Guided Mode Resonance Enhanced Microscopy and Lasing

Manuel Deckart

Doctor of Philosophy

Physics

University of York

March 2023

Abstract

A major goal of nanophotonics research is to enhance light-matter interaction and to develop novel functionalities. The work in this thesis addresses this goal in 2 areas, i.e. microscopy and laser emission, using guided mode resonances (GMRs) as a tool.

GMRs exhibit significant field enhancements, which makes them interesting for the enhancement of light-matter interactions, such as light scattering or fluorescence emission; the challenge was to show whether and how GMRs could be used to improve microscopy methods such as interferometric scattering microscopy (iSCAT) and fluorescence microscopy. The second challenge was to show whether GMRs could be used to enhance laser operation of 2D-material lasers.

In the first part of the thesis, I describe how I built, tested and optimised an optical system that allows the study of enhanced microscopy. Then I demonstrate an efficient method for quantifying the enhancement of fluorescence excitation with a chirped GMR grating. With regular iSCAT, I was able to detect gold nanoparticles as small as 20 nm.

In the second part, I show how a two-dimensional GMR grating can be used to both enhance the pump absorption and the laser emission of a WS_2 monolayer. The devices, lasing with a low pump threshold, have a much higher output power and spatial coherence than other 2D-material lasers reported in the literature.

The contrast enhancement in microscopy opens new possibilities, as it can either push the detection limits or simplify the setup requirements for detecting a given particle. Regarding the lasing application, I showed that the concept of GMR-based lasers with large area 2D-material gain media is promising. The concept could be adapted to other 2D-materials emitting at wavelengths relevant for communication or sensing applications. This would represent an important step towards operation with reduced power consumption or for opening novel opportunities for making lasers.

Acknowledgements

I am grateful to my supervisor Prof Thomas F Krauss, for welcoming me in his research group and giving me the support when needed, but also the freedom to explore, learn and grow as an independent researcher.

I also want to thank Dr Yue Wang for a truly inspiring collaboration on 2D material lasers, which represents an important part of this thesis.

I am extremely grateful for the friendship, encouragement and support from the past and present members of the Photonics Group and the Bio-Inspired Technologies group: in particular, Dr Chris Reardon, who provided me with invaluable help and advice when it came to problem-solving; Dr George Duffett, for inspiring discussions, and who together with Dr Augusto Martins and Kalum Thurgood-Parkes was also a great support outside of work; Dr Donato Conteduca, whose cheerful personality and guidance were most appreciated; Dr Isabel Barth and Dr Giampaolo Pitruzzello, for fruitful photonics discussions. Thank you to my colleagues Rhys Ashton, Shrishty Bakshi, Sam Blair, Dr Ben Coulson, Francisca D'Rozario, Dr Pin Dong, Dr Alexander Drayton, Dr Richard John, Dr José Juan-Colás, Minahil Khan, Dr Soheila Kharratian, Dr Casper Kunstmann, Dr Kezheng Li, Josh Male, Dr Lisa Miller, Dr Lewis Reeves, Dr Pankaj Sahoo, Dr Callum Silver, Dr Matthew Simmons, Adam Stroughair, Dr Nyasha Suliali, and Katie Thornton.

I thank Prof Steven Johnson for the support with the chemistry. Many thanks to Dr Laurence Wilson, who was an enthusiastic and supportive TAP member. I also thank Dr Steve Quinn for the support in planning the fluorescence imaging part of the optical setup. Thank you to Tim Ayers, for providing the electronic solutions, and the mechanical workshop for making essential parts for the optical setup. A particular thank you goes to Prof Phillip Kukura, Dr Stephen Thorpe and Jack Peters from Kukura lab in Oxford, who gave valuable advice concerning my iSCAT setup.

A warm thank you to the Capoeira In York Community - the trainings helped me find balance, take a step back and clear my mind. I deeply thank my parents, Richard and Daniela, and my friend Livia, who never stopped believing in me and kept encouraging me to give my best. Finally, I want to thank my partner, Emily, whose unconditional love and support have truly enabled me to make it this far and to overcome the lows that I faced. Merci!

Declaration of Authorship

I declare that this thesis is a presentation of original work and I am the sole author. This work has not previously been presented for a degree or other qualification at this University or elsewhere. All sources are acknowledged as references.

Attended Events

- BPSI Symposium 2019: Light and Life - A molecular perspective, York (presentation)

- AMOLF International Nanophotonics School 2019, Amsterdam (poster)

- Physics of Life Summer School 2019, Durham (poster)

- Royce@Leeds Winter School 2020, Leeds

- Workshop on Interferometric Scattering Microscopy 2020, Erlangen, virtual

- Photonics Spectra Conference 2023, virtual

Contents

Abbreviations

ACE	Acetone
AuNP	Gold nanoparticles
BFP	Back focal plane
BIC	Bound state in the continuum
DI	De-ionised (water)
DOS	Density of states
EBL	E-beam lithography
FBZ	First Brillouin zone
FF	Fill factor
FFP	Front focal plane
FoV	Field of view
GMR	Guided mode resonance
IPA	Isopropanol
iSCAT	Interferometric scattering microscopy
NA	Numerical aperture
PDMS	Polydimethylsiloxane
PMMA	Poly(methyl methacrylate)
PR	Partial reflector
PSD	Power spectral density
PSF	Point spread function
RCWA	Rigorous coupled wave analysis
RIE	Reactive ion etching
ROI	Region of interest
SEM	Scanning electron microscopy
Si_3N_4	Silicon nitride
SNR	Signal-to-noise ratio
TE	Transverse electric
TIR	Total internal reflection
TM	Transverse magnetic
TMD	Transition-metal dichalcogenide
WS_2	Tungsten disulfide

Chapter 1

Brief Introduction

1.1   Guided Mode Resonance

Guided mode resonances (GMRs) occur in diffraction gratings that are made of high index material and are therefore able to support leaky guided modes in the grating layer. The grating parameters are designed to produce a resonance at the wavelength that corresponds to the period of the grating. GMRs are characterised by their peak in the reflection/transmission spectrum and by significant electric field enhancements of the resonant modes (typical $E/E_0 = 10 - 20$ on resonance).

GMRs find applications in a wide range of fields, such as sensors, photodetectors, polarisers, spectrometers, optical filters and more [1]. In this work, I focus on the use of GMRs in the fields of microscopy and lasing.

1.2   Microscopy

Optical microscopy is an essential tool for studying systems from the micro- to the nanoscale. Especially in biophysics and in the life sciences, observations of single particles can reveal information that is inaccessible with ensemble average approaches [2]. As the particle size decreases, most optical contrast mechanisms reach their limit in terms of resolution or signal-to-noise ratio.

The various optical microscopy approaches can be grouped into two main categories, according to the mechanism that provides the contrast: fluorescence and light scattering. Fluorescence microscopy relies on the ability of imaged particles to absorb light at a

given wavelength during excitation, followed by a relaxation via emission of light at usually longer wavelengths. The excitation light is then attenuated using optical filters in order to suppress the background and achieve high contrast images. Imaging of particles in complex media can be achieved with site-specific labels and super-resolution imaging beyond the diffraction limit can also be achieved [3]. For applications requiring a high spatial and temporal resolution, e.g. in single particle tracking, fluorescence microscopy is fundamentally limited by the photon emission rate of the fluorophore. In cases where the used fluorophores suffer from photo-blinking or photo-bleaching [4], the total observation time is limited as well.

Given these limitations, it worth asking whether there is a place for microscopy techniques that rely on light scattering rather than on fluorescence, and whether such techniques could resolve nanoscale particles. A particularly interesting method is that of interferometric scattering microscopy (iSCAT), as its interferometric detection scheme provides extremely high sensitivity that allows single particle tracking with high spatio-temporal resolution and label-free detection down to the single protein level.

The interesting properties of GMRs can be used to further push the limits of both scattering [5] and fluorescence based microscopy [6]. The high quality resonances exhibited by GMRs in dielectric gratings offer strong field enhancement, which benefits both methods. In addition, the raditating mode of a GMR is well defined such that it is possible to channel the light scattered or emitted from a particle into specific far field radiation angles, which improves the collection efficiency.

In order to obtain a grating at the desired resonance wavelength, I usually perform initial design simulations to find the relevant parameters. As the simulations describe an ideal system, whereas a realistic system suffers from fabrication imperfections and inconsistencies, a number of gratings have to be fabricated with parameters covering a range that is centred around the simulated values. The gratings resulting from this lithographic tuning are then characterised in order to identify the desired resonance and actual structural parameters.

1.3   Lasing

Since their first realisation in 1960 [7], lasers have seen tremendous developments and are now widely used in science, technology and medicine.

The two main requirements for laser operation are a gain medium and an optical

cavity. The gain medium is optically or electrically pumped to put the gain medium into an excited state. The medium then spontaneously relaxes into a lower energy state, with the energy difference being released as a photon of the corresponding wavelength. When a photon of this wavelength then propagates through the excited emitter, it can stimulate the release of more photons into the same state (wavelength, phase, direction and polarisation). The function of the optical cavity is to provide the resonant feedback, so that the photons in the lasing state keep propagating through the gain medium and keep stimulating more photons into the same lasing mode.

For applications where high output powers are typically not required, such as data communications, optical computing and optical sensing, it is of interest to reduce the footprint and power consumption by making efficient use of the gain material and to achieve lasing at low pumping power, which drives the search for suitable gain materials and laser designs. 2D materials (graphene-like materials of atomic layer thickness) are promising gain media, especially monolayer transition-metal dichalcogenide (TMD) semiconductors, which are efficient light emitters due to their direct band gap and strong exciton binding energy.[8]

While the TMD monolayers are characterised by a high quantum efficiency, the total gain - and therefore the output power – is rather limited because of the very small overlap of the resonant mode with the gain material. With such relatively low modal gain, the appropriate design of a high quality cavity is all the more important for achieving lasing with sufficient output power.

One aim of this work is therefore to introduce a suitable cavity design based on GMRs, then demonstrate and characterise the lasing properties of the resulting devices.

1.4 Thesis Outline

In chapter 2 of this thesis, I present Maxwell's equations, how they can be used to describe light and its interaction with dielectric materials. Moreover, I describe the concepts of guided modes and diffraction, then bring them together in order to describe a GMR, along with its range of important properties.

In chapter 3, I show how GMR gratings are fabricated using e-beam lithography and reactive ion etching. Then, I verify the grating geometry by means of scanning electron microscopy and characterise the resonances by means of the peaks in the reflection spectrum.

As a key aim is to study GMR-enhanced microscopy, an appropriate optical setup is required. To this end, I describe the building, testing and optimisation of a combined iSCAT and fluorescence microscopy setup in chapter 4.

In chapter 5, I demonstrate the use of a chirped GMR design for the efficient characterisation of the resonance and quantification of contrast enhancement in microscopy. As an example, I consider the excitation enhancement of fluorescent beads.

In chapter 6, I introduce a GMR grating design that not only supports a GMR resonance for enhancing the excitation of a photo-luminescent flake of 2D material, but also supports a second resonance that acts as a lasing cavity with a high Q-factor. I will first describe the design in more detail, then characterise the cold-cavity modes of the grating without active material. Finally, I describe several properties of the lasing device, such as the threshold behaviour, linewidth narrowing, directionality and polarisation.

Chapter 2

Guided Mode Resonance Theory

At the beginning of this chapter, I show how Maxwell's equations (section 2.1) can be used to describe light as an electromagnetic wave (section 2.2). In a second step, refraction of a beam of light (section 2.3) is considered, and how it relates to total internal reflection (section 2.4), a phenomenon allowing confinement of light inside dielectric slab waveguide structures (section 2.5). The thin film response observed from slab waveguides when illuminated with an out-of plane beam is described in section 2.6.

Section 2.7 describes diffraction, which is the mechanism that enables coupling between waves of different propagation directions.

At the end of the chapter, I bring the concepts of diffraction and guided modes together in order to describe a guided mode resonance (GMR) in section 2.8. This explanation is supported by the concept of Bloch modes, which are used to describe the resonant modes in a periodic dielectric medium (section 2.8.3). This then leads to the concept of a photonic band structure (section 2.8.5) and the photonic band gap (section 2.8.4). An example band structure and the corresponding field distribution of the resonant modes are simulated in section 2.8.6.

Section 2.9 shows how the resonances can be described by a Fano line shape. Finally, Purcell enhancement (section 2.11) and limitations due to non-radiative losses (section 2.12) are discussed.

2.1 Maxwell's Equations

Maxwell's equations describe electric and magnetic fields. A range of assumptions on the material properties are made in order to obtain the equations in the relevant form.

- there is no source of charges or currents.

- the field intensity is low enough to neglect non-linear effects, i.e. the displacement field $\mathbf{D} = \epsilon \mathbf{E}$ varies linearly with an applied electric field $\mathbf{E}$ in a medium of permittivity $\epsilon = \epsilon_0 \epsilon_r$, where ϵ_0 is the vacuum permittivity and ϵ_r is the material dependent relative permittivity.

- ϵ is homogeneous and isotropic for a given material, i.e. it is a scalar and behaves the same in all directions of polarisation.

- the materials are non-magnetic, they are described by the magnetic susceptibility $\mu = \mu_0$ in vacuum.

These assumptions hold for the materials with which the resonant gratings are fabricated in this work. The corresponding Maxwell's equations are [9]:

Gauss' law

$$\boldsymbol{\nabla} \cdot (\epsilon \mathbf{E}) = 0 \tag{2.1}$$

Maxwell-Faraday equation:

$$\boldsymbol{\nabla} \times \mathbf{E} = -\frac{\partial \mathbf{B}}{\partial t} \tag{2.2}$$

Gauss' law for magnetism:

$$\boldsymbol{\nabla} \cdot \mathbf{B} = 0 \tag{2.3}$$

Ampère's law:

$$\boldsymbol{\nabla} \times \mathbf{B} = \epsilon \mu_0 \frac{\partial \mathbf{E}}{\partial t} \tag{2.4}$$

The four equations lay the foundation of electromagnetic theory. In the following, I show they can be used to describe light, covering phenomena that range from simple propagation in free space to guided mode resonance.

2.2 Wave Equation

As the materials in this work are assumed to be non-magnetic ($\mu/\mu_0 = 1$), the fields are manipulated via the permittivity ϵ. Since ϵ describes how a material responds to an electric field, I will focus on the solutions of $\mathbf{E}$ in the following sections.

The Maxwell-Faraday equation (Eq 2.2) couples the electric to the magnetic field. To find a solution, the fields can be decoupled by firstly applying the curl operator on both sides of the equation. Using the vector identity

$$\boldsymbol{\nabla} \times (\boldsymbol{\nabla} \times \mathbf{E}) = \boldsymbol{\nabla}(\boldsymbol{\nabla} \cdot \mathbf{E}) - \boldsymbol{\nabla}^2 \mathbf{E} \tag{2.5}$$

together with Gauss' law (Eq 2.1) and Ampère's law (Eq 2.4), one finds the decoupled wave equation for the electric field

$$\left(\boldsymbol{\nabla}^2 - \epsilon \mu_0 \frac{\partial^2}{\partial t^2} \right) \mathbf{E} = 0 \ . \tag{2.6}$$

A solution to this wave equation is given by the plane wave

$$\mathbf{E}(\mathbf{r}, t) = \mathbf{E_0} e^{i(\mathbf{k_n} \cdot \mathbf{r} - \omega t)}, \tag{2.7}$$

whose propagation direction is along the wave vector $\mathbf{k_n}$, and ω is the angular frequency.

In three-dimensional space, a wavefront is defined as the surface corresponding to a constant arbitrary phase $\phi = (\mathbf{k_n} \cdot \mathbf{r} - \omega t) = \phi_0$. The wavefronts propagate at a phase velocity

$$v = \frac{\omega}{k_n} = \frac{1}{\sqrt{\epsilon \mu_0}} = \frac{c}{n} \ , \tag{2.8}$$

which corresponds to the speed of light in vacuum $c = \frac{1}{\sqrt{\mu_0 \epsilon_0}}$, divided by the refractive index $n = \sqrt{\epsilon_r}$.

In vacuum, the refractive index is $n = 1$, and the vacuum wavelength is defined as

$$\lambda_0 = \frac{2\pi}{k_0}, \tag{2.9}$$

with the vacuum wave number $k_0 = |\mathbf{k_0}|$.

In a medium of $n \neq 1$, the wavenumber is given by $k_n = nk_0$, which yields a wavelength

$$\lambda_n = \frac{\lambda_0}{n} \ . \tag{2.10}$$

The polarisation of the wave describes in which direction the fields oscillate. One can plug the plane wave equation (Eq 2.7) into Gauss' law (Eq 2.1) in order to find that the electric field component along the propagation direction is zero. The same can be shown for the magnetic field. Therefore, light propagating as a plane wave in free space is a transverse electromagnetic wave.

2.3   Snell's Law

Consider a beam of light propagating along $\mathbf{k_1}$, impinging on a planar interface between two different dielectric materials at an angle θ_1 with respect to the normal, as shown in Fig 2.1 A). A portion of the beam is reflected and propagates along $\mathbf{k_1'}$ at the same angle θ_1 on the opposite side of the normal.

In general, another portion of the beam can be transmitted, but will propagate at a different angle θ_2, which relates to θ_1 via Snell's law [9]

$$n_1 \sin(\theta_1) = n_2 \sin(\theta_2) \ , \tag{2.11}$$

where n_1 and n_2 are the refractive indices of the media of incidence and transmission, respectively.

2.4   Total Internal Reflection

2.4.1   Critical Angle

The upper limit of the transmission angle θ_2 in Eq 2.11 is given by $90\,^{\circ}$, i.e. propagation parallel to the interface. The corresponding incidence angle θ_1 is known as the critical angle

$$\theta_c = \sin^{-1}\left(\frac{n_2}{n_1}\right) \ . \tag{2.12}$$

For any incidence angles $\theta_1 > \theta_c$, Eq 2.11 has no real solution for θ_2, i.e. no propagating wave exists on the low-index side. Instead, the field is described by an evanescent wave,
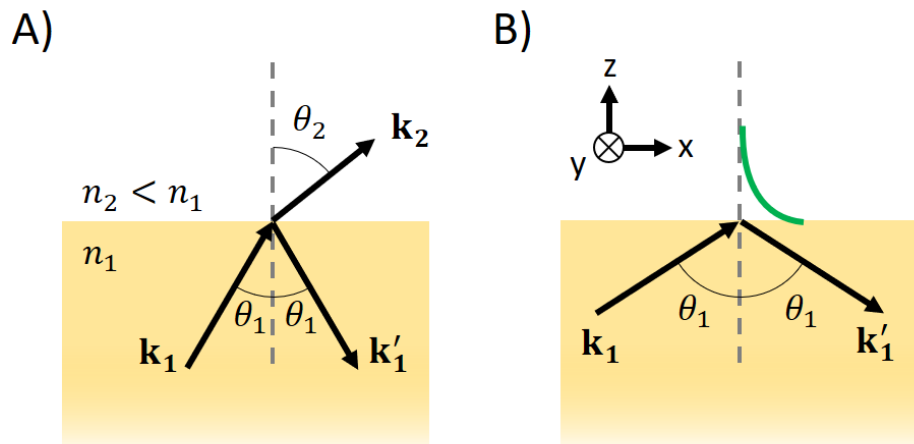
Figure 2.1: Reflection and transmission of light at a refractive index interface with incidence from the higher index medium. The critical angle for total internal reflection is θ_c (Eq 2.12). A) Incidence at $\theta_1 < \theta_c$, with propagating transmitted and reflected light. B) Incidence at $\theta_1 > \theta_c$, where propagation is only possible for the reflected light. On the lower index side (n_2), the amplitude of the evanescent field decays exponentially (green line).

as illustrated in Fig 2.1 B). In this regime, all the light is completely reflected back into the high index medium eventually, corresponding to total internal reflection (TIR).

2.4.2 Evanescent Wave

The transmitted wave is described by $\mathbf{k_2}$, whose z-component is

$$k_{2,z} = n_2 k_0 \cos(\theta_2) \ . \tag{2.13}$$

The cos-term can be written as

$$\cos(\theta_2) = \pm\sqrt{1 - \sin^2(\theta_2)} = \pm\sqrt{1 - \left(\frac{n_1}{n_2}\sin(\theta_1)\right)^2} \ , \tag{2.14}$$

where Snell's law (Eq 2.11) was applied. When $\theta_1 > \theta_c$ the term inside the square root is negative, which leads to a purely complex z-component of $\mathbf{k_2}$.

When plugging Eq 2.13 and 2.14 into the plane wave equation (Eq 2.7), it is found that the wave in the low index medium is described by an exponentially decaying amplitude along the z-axis,

$$E_2(z) \propto e^{-\kappa z} \ , \tag{2.15}$$

with

$$\kappa = k_0 \sqrt{n_1^2 \sin^2(\theta_1) - n_2^2} \; . \tag{2.16}$$

Note that the solution of Eq 2.14 of the opposite sign corresponds to an exponentially increasing solution and is discarded, as it is not physical.

The evanescent wave can be characterised by its penetration depth $l = \frac{1}{\kappa}$ corresponding to the distance at which the amplitude drops by a factor of $1/e$. The depth l decreases when θ_1 or n_1 are increased, or when n_2 is decreased.

For the example of an interface between glass ($n_1 = 1.5$) and water ($n_2 = 1.333$), with light of wavelength $\lambda = 600$ nm at high incidence angles $\theta \gtrsim 80\,^\circ$, the penetration depth is $l \approx 140$ nm. In contrast, typical guided mode resonances described in this work have an effective index of $n_{eff} = 1.55$, which yields a penetration depth of $l = 120$ nm into the water medium (see more details in the following sections and Eq 2.18).

2.5 Guided Modes

2.5.1 Slab Waveguide

A slab waveguide [9, 10] is a structure that is able to confine light in one arbitrary dimension z, allowing propagation along the orthogonal directions x and y, see Fig 2.2.

With dielectric materials, the light confinement can be achieved with TIR. In order for TIR to occur in the positive and negative z-direction, the refractive index of the slab n_1 must be greater than the indices n_0 and n_2 of the medium below and above the slab, respectively.

Along the xy-plane, the slab extends infinitely and indices are assumed homogeneous. Consider propagation along the arbitrary x-axis, which makes the solution independent of y. This leads to a solution with an envelope in z, propagating in plane as

$$\mathbf{E}(x, z) = \mathbf{E}(z) e^{i(k_x x - \omega t)} \; , \tag{2.17}$$

where the in-plane wave vector component is $k_x = n_{eff} k_0$, with effective index n_{eff}. The envelope along the z-axis is described by

$$\left(\frac{\partial^2}{\partial z^2} + k_z^2 \right) \mathbf{E}(z) = 0 \; , \tag{2.18}$$
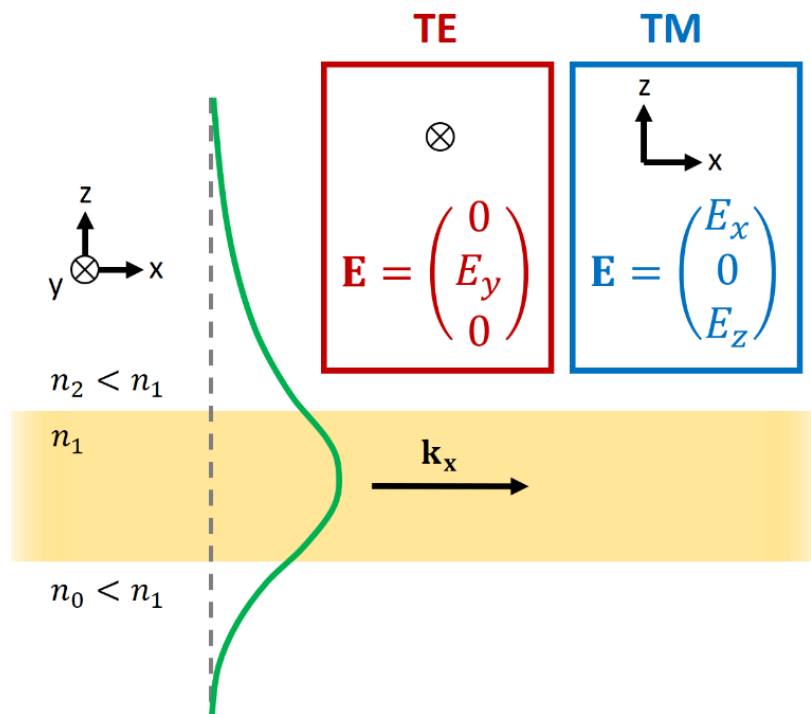
Figure 2.2: Schematic of a slab waveguide with intensity profile of the fundamental guided mode (green) propagating along the x-axis. The oscillation direction of the electric field for the TE and TM polarisation is shown in the red and blue frame, respectively.

with

$$k_z^2 = k_n^2 - k_x^2 \ . \tag{2.19}$$

Note that $k_n = nk_0$ depends on the medium index n, which leads to three different solutions for the envelope in the three layers.

For guided modes, the envelope is described by evanescent tails in the surrounding media, and a sinusoidal wave inside the slab. At the interfaces, the wave must satisfy boundary conditions that depend on the polarisation of the mode (see following section).

For a given wavelength λ_0, one or more solutions of Eq 2.18 are possible, corresponding to different effective indices. The effective index n_{eff} of the guided mode is given by a weighted sum of the material indices, where the weights are determined by the envelope. The order of the guided mode is given by the number of nodes of the sinusoidal wave inside the slab, where a higher order corresponds to a lower n_{eff}.

2.5.2 Boundary Conditions

For transverse electric (TE) modes, the electric field is orthogonal to the propagation direction and the index interfaces. If the confinement is along z and propagation along x, the only non-zero electric field component is E_y (Fig 2.2).

The other polarisation of interest is transverse magnetic (TM), where it is the magnetic field whose oscillation is orthogonal to the propagation direction and the interfaces. In this case, the non-zero electric field components are E_x and E_z. Note that there is an electric field component along the propagation direction of the mode, which would not be possible for plane waves in free space.

Gauss' law (Eq 2.1) implies that the displacement field component $D_z = \epsilon E_z$ normal to the interface is continuous. With Faraday's law (Eq 2.2), it can be shown that the tangential components of the electric field E_x and E_y are continuous.

As the TE and TM modes satisfy different boundary conditions, they have different envelopes along z. Therefore, they have different effective indices n_{eff} and different field distributions for a given λ_0.

2.6 Thin Film Interference

As described in the previous section, a thin film of high index material surrounded by lower index media can support guided modes. The light in such modes is confined to the slab, i.e. it cannot couple to out-of-plane propagating waves. This implies that the inverse is not possible either: A beam of light propagating in free space that impinges on the slab out-of-plane cannot couple to the guided modes either.

Instead, the beam will be partially reflected and transmitted at the first index interface with amplitude coefficients r_{01} and t_{01}, respectively, see Fig 2.3. Note that the reflected beam (red arrow) experiences a phase change of π, as $n_1 > n_0$. The transmitted part propagates on to the second index interface, where it is partially reflected, travels back up to the first interface and is partially transmitted (green, solid arrow). The reflected part keeps travelling between the interfaces, with its amplitude decreasing with each round trip, as it is partially transmitted (green, dashed arrow) at each interface.

It can be shown, using geometry arguments and Snell's law, that the phase difference
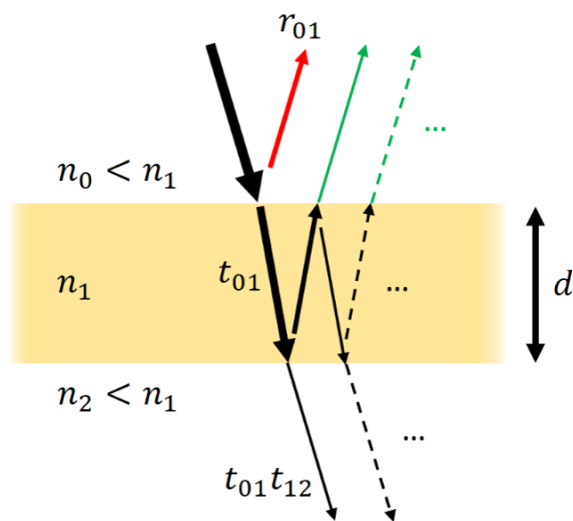
Figure 2.3: Thin film interference. An incoming beam of light is partially reflected and transmitted at each refractive index interface. The reflected part of the light inside the film bounces between the interfaces with an amplitude that decreases at each reflection, which is illustrated by the thinning and eventual disappearance of the arrows.

accumulated during one round trip inside the slab is given by

$$\Delta\phi = 2n_1 k_0 d \cos(\theta_1) \ , \tag{2.20}$$

where $k_0 = \frac{2\pi}{\lambda_0}$, d is the film thickness, and θ_1 is the angle of the refracted beam inside the slab.

The resulting reflection spectrum represents the sum of all the individual portions of light from each round trip. Consider a fixed angle of incidence. If the wavelength is such that $\Delta\phi$ is a multiple of 2π, then all portions transmitted from within the thin film back into the medium of incidence constructively interfere with each other. The initial reflection of the incident beam (red arrow) has a π-shift with respect the sum of waves from inside the slab (green arrows), i.e. they destructively interfere. This corresponds to a dip in the reflection spectrum, or a peak in the transmission spectrum.

In contrast, if the phase difference is $\Delta\phi = \pi + m2\pi$ with $m \in \mathbb{Z}$, the waves from consecutive round trips interfere destructively with each other, but the initial reflection is in phase with the portion of light coming back from the first round trip. This scenario corresponds to a peak in reflection.

Since the reflection coefficients of refractive index interfaces are generally low, peaks

and dips in the spectrum are wide and slowly varying with λ_0. Note that the shape of the spectrum is slightly different for light whose electric field is oriented orthogonally to the plane of the incident and reflected beam (s-polarised) and light polarised parallel to the plane (p-polarised). This is due to the polarisation dependence of the reflection and transmission coefficients of the interfaces.
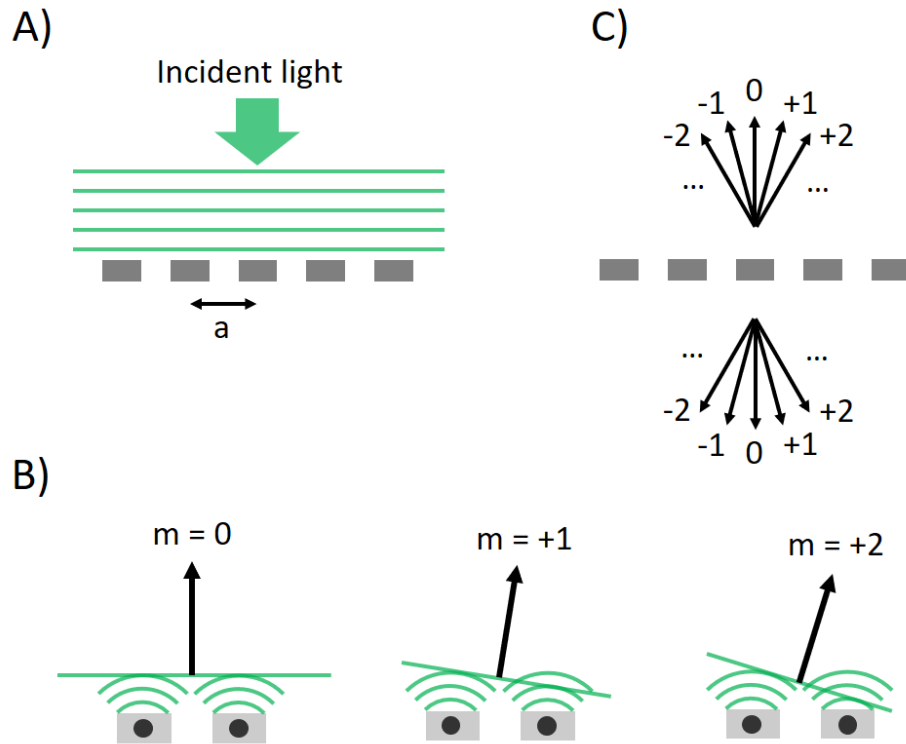
2.7 Diffraction Grating

Diffraction [9, 10] is one of the key phenomena that give rise to guided mode resonance, as it provides the coupling between guided modes and out-of-plane propagating waves (see section 2.8).

Recall from section 2.3 that a plane wave incident on a planar refractive index interface is partially reflected and propagates as a plane wave at a single, well defined angle. However, if the wave interacts with an object of a finite size comparable to the wavelength λ_0, it may be scattered into a continuous range of angles. In order to generate such scattering in a controlled manner, an optical diffraction grating may be created by periodically arranging multiple unit cells, each containing the same scattering object, with a period a of the order of λ_0. Fig 2.4 A) shows a grating with a plane wave at normal incidence.

Consider two neighbouring unit cells separated by the period a, as shown in Fig 2.4 B). The unit cell of the grating is approximated as a point source scattering a spherical wave into the surrounding medium of refractive index n. When two wave fronts meet in phase, they constructively interfere. If the path difference between the two waves is zero, their interference is always constructive. This case corresponds to diffraction order $m = 0$, with a diffraction angle that is equal to the angle of incidence flipped around the normal of the grating.

Constructive interference may also occur when a number m of wave fronts is "skipped" between the two waves, e.g. $m = 1$ or $m = 2$ illustrated in Fig 2.4 B), which results in waves propagating at an angle. A finite number of diffraction orders may exist on both sides of the grating, see Fig 2.4 C). Note that half-way between two consecutive diffraction orders, the interference is destructive, i.e. no light can propagate along the corresponding direction.

The diffraction angles are calculated for an incoming wave at normal incidence, using the schematic in Fig 2.5. For an observation point at angle θ and distance $d \gg a$

Figure 2.4: Schematic of an optical diffraction grating. A) Plane wave at normal incidence on the grating of period a. Wavefronts are represented by green lines. B) Two neighbouring unit cells of the grating represented as point sources (black dots). The diffraction order m and corresponding propagation directions (black arrows) at angles for which the two waves interfere constructively. Green line: Diffracted wave front. C) Positive and negative diffraction orders in reflection and transmission.
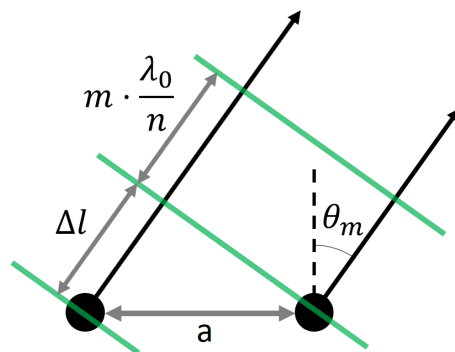
Figure 2.5: Schematic for the calculation of diffraction angles, with grating period a. For constructive interference at different angles θ_m, the path difference Δl is equal to m times the wavelength in medium $\lambda_n = \lambda_0/n$.

far away from the grating, the path difference between the two waves is given by

$$\Delta l = a \sin(\theta) \ , \tag{2.21}$$

corresponding to a phase difference of

$$\Delta \phi(\theta) = k_n \Delta l = \frac{n2\pi}{\lambda_0} a \sin(\theta) \ . \tag{2.22}$$

Constructive interference occurs when $\Delta\phi = m2\pi$, with the integer m corresponding to the order of diffraction, which yields the diffraction angle

$$\theta_m = \sin^{-1}(m \cdot \frac{\lambda_0}{an}) \ . \tag{2.23}$$

As the domain of the $\sin^{-1}$ function is [-1,1], the equation only allows real solutions when

$$|m| \leq \frac{an}{\lambda_0} \ . \tag{2.24}$$

This means that for a given wavelength λ_0, a sufficient increase of the period a leads to an increase in the number of diffraction orders and reduces their angular spacing. On the other hand, if a is reduced so that

$$a < \frac{\lambda_0}{n} \ , \tag{2.25}$$

the number of diffraction orders is only one, with order $m = 0$. It is important to notice that for a higher index medium, a larger number of diffraction orders might be available.
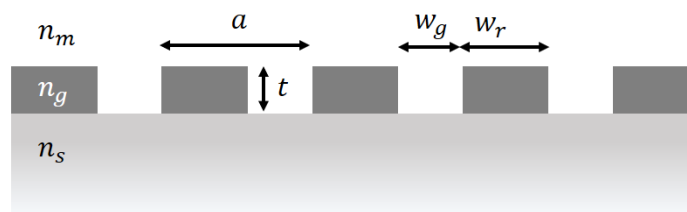
2.8   Guided Mode Resonance

2.8.1   Grating Geometry

The geometry of a GMR-grating is parametrised according to Fig 2.6. The fill factor is defined as

$$FF = \frac{w_r}{a} \ , \tag{2.26}$$

with the width w_r of the grating ridge and period a.

Figure 2.6: GMR-grating geometry, with grating thickness t, ridge width w_r, gap width w_g, period a, and refractive indices of the substrate (n_s), grating (n_g) and medium (n_m).

2.8.2   Summary of Basic Principles

Consider a GMR-grating as shown in the previous section 2.8.1. The key point to note is that the index n_g of the grating material has to be significantly higher than its surrounding media, so that the resulting effective index n_{eff} satisfies

$$n_{eff} > n_s \qquad \text{and} \qquad n_{eff} > n_m \,, \tag{2.27}$$

for the grating layer to be able to support guided modes.

For a given wavelength λ_0, the period a is designed small enough, so that in the medium and substrate, only the 0th order of diffraction is supported (see Eq 2.25). However, a is chosen big enough for the first diffraction orders $m = \pm 1$ to exist in the grating layer [11], i.e.

$$\frac{\lambda_0}{n_{eff}} \le a < \frac{\lambda_0}{n_i}, \qquad i \in \{\text{substrate}, \text{medium}\} \,. \tag{2.28}$$

When a beam of light with wavelength λ_0 impinges at normal incidence on the grating (Fig 2.7 A), the zero order light only experiences the thin film response of the grating. The first order light is diffracted into the grating layer and couples to a leaky guided mode.

As the mode propagates along the grating (Fig 2.7 B), a small amount of light is scattered at each interface between the grating ridge and the gap. As a result, the leaky guided mode experiences two kinds of diffraction. On one hand, in-plane diffraction causes the light to bounce back and forth (black arrows) along the direction of periodicity. On the other hand, out-of-plane diffraction (Fig 2.7 C) allows the light

to couple back out to free space radiation - the inverse process of A).

If λ_0 and a are such that all the scattered waves are in phase, the resonance condition is met. This phase-matching condition relates the effective index n_{eff} of the leaky guided mode to the resonant wavelength λ_{res} and the grating period a as

$$n_{eff} = \frac{\lambda_{res}}{a} \ .$$

(2.29)

In this case, the total out-coupled wave interferes with the light that experienced the thin film response at the start. Depending on whether the interference is constructive or destructive, the incident wave may be completely reflected or transmitted.
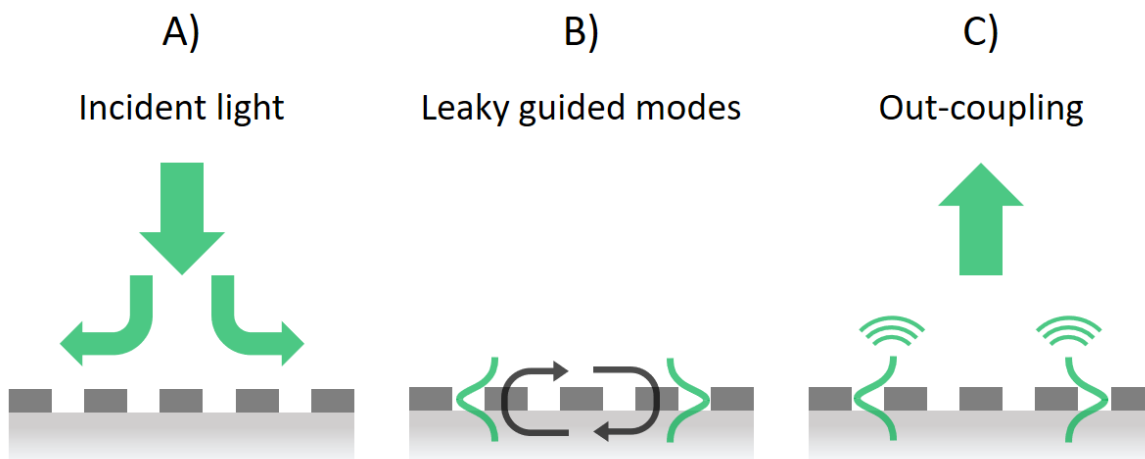
Figure 2.7: Basic principles involved in a GMR. A) A beam of light at normal incidence, diffracting into the grating layer. B) Guided modes (green profiles) experiencing in-plane diffraction (black arrows). C) The guided modes are leaky and couple to out-of-plane free space radiation.

2.8.3 Bloch Modes

Consider a periodic permittivity

$$\epsilon(x) = \epsilon(x + a) \ ,$$

(2.30)

with period a, choosing the x-axis as the arbitrary grating direction.

According to Bloch's theorem [12], the solution to the wave equation (Eq 2.6) in

such a medium is given by

$$E_{k_x}(x) = e^{ik_x x} u_{k_x}(x) \ , \tag{2.31}$$

which corresponds to a plane wave $e^{ik_x x}$ modulated by a function $u_{k_x}(x)$ that has the same periodicity as $\epsilon(x)$.

Therefore, the wave can be expressed as

$$E_{k_x}(x) = \sum_{m=-\infty}^{\infty} E_m e^{i(k_x + mG_x)x}, \ m \in \mathbb{Z} \tag{2.32}$$

with the reciprocal lattice vector $\mathbf{G}$, whose only non-zero component in this example is

$$G_x = \frac{2\pi}{a} \ . \tag{2.33}$$

The Bloch modes can therefore be viewed as a linear combination of a discrete set of plane waves with different in-plane wave vector components. For example, in the case of the GMR mode, light at normal incidence with $k_x = 0$ can couple to guided waves $k_x = \pm G_x$, since they are part of the same Bloch mode.

2.8.4 Photonic Band Gap

The photonic band gap [10] is well illustrated by the modes on either side of the first band gap at $k_x = \frac{G_x}{2}$. According to Eq 2.32, this mode has plane wave components

$$E_0 e^{i\frac{G_x}{2}x}$$

and

$$E_{-1} e^{-i\frac{G_x}{2}x} \ .$$

As illustrated in Fig 2.8, the two waves have an in-plane wave vector of equal amplitude and opposite sign, i.e. they are two counter-propagating waves that form a standing wave. The nodes of the standing wave can either be located in the grating ridge or in the gap, in order to respect the symmetry of the system.

If the nodes are located in the gap, a large amount of the standing wave will overlap with the ridge, resulting in a higher effective index. If on the other hand the nodes are in the ridge, the wave will mainly overlap with the gap, resulting in a lower refractive index.
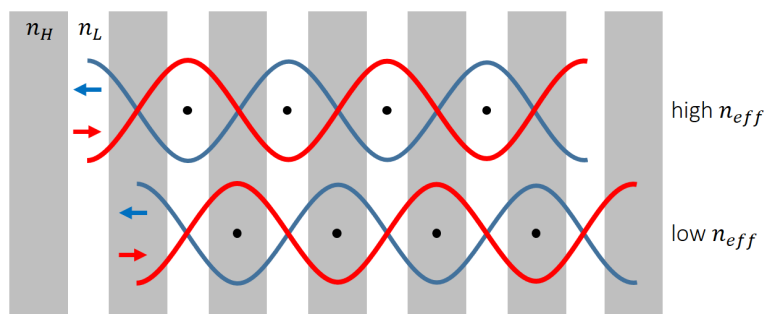
Figure 2.8: Illustration of counter-propagating waves in a GMR-grating, consisting of alternating sections of high (n_H) and low (n_L) refractive index. Counter-propagating waves in red and blue form a standing wave with nodes (black dots), where the waves cancel each other out. Between the nodes, the standing wave amplitude oscillates. The effective index depends on the position of the nodes and peaks of the standing wave.

Between the lower and higher effective indices, no solution is available, i.e. no Bloch mode exists in the grating layer. This corresponds to the photonic band gap. A beam of light hitting the grating at a forbidden wavelength lying within a gap, will simply experience the thin film response of the grating layer.

2.8.5   Photonic Band Structure

In the equation for the Bloch mode (Eq 2.32), it can be seen that $E_{k_x+lG}(x) = E_{k_x}(x)$, for any $l \in \mathbb{Z}$. This shows that all the information provided by the equation can be folded back into a finite range of k_x, e.g. $-\frac{G_x}{2} \leq k_x \leq \frac{G_x}{2}$, which is the first Brillouin zone (FBZ). Due to the folding, a band structure is obtained, where different bands have different effective indices and corresponding resonant wavelengths for a given period.

The band diagram can be inferred from the resonant peaks in the optical reflection spectra at different incident angles. I simulate these spectra with the S^4 software [13], which is an implementation of the semi-analytical rigorous coupled wave analysis (RCWA) [14]. A number of spatial harmonics $n_{Harm} = 21$ is used in this work, see the appendix for the convergence plots supporting this choice (Appendix A.1).

Consider, as an example, a silicon nitride grating on a glass substrate covered by a water medium. The refractive indices are assumed constant over the considered wavelength range, represented by the indices at $\lambda = 655$ nm of $n_g = 2.0368$, $n_s = 1.4693$ and $n_m = 1.333$ for the grating, substrate and medium, respectively [15]. The corresponding band diagram (Fig 2.9) features distinct lines, which correspond to the photonic bands of the periodic structure. The values of k_x go beyond the FBZ, in order
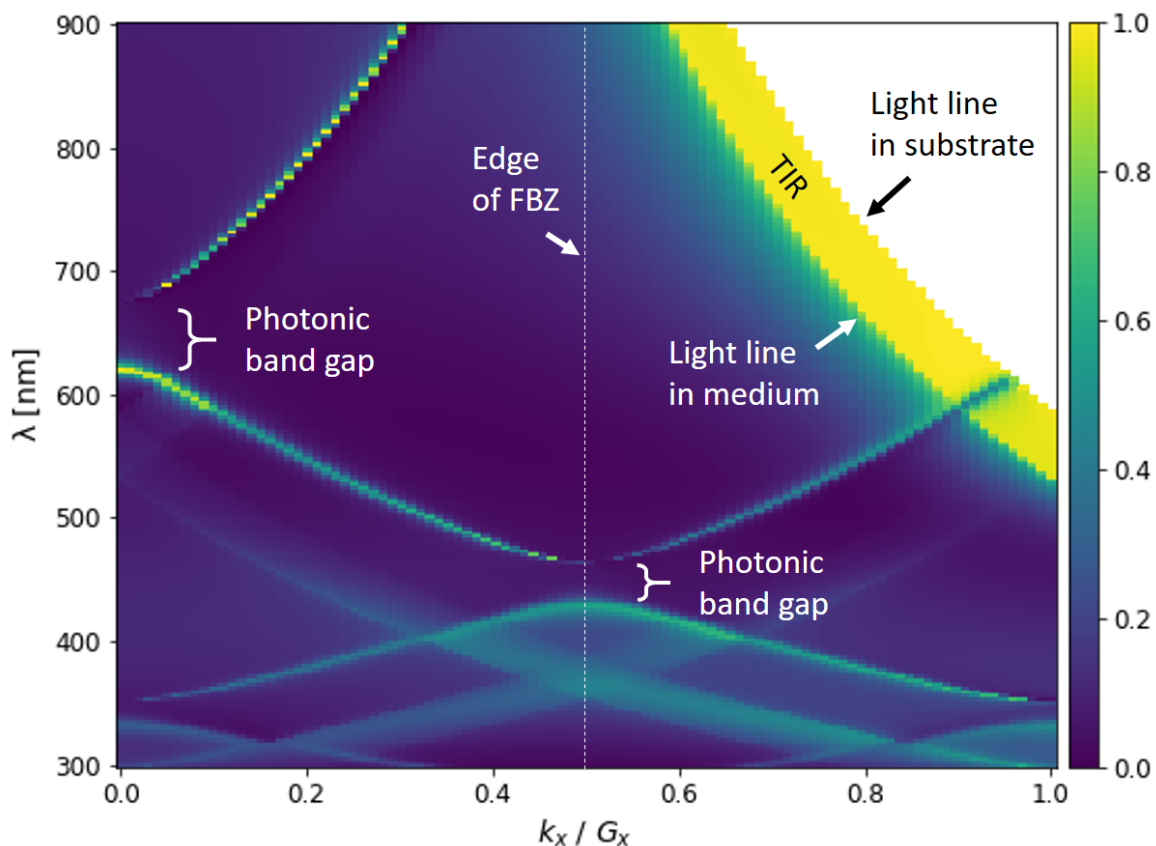
Figure 2.9: TE-polarised dispersion diagram of a GMR-grating, obtained by plotting the optical reflectance spectrum at different angles. Grating parameters: Period $a = 400$ nm, grating thickness t=150 nm, fill factor FF=0.75, grating material: Si_3N_4 , substrate: glass, medium: water. Incidence from substrate side.

to illustrate the folding of the bands.

The angle of incidence θ_x relates to the in-plane wave vector component as $k_x = k_n \sin(\theta_x)$. Only values of $k_x \leq k_n$ can be measured with this method, which corresponds to the light cone in the medium of index n. With incidence from the glass substrate side, a range of k_x is available in glass that can't propagate in the water medium. In this range, all the light will be reflected back into the glass eventually, which corresponds to TIR (section 2.4).

Note that here the y-axis is the wavelength λ, which means that lower band numbers are closer to the top in the figure. Several band gaps can be seen, e.g. at $\lambda \approx 650$ nm between the second and third band at the Γ-point, i.e. where $k_x = 0$. A higher harmonic of this gap is found at approximately half the wavelength, $\lambda \approx 350$ nm. The

band gap at the edge of the FBZ at $\lambda \approx 450$ nm is a higher harmonic of the lowest energy band gap, which was illustrated in the previous section. It is worth noticing that the wide TIR band folds back into the FBZ as well, but is not to be confused with the resonant modes.

In general, complete transmission and reflection is reached for resonances with incident angles inside the light cone, which only couple to in-plane waves that are outside the light cone. This regime corresponds to cases where only diffraction order zero exists inside the substrate and the medium, i.e. no light is lost to higher orders of diffraction, while the first diffraction orders $m = \pm 1$ within the grating layer match the resonant guided mode. Corresponding modes are found on either side of the first band gap at the Γ-point. They will be considered in more detail in the following section.

2.8.6 GMR Modes and BICs

The modes of interest for this work are located on either side of the first band gap at the Γ-point. The corresponding region in the dispersion diagram is shown in Fig 2.10 A). The two bands behave differently as they approach the Γ-point - the TE^{+1} mode at $\lambda = 620$ nm remains completely reflective and of similar width, whereas the TE^{-1} at $\lambda = 675$ nm becomes sharper until it disappears at $k_x = 0$.

An explanation for this disappearance can be found by examining the corresponding electric fields at a small incidence angle. Since the modes are TE-polarised, the only non-zero component of the electric field is E_y, whose real part is shown in Fig 2.10 B) for the TE^{-1} and Fig 2.10 C) for the TE^{+1} mode.

Remember that the coupling mechanism between light propagating in free space and the in-plane Bloch mode is provided by scattering at refractive index interfaces between the grating ridges and gaps. For the bright TE^{+1} mode at normal incidence, the two interfaces on either side of the gap experience the same field amplitude and phase, i.e. their scattered waves constructively interfere and can propagate out-of-plane. In contrast, the field of the TE^{-1} at normal incidence is anti-symmetric with respect to the centre of the gap, i.e. the waves from the two interfaces are of opposite phase and interfere destructively. As a consequence, no light can radiate out of the grating - this is a bound state in the continuum (BIC) [16].

As it is the symmetry that prevents coupling to the out-of-plane radiation, this state is a symmetry protected BIC. If the angle of incidence is slightly off-normal, the

symmetry is broken, and a small fraction of the light can couple out.

A similar behaviour is observed for the TM polarisation, the corresponding figure can be found in Appendix A.2.
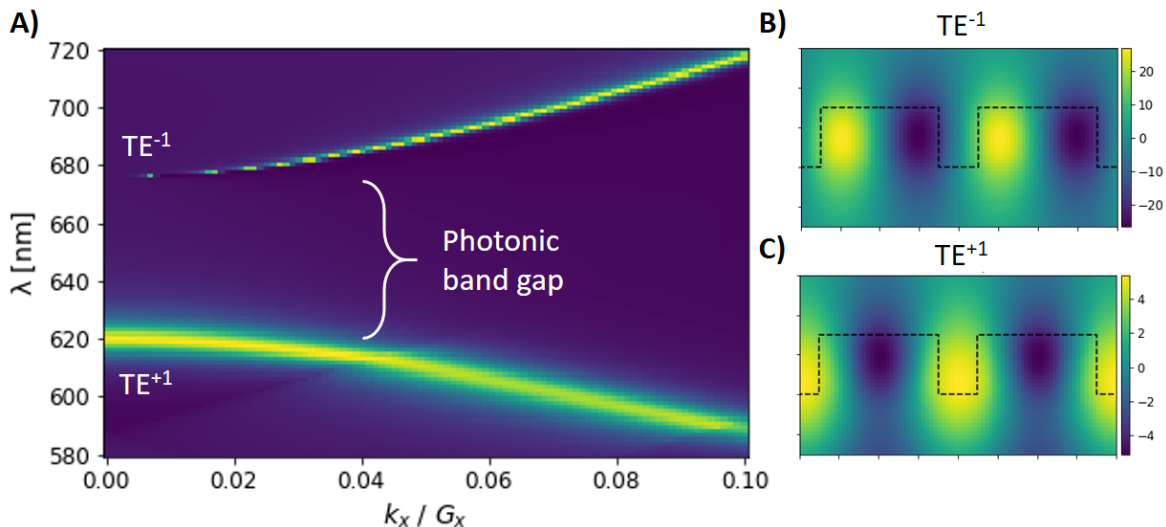
Figure 2.10: First band gap around the Γ-point and fields for a GMR-grating with TE-polarised light. A) Band diagram, showing the photonic band gap between two resonances. B) and C) Real y-component of the electric field of the TE^{-1} mode (at 0.5° incidence) and the TE^{+1} mode, respectively. Black dashed line: edge of the grating.

2.9 Fano Resonance

The resonance peaks in the reflection spectra of the GMR-grating are the result of an interference between the thin film response and the in-plane guided modes. The peaks are described by the Fano line shape [17]

$$F_0(\nu) = \frac{(q\gamma + \nu - \nu_0)^2}{\gamma^2 + (\nu - \nu_0)^2} \ , \tag{2.34}$$

with the frequency $\nu = \frac{1}{\lambda}$, half width γ and asymmetry parameter q. The latter contains information on the phase difference between the thin film and the guided mode. Note that in case $q = 0$, the peak is a symmetric Lorentzian peak.

When fitting the Fano equation to data from simulations or experiments, an amplitude A and offset B are used to take the sign and possible absence of normalisation

into account. The Fano equation becomes

$$F(\nu) = AF_0(\nu) + B \ . \tag{2.35}$$

Fig 2.11 shows a peak of the TE^{+1} and the TE^{-1} mode, both fitted with a Fano line shape with excellent agreement.
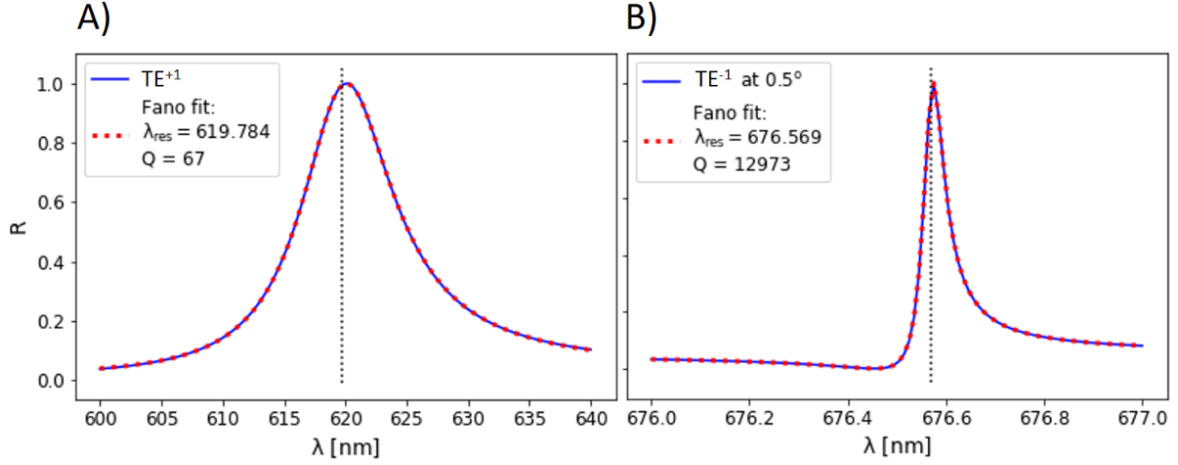
Figure 2.11: Simulated spectrum with fitted Fano for the TE^{+1} (A) and TE^{-1} (B) mode at $\theta_x = 0.5\,°$ incidence.

2.10 Q-factor

A resonance peak can be characterised by its quality factor Q [18], which is defined as

$$Q = 2\pi \frac{U}{\Delta U} \ , \tag{2.36}$$

with the energy U stored in the resonator and the energy ΔU dissipated per optical cycle.

Assume Q is a constant, and express ΔU in terms of the average temporal derivative of the energy

$$\Delta U = \frac{\dot{U}}{\nu_0} \ , \tag{2.37}$$

which leads to the differential equation

$$\dot{U} = \frac{2\pi\nu_0}{Q} U \ , \tag{2.38}$$

which shows that in absence of a source, the energy inside the resonator decays exponentially

$$U(t) = U_0 e^{-\frac{t}{\tau}} ,\tag{2.39}$$

where U_0 is a constant and

$$\tau = \frac{Q}{2\pi\nu_0}\tag{2.40}$$

is the exponential energy decay time.

An electric field oscillating at ν_0 and decaying in energy as Eq 2.39 can be expressed as

$$E(t) = E_0 e^{-\frac{t}{2\tau} + i2\pi\nu_0} .\tag{2.41}$$

Taking the Fourier transform of Eq 2.41 yields a Lorentzian line shape with a frequency half width at half maximum $\gamma = \frac{1}{2\pi}\frac{1}{2\tau}$, which allows to write the Q-factor as

$$Q = \frac{\nu_0}{2\gamma} .\tag{2.42}$$

For narrow peaks in a wavelength spectrum, the Q-factor can be expressed in terms of the resonant wavlength $\lambda_0 = \frac{1}{\nu_0}$ and the full width at half maximum $\Delta\lambda = \frac{2\gamma}{\lambda^2}$, yielding [11]

$$Q = \frac{\lambda_0}{\Delta\lambda} .\tag{2.43}$$

For the example TE^{+1} and TE^{-1} peaks in Fig 2.11, the Q-factors can be visually estimated as $Q \approx \frac{620 \text{ nm}}{10 \text{ nm}} = 62$ and $Q \approx \frac{677 \text{ nm}}{0.05 \text{ nm}} \approx 13\ 500$, respectively. These estimated values are in good agreement with the precise values of $Q = 67$ and $Q = 12973$ extracted from the Fano fit.

Note that the TE^{-1} mode is a BIC at the Γ-point, i.e. it is bound and has an infinite Q in an ideal system. As this point is approached ($k_x \to 0$), the Q-factor of the TE^{-1} mode continuously increases, which explains the high Q observed at the small incidence angle.

2.11 Purcell Effect

As seen in Eq 2.32, the GMR-grating provides a coupling mechanism between waves travelling in opposite directions inside the grating layer, able to form closed paths. The grating can therefore be considered as a distributed cavity.

Consider a quantum system, such as an atom or molecule, that can spontaneously emit light by undergoing a transition from a higher energy state to a lower energy state.

Fermi's golden rule [19] states that the rate of spontaneous emission is proportional to the density of states (DOS), which describes the number of states available for a given energy.

The DOS inside a resonant cavity can be higher than the DOS in free space, i.e. the spontaneous emission of the emitter can be enhanced by the cavity. If the emitter spectrally overlaps with the cavity and emits in the same polarisation as the cavity resonance, the enhancement is quantified by the Purcell factor [20]

$$F_p = \frac{3}{4\pi^2} \left(\frac{\lambda_0}{n} \right)^3 \frac{Q}{V}, \tag{2.44}$$

where λ_0 is the wavelength in vacuum, n the effective index, Q the quality factor and V the mode volume.

The Purcell factor can be estimated for the resonances shown in Fig 2.11, assuming a mode volume equal to the cubed effective wavelength, i.e.

$$F_p \approx \frac{3}{4\pi^2} Q \ , \tag{2.45}$$

which yields an enhancement factor of $F_p \approx 5$ and $F_p \approx 1000$ for the TE^{+1} and the TE^{-1} mode, respectively.

2.12   Q-matching

According to the previous section, a higher radiative Q-factor Q_r leads to stronger enhancement. However in practice the Q-factor is limited by non-radiative losses, such as scattering losses from material roughness and impurities, or absorption loss of the materials.

The non-radiative losses can be described by a separate factor Q_{nr}, which describes how quickly a mode decays due to the losses.

The total Q-factor is then given by

$$Q_{tot} = \frac{1}{\frac{1}{Q_r} + \frac{1}{Q_{nr}}} \ . \tag{2.46}$$

If $Q_{nr} << Q_r$, a large number of photons is lost before radiating into the cavity mode. In contrast, if $Q_{nr} >> Q_r$, the radiative Q_r could be further increased for better enhancement. Q-matching is a condition for which an optimum emission is obtained, corresponding to $Q_r = Q_{nr}$ [21, 22].

Chapter 3

Fabrication & Sample Characterisation

3.1 Introduction

All samples made for this thesis consist of a substrate on top of which one patterned layer of high index dielectric material is fabricated by e-beam lithography (EBL) and dry etching. The aim is to obtain samples that support resonant modes in the visible wavelength range. This chapter starts with general material considerations, followed by an overview and explanation of the different nanofabrication steps involved. Finally, it is shown how the resulting samples are characterised by means of scanning electron microscopy (SEM) and their optical spectra.

3.1.1 Fabrication

The samples described in this thesis consist of a substrate covered with a thin film of higher index material, in which guided modes can be supported; a typical example being a glass substrate coated in silicon nitride (Si_3N_4) acting as the waveguide layer. In order to obtain guided mode resonances (GMRs), this layer is patterned by removing material with regular spacing in one or two dimensions, resulting in 1D or 2D optical gratings. In order to understand the scale of these features, let's recall that a guided mode resonance can be described by its effective refractive index

$$n_{eff} = \frac{\lambda}{a},$$

(3.1)

where λ is the wavelength and a is the grating period at resonance. Since the effective index is a weighted average of the refractive indices of the grating, the substrate and the medium, its value is typically of the order of $n_{eff} = 1.55 - 2$. This means that in order to obtain resonances in the visible wavelength range of $\lambda = 400 - 700$ nm, periods of only a few hundreds of nm are required. As a consequence, the desired size of the regularly spaced grating troughs or holes is typically of order 100 nm. An appropriate technique for the creation of such small features is the technique of e-beam lithography (EBL), which can produce features as small as several tens of nm. In EBL, the pattern of interest is written into a resist with a focused beam of electrons. In case of positive resist, the areas where the resist is exposed will undergo a chemical transformation that makes it soluble to the developer, while the unexposed areas stay insoluble. During the development step, the exposed pattern is then dissolved, and the remaining resist acts as a protective mask, so that only the exposed pattern is etched into the high index layer during the reactive ion etching (RIE) step. Details of the individual fabrication steps are described in section 3.2.2.

3.1.2   Sample Characterisation

Once a sample is obtained after the EBL and RIE steps (section 3.2.2), it is ready to be used for the experiment. We first structurally and spectroscopically characterise the sample to make sure the pattern dimensions match the design and the optical properties agree with the simulations. Sample characterisation is particularly important when making new types of patterns that have not been fabricated before.

The dimensions of the patterned layer can be verified by examining the sample under a microscope. The high resolution required to image the small features can be achieved by scanning electron microscopy (SEM). Similar to the EBL system, a focused beam of electrons is used. However, it is now scanned over a complete field of view on the sample. By measuring and recording the current generated by scattered electrons as a function of beam position, an intensity image can be constructed.

Another important characterisation method is to examine the optical response of the sample and to verify that it does indeed support the resonances that it was designed for. GMR modes can readily be identified by their peaks (dips) in the reflection (transmission) spectrum. The setup and technique used for obtaining the spectra are described in section 3.2.4.

Once the spectra are measured, they are compared to the simulations that were per-

formed during the sample design, which allows assessing the quality and understanding possible issues with the fabricated sample.

3.2 Materials and Methods

3.2.1 Substrate and High Index Materials

First of all, an appropriate substrate material is chosen. The resonant modes of the GMR grating are excited by out-of-plane illumination, which means that the experiments can be carried out either in transmission or in reflection. For transmission experiments, a transparent substrate is necessary. If the substrate is opaque, it is only possible to perform experiments in reflection - illuminating and measuring from the same side. However, it is often advantageous to separate the optical path from the fluidic path, in which case one preferably illuminates through a transparent substrate and arranges the fluidics on the other side. Additionally, for the optical modes to experience a minimum of scattering loss and to exhibit the highest possible Q-factor, we need a high quality substrate with very small surface roughness. Additionally, the substrate material should be free of absorption losses for the wavelength of interest. Since glass can satisfy all of these conditions, I chose it as the substrate for this work.

The thin film that is placed on top of the substrate to support the guided mode must have a refractive index that is higher than that of the substrate and the medium in which experiments are to be performed - otherwise, neither the guided modes nor the desired resonances will be supported. In addition, the material for this layer should be free of absorption losses. Silicon nitride (Si_3N_4), with its index of ~ 2 in the visible range [23], satisfies these conditions. In addition, it is not only mechanically robust, but also of good chemical and biological inertness [24], which is of interest when chemically functionalising the surface or performing biological experiments.

The Si_3N_4 on glass wafers used for this work are commercially acquired (Silson, UK). The Si_3N_4 layers are 150 nm thick and produced using a chemical vapour deposition method on 500 um thick glass substrates. The wafers are diced into 15 x 15 mm^2 chips, after which they are ready for the nanofabrication steps described in the following section.

3.2.2 Nanofabrication Steps

The main fabrication steps for patterning the high index layer are schematically illustrated in Fig 3.1. Detailed information on each step is given below.

A) The sample is first cleaned by placing it in an ultrasonic bath in acetone (ACE) for 10 min, followed by a rinse in isopropanol (IPA). The sample is then blown dry with nitrogen gas.

B) The positive resist for the electron beam exposure (AR-P 6200.13, Allresist GmbH) is spun at 5000 rpm for 1 min and baked on a hotplate at 180 °C for 5 min. Since the substrate and the thin film are dielectric, they are not able to dissipate the charge that will be created during exposure to the electron beam. The resulting charging of the surface would lead to localised charging, thus deflecting the beam. To prevent charging, a charge dissipation layer (AR-PC 5090, Allresist GmbH) is spun at 2000 rpm for 1 min and baked at 90 °C for 2 min.

C) The e-beam exposure is performed on a Voyager EBL system (Raith GmbH), with an accelerating voltage of 50 kV, a beam current of 140 pA and a base dose of 135 µC cm^{-2}. The base dose is multiplied by the dose factor. Initially, several replicas of a given pattern are be exposed, each with a different dose factor. With such a dose test, the optimal factor that yields the desired features, is determined.

D) The charge dissipation layer is removed by immersing the chip in deionised (DI) water at room temperature for 2 min. The exposed pattern is then developed in Xylene at room temperature for 2 min, which is quenched by rinsing the chip in IPA.

E) The pattern is etched into the Si_3N_4 layer using a plasma-based RIE system. A constant gas flow of CHF_3 (58 sccm) and O_2 (2 sccm) is used, with a bias voltage of 360 V and chamber pressure of 0.19 mbar, etching for 7 min.

F) The remaining resist is removed with MICROPOSIT Remover 1165 (A-Gas Electronic Materials, UK) in a gentle sonication bath at 50 °C for 10 min. Finally, the sample is rinsed in ACE and IPA, then again blown dry with nitrogen gas.
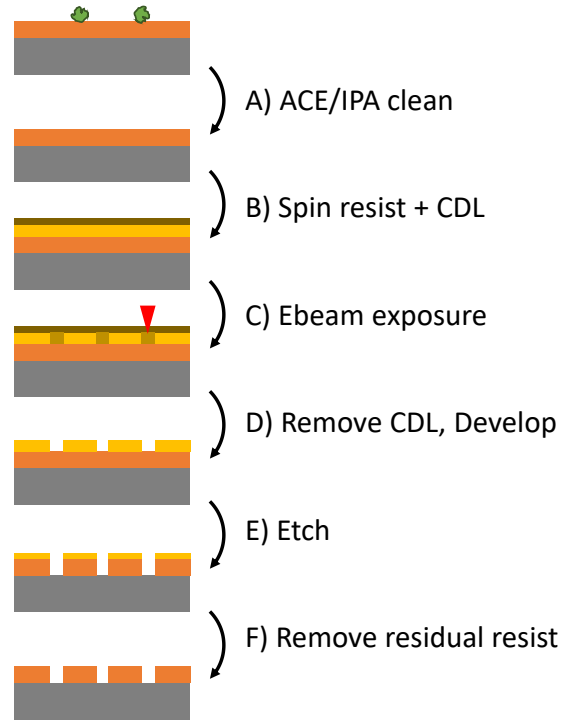
Figure 3.1: Schematic of the main fabrication steps used for patterning the high index layer to obtain the resonant gratings. ACE: acetone, IPA: isopropanol, CDL: charge dissipation layer.

3.2.3   Scanning Electron Microscopy

The SEM system used for this work is the JEOL 7800F Prime SEM, located in the York JEOL Nanocentre.

As before, charge accumulation is an issue also when imaging the sample with an electron microscope, so I applied another charge dissipation layer. For imaging, this layer should be as thin as possible, so we apply a 5-10 nm layer of platinum/palladium by sputter deposition. It is worth noting that the CDL cannot be removed without damaging the sample, which means that no experiments can be performed on any sample once it has been imaged with the SEM.

3.2.4   Optical Characterisation

Since the resonances are usually designed with water as the medium, it is advantageous to measure the reflection spectrum by illuminating and collecting from the substrate

side on an inverted microscope setup. This configuration means that a sample can simply be placed on the microscope stage and a drop of water is placed on top of it with a syringe or pipette - no need for any advanced fluidics, such as channels or wells.

The reflection spectrum can then be obtained in different ways. If the resonant structure to be measured is large enough to fill the entire field of view (FoV) of the microscope, within which all grating parameters are constant, the spectrum can be analysed directly by collecting all the light and passing it through a spectrometer. Although this method is simple and quick, it does not provide any spatial information.

If both spatial and spectral information is required, the illumination light can be filtered, in order to effectively illuminate the sample with a "single" wavelength. For each wavelength inside a range of interest, a microscope image is then acquired. This means that the resulting image stack of frames has the spatial information in the x and y pixel coordinates, and each frame number corresponds to a certain wavelength that was used to illuminate, i.e. for each point in space (x,y) a wavelength spectrum is recorded.

Here, I used a halogen lamp that is spectrally filtered with a grating monochromator. The working principle of such a monochromator is the following: A broad spectrum of light enters the monochromator through a narrow slit; the light is collimated and reflected onto a diffraction grating with a parabolic mirror. It then leaves the monochromator through an exit slit at a fixed angle. Since the angle of diffraction for any non-zero order depends on the wavelength, it is possible to choose the angle of the grating such that the first diffraction order for the wavelength of interest can pass the exit slit. The width of the exit slit determines how narrow the spectrum of the filtered light is, i.e. for a high spectral resolution, the slit must be narrow. However, the slit cannot be narrowed down indefinitely, since at some point the intensity will get so small that no light can be detected at all. As a rule of thumb, the illumination spectrum can be considered narrow enough if the resonance peak to be resolved is several times wider.

A schematic of the setup used for measuring the reflection spectra of the samples is shown in Fig 3.2. Light emitted from a Halogen lamp (TLS-72-Q250, Photonic Solutions) is filtered using a monochromator (9072, Photonic Solutions) and passes through a lens (KL) that focuses it in the centre of the back focal plane (BFP) of an objective lens after being reflected from a beam splitter cube (BS). This so-called Köhler illumination creates a collimated beam illuminating the sample at normal incidence.
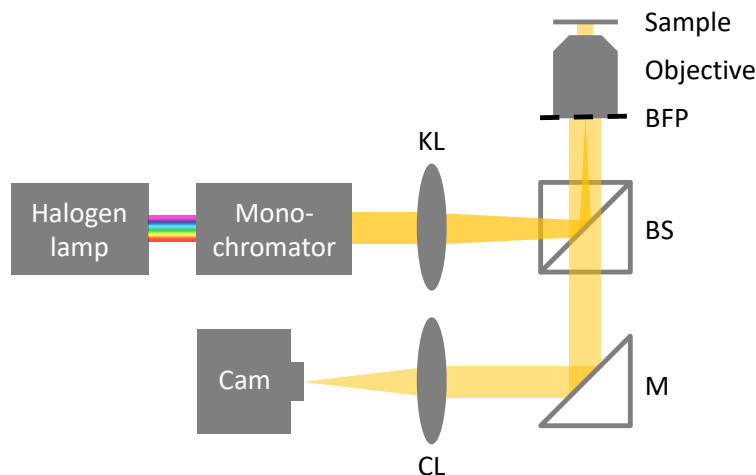
Figure 3.2: Schematic of the setup used to spatially resolve the reflection spectrum of the resonant samples. KL: Köhler lens, BS: beam splitter, BFP: back focal plane of the objective, M: mirror, CL: camera lens.

Light returned from the sample is collected by the objective, passes through the beam splitter and is focused onto the camera by a second lens (CL).

In cases where a measured spectrum shows a background that is not constant, for example due to the non-uniform spectrum of the illumination light, I used a background normalisation. If only the peak position and width are of interest, a quick and reliable way to perform the normalisation is to divide the spectrum of the grating by the spectrum of an unpatterned region on the chip. This removes not only the effect of the source, but also the thin film contribution of the measured spectrum. If, however, the absolute reflectance values of the entire sample are required, e.g. when wanting to compare it to the simulation, the grating spectrum is normalised against the spectrum of a mirror, which is acquired and computed separately.

3.3 Results

3.3.1 Scanning Electron Microscopy

Example SEM images of a 1D optical grating fabricated in Si_3N_4 on glass are shown in Fig 3.3 for different dose factors $DF = 1.15$ (A) and $DF = 1.3$ (B). The design pattern has a period of 450 nm and fill factor of 0.75. The fill factor is defined as the

A)

B)
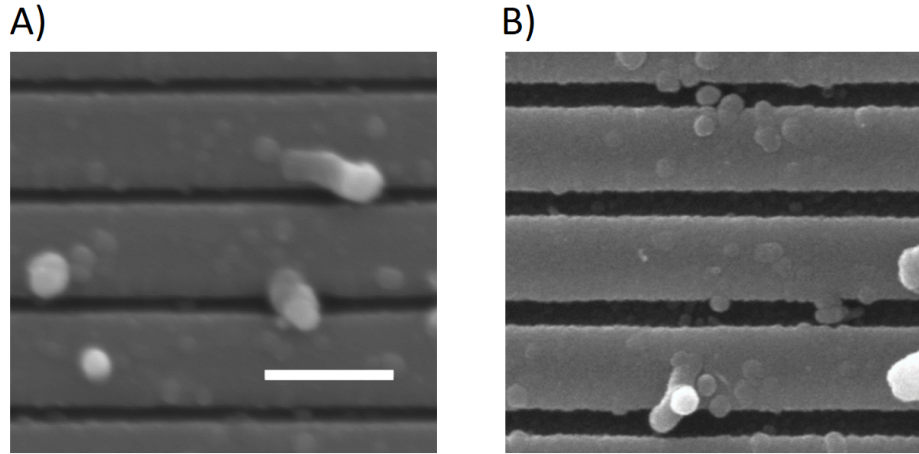
Figure 3.3: SEM micrograph of a 1D grating in Si_3N_4 on a glass substrate. Design period 450 nm, fill factor 0.75. Dose factor 1.15 (A) and 1.3 (B). SEM parameters: Magnification 50 000x, working distance 20 mm and acceleration voltage 5 kV. Scale bar 500 nm.

ridge width divided by the period, so it describes the fraction of high-index material. The grating ridges appear as bright horizontal stripes, and the thinner dark stripes between them correspond to the etched gaps. As desired, the gaps are well etched, with a constant width and without any bridging between the ridges. With the help of the scale bar included in the micrograph (500 nm), one can confirm that the correct period of 450 nm is obtained. With a dose factor 1.15 the gap is approximately 60 nm, yielding a fill factor of ~ 0.86, which is too high. However, with a dose factor of 1.3, a gap of 110 nm is obtained, corresponding to the target fill factor ~ 0.75. The 10 - 100 nm sized, round particles apparent on the micrograph are impurities.

3.3.2   Optical Reflection Spectrum

A selection of images and the resulting reflection spectrum measured with the monochromator setup (Fig 3.2) are shown in Fig 3.4. The grating with constant period is situated in the centre of the field of view, surrounded by unpatterned Si_3N_4. Between two consecutive points, the illumination wavelength is increased by 2 nm, covering a range of $\lambda = 520$ - 700 nm. The background normalised spectrum is obtained by dividing the mean intensity on the grating by the mean intensity of the unpatterned layer. At the wavelength of $\lambda \approx 600$ nm, corresponding to the centre of the resonance peak, the grating appears brightest.
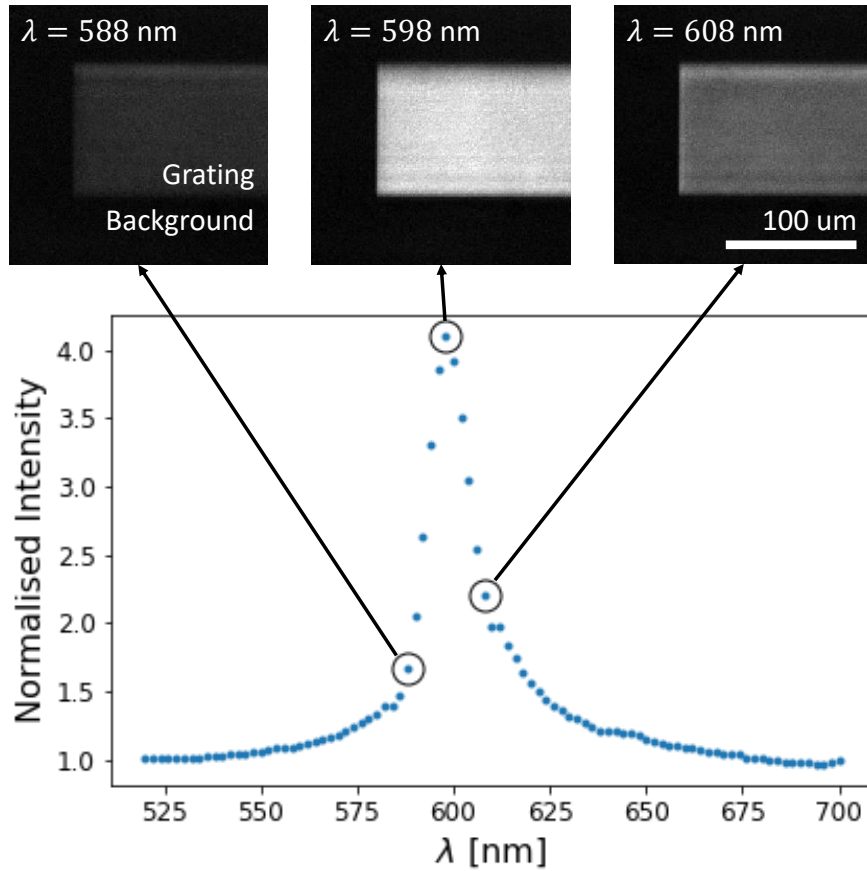
Figure 3.4: (Top) Selection of images of a 1D GMR grating with a constant period, acquired with the monochromator setup at various wavelengths λ in TE polarisation. (Bottom) Computed spectrum obtained by normalising the average graylevel in the grating region by the average graylevel of unpatterned Si_3N_4 background.

The identification of the resonance peak can be simplified by using chirped gratings [25]. Since a resonance is described by its effective index (Eq 3.1), it can be identified by either fixing a period and scanning the wavelength as described above, or the other way around - by fixing a wavelength and scanning the period. A schematic of a chirped grating that represents such a period scan is shown in Fig 3.5 A). In this design, the period increases as the x-coordinate increases, i.e. the grating ridges spread out like a fan, while the fill factor is kept constant. The spectral information of the resonance is encoded in space: When illuminated with a single wavelength that lies within the range of the chirped grating, a bar lights up at the x-coordinate corresponding to the resonant period, see example images in Fig 3.5 B) and C), acquired using a 4x and 20x
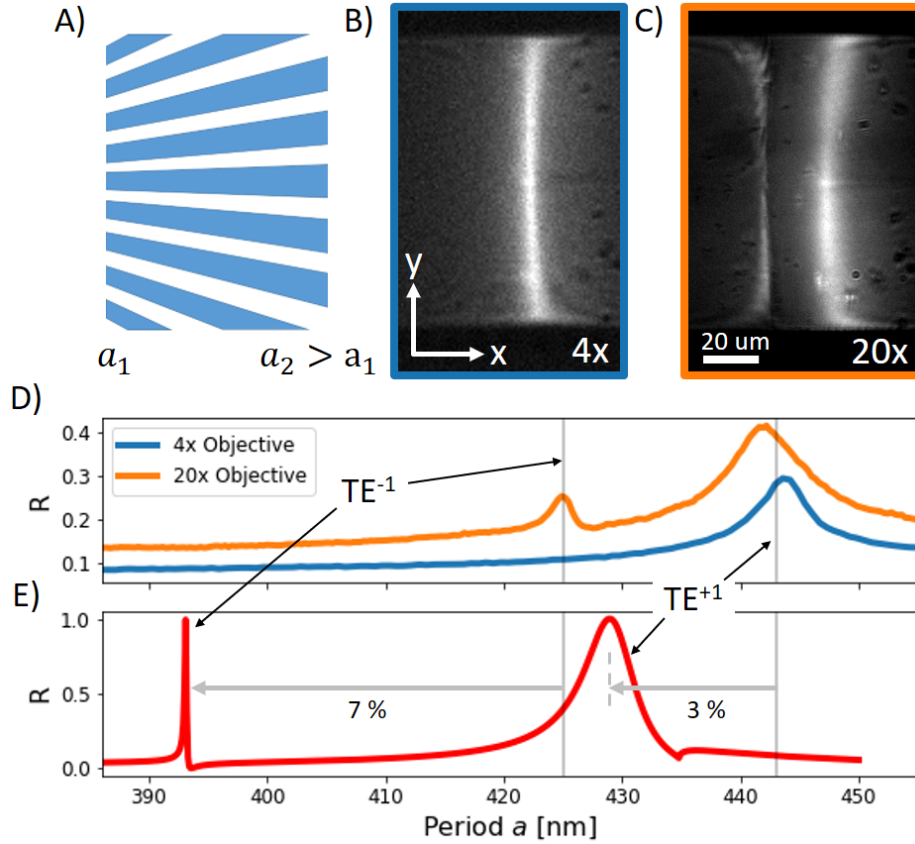
Figure 3.5: A) Schematic of the chirped grating design with the period linearly increasing along the x-axis. B) and C) Example images of a chirped grating in Si_3N_4 with a nominal fill factor of 0.75, acquired on a monochromator setup at wavelength $\lambda = 650$ nm, TE-polarised. The images show the same field of view with a 4x and 20x objective, respectively. Images are normalised to a mirror. D) Period spectrum obtained by averaging the graylevel of the central region of the grating along the y-axis. E) Simulated spectrum at a small incidence angle $\theta = 1°$. Si_3N_4 index $n = 1.9653$; fill factor 0.75.

objective, respectively. Both images show the bright TE^{+1} GMR mode, but with the higher magnification objective, a second peak is observed, which corresponds to the TE^{-1} mode. Note that the upper and lower edges of the grating affect the resonances, but this effect fades out when approaching the centre of the grating.

A "period spectrum" can be obtained by averaging the graylevel of the mirror normalised images along the y-axis, see Fig 3.5 D). A region of interest is used to select the centre of the grating only, excluding the edge effects. Same as for the wavelength spectrum presented above, the resonance peak is revealed, but this time only requiring

48

the image at one single wavelength. The TE^{+1} peak is at period $a \approx 445$ nm, and the TE^{-1} at $a \approx 425$ nm.

The spectrum simulated for the initial design of the grating is shown in Fig 3.5 E), where a refractive index of Si_3N_4 of $n = 1.9653$ is used. The index was measured[1] on a pristine Si_3N_4 film with a film analyser system (Filmetrics F20). The corresponding spectrum shows peaks for both modes, but at 3% (TE^{+1}) and 7% (TE^{-1}) lower periods than observed in the experiment.

3.4   Discussion & Conclusion

In this section, I have described the fabrication of optical gratings that support GMR resonances in the visible wavelength range. The dimensions of the grating ridges were verified using SEM images. The resonance peaks in the reflection spectrum were measured by either considering a grating of fixed period and scanning the wavelength, or by fixing the wavelength and using chirped gratings to scan a range of periods. The period spectrum measured with a 20x objective not only shows the bright TE^{+1} mode, but also the TE^{-1} mode. Since the latter cannot be seen at normal incidence (see chapter 2), it can be concluded that the illumination beam contains larger angles than with the 4x objective, i.e. the beam with the 20x objective is less collimated.

The measured spectra agree with the simulations, as they both show the TE^{+1} and TE^{-1} mode on the red and blue side of the band gap, respectively. The measured peaks are at 3-7 % longer periods, which means they have a slightly smaller effective index, which can have various origins:

- The fill factor may be overestimated, as the charge dissipation layer of $5 - 10$ nm, deposited for the SEM imaging, can make the gap appear up to ~ 20 nm smaller. In this case, the true fill factor would only be ~ 0.71.

- The sample is deliberately over-etched, i.e. we etch deeper than the exact 150 nm of the Si_3N_4 layer, in order to make sure it is completely etched through. This is not taken into account in the simulations.

- The etching is not perfectly directional, which can lead to rounded edges of the grating ridges.

---

[1]Thanks to Sam Blair for his assistance with this measurement.

The absolute reflectance values in the measured spectra only reach 20-25% from baseline to the peak maximum, instead of the expected 90-100% observed in the simulations. Possible reasons are given by an incident beam that is not perfectly collimated and scattering loss due to surface roughness experienced by the leaky guided modes.

Chapter 4

Interferometric Scattering Microscopy

4.1 Introduction

Interferometric scattering microscopy (iSCAT) is an optical microscopy technique whereby the contrast arises from light scattering and interferometry. Due to the interferometric detection and appropriate image processing, iSCAT is highly sensitive and can detect single proteins. Since its introduction in 2004 [26] it has grown into an established imaging technique, with main applications in single particle tracking and mass photometry.

To start this chapter, the general working principle of iSCAT is explained (section 4.1.1), followed by a brief description of the expected signals (section 4.1.2). Sources of noise and methods to address them are considered in section 4.1.3. The properties of the objective back focal plane (BFP) are explained in section 4.1.4. The following section 4.1.5 describes not only how these properties can be used to enhance the iSCAT signal, but also briefly discusses a range of other enhancement approaches found in the literature, including optical gratings. To conclude the introduction, two main applications of iSCAT are described in sections 4.1.6 (single particle tracking) and 4.1.7 (mass photometry).

The introduction is followed by section 4.2, which shows how a first iSCAT setup was built, various aspects of it tested and optimised. A first test is carried out to make sure that the camera and its control software reach the intended speed (section 4.2.1).

The first version of the setup is then presented (section 4.2.2), followed by observations of mechanical noise due to the stage and how it was improved (section 4.2.3). Relatively large particles are imaged with iSCAT and confirmed with simultaneous fluorescence microscopy images (section 4.2.4). The particle size is then decreased in order to characterise the limits of the setup (section 4.2.5).

Implementations of the popular method of numerical aperture (NA) filtering for enhanced iSCAT are considered in section 4.3. A first approach, where a partial reflector takes the place of the beam splitter, is described in section 4.3.1. A more elaborate approach consists of imaging and manipulating the BFP of the objective. The implemented setup modification is described in section 4.3.2. Correct imaging of the BFP is tested in an experiment, where the maximal collected emission angle allowed by the NA of the objective and the critical angles for total internal reflection (TIR) are measured (section 4.3.3). Finally, NA-filtering with partial reflectors in the imaged BFP is demonstrated (section 4.3.4).

4.1.1 Working Principle

In the simplest form of iSCAT, a particle to be imaged on a glass substrate is illuminated with a collimated laser beam from below in an inverted microscope configuration, see schematic in Fig 4.1. The collimated beam is obtained by focusing a laser beam in the BFP of the objective lens via a beam splitter. The incident beam is reflected on the substrate-medium interface with a reflectivity r and travels back down through the beam splitter towards the imaging system. In addition to this reference signal, scattered light from the particle with a scattering amplitude s (complex number) is collected by the objective. The resulting intensity measured at the detector is given by

$$I = I_0(r^2 + |s|^2 + 2r|s|\cos\phi), \tag{4.1}$$

where I_0 is the intensity of the incident light and ϕ is the phase difference between the reflected and the scattered light. The signal consists of three terms, which correspond to the pure reflection term, the pure scattering term and the interference term.

If the particle diameter D is small compared to the wavelength, i.e. $D \ll \lambda$, and is approximately spherical, the scattering amplitude s is proportional to the polarisability [27, 28],
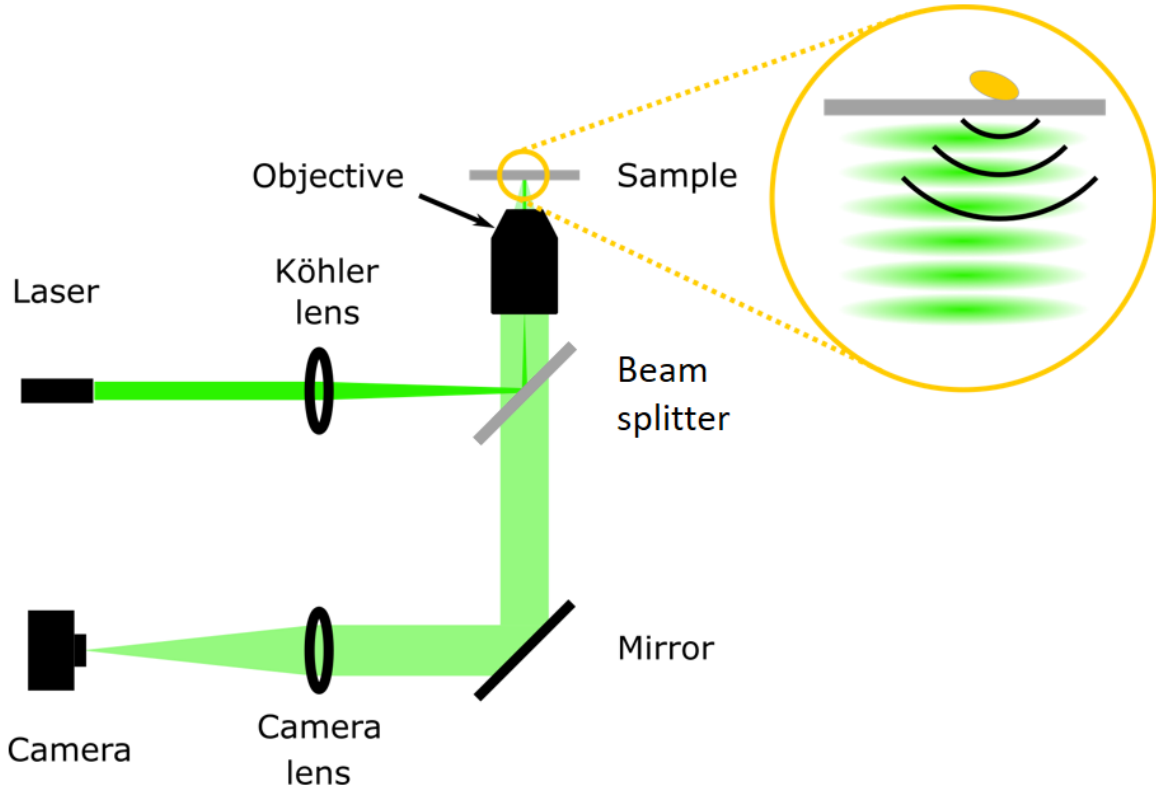
Figure 4.1: Schematic of a simple iSCAT setup. A laser beam passes a Köhler lens, which focuses it in the back focal plane of the objective after a reflection at the beam splitter. The inset illustrates the incident collimated beam and its reflection in green, and scattered light from the yellow particle in black. Both the reflected and scattered light travel through the beam splitter, after which an image is formed on the camera sensor by the corresponding lens.

$$\alpha = 3V\epsilon_m \frac{(\epsilon_p - \epsilon_m)}{\epsilon_p + 2\epsilon_m}, \tag{4.2}$$

with the particle volume V and complex dielectric constants ϵ_m and ϵ_p of the medium and particle, respectively. This corresponds to the Rayleigh scattering regime, where the scattering cross-section [27] is related to the polarizability as

$$\sigma_R = \frac{8}{3\pi^2}|\alpha|^2\lambda^{-4} \ . \tag{4.3}$$

It is interesting to evaluate Eq 4.2 for two common materials, such as gold and polystyrene, in order to highlight their different scattering characteristics. Considering

a wavelength of 520 nm, the dielectric constant for gold is given by

$$\epsilon_{gold}(\lambda = 520 \text{ nm}) = (n_{gold} + ik_{gold})^2 = (0.635 + 2.07\ i)^2\ , \tag{4.4}$$

and for polystyrene it is

$$\epsilon_{polystyrene}(\lambda = 520 \text{ nm}) = (1.6 + 0\ i)^2, \tag{4.5}$$

with real (n) and imaginary (k) parts of the refractive indices obtained from [15]. With a water medium of $\epsilon_m = 1.333^2$, the corresponding polarisabilities per volume are given by

$$\frac{|\alpha_{gold}|}{V} = 8.06 \tag{4.6}$$

and

$$\frac{|\alpha_{polystyrene}|}{V} = 0.939\ , \tag{4.7}$$

which show that the iSCAT signal for a given particle size is expected to be almost and order of magnitude stronger for gold than for polystyrene.

The pure scattering term $|s|^2$ in Eq 4.1 is proportional to V^2, and therefore becomes negligible for small particles. The interference term, used in iSCAT, only varies linearly with V, and therefore decreases less rapidly when decreasing the particle size, which explains why iSCAT is particularly useful for detecting small particles.

In practice, the acquired iSCAT images are divided by a background image in order to remove the effects of illumination inhomogeneities. This is called flat fielding [29]. For weak scatterers, the resulting normalised signal is given by

$$\tilde{I} = 1 + \frac{2|s|}{r}\cos\phi\ , \tag{4.8}$$

which shows that the contrast is mainly determined by the ratio $\frac{|s|}{r}$.

4.1.2 Point Spread Function

The image of a scatterer that is much smaller than the illumination wavelength is given by the point spread function (PSF). To estimate the PSF of a point-like scatterer, one can consider the optical field of a diffraction limited spot created by the objective when its back aperture is filled with light. The corresponding field in the front focal plane is described by the Fourier transform of the aperture (see section 4.1.4). With a circular

aperture, a so-called Jinc function is obtained (see Fig 4.2, left),

$$\text{Jinc}(\rho) = \frac{J_1(\rho)}{\rho}, \tag{4.9}$$

where J_1 is the Bessel function of the first kind of order one, and ρ represents the lateral radial distance from the centre.
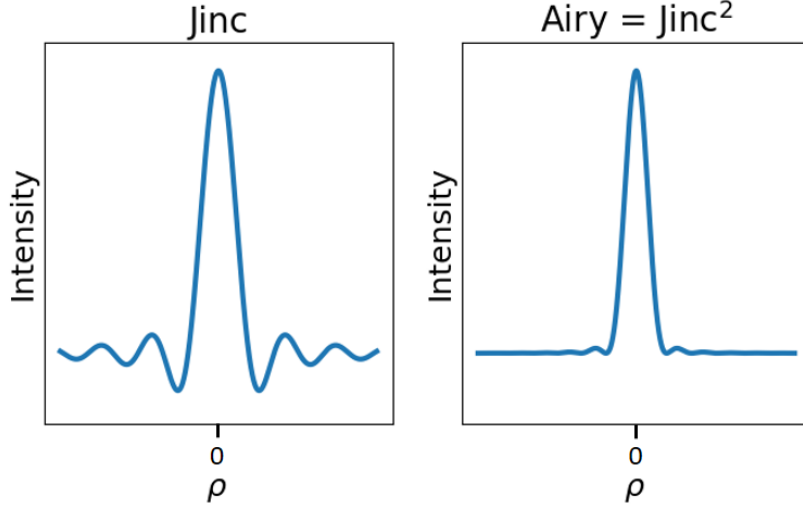
Figure 4.2: (left) Jinc function to approximate the iSCAT PSF. (right) Airy pattern, the PSF observed in dark field microscopy. The radial displacement with respect to the PSF centre is denoted ρ.

In the iSCAT regime, the PSF is determined by the interference term and therefore linear with the scattered field, i.e. it is comparable to the Jinc function directly, with its rings that decay as $1/\rho$. It is important to note that the Jinc is only an approximation of the iSCAT PSF, whose exact shape and sign also depend on the phase difference ϕ between scattered and reflected light, and therefore on the scatterer material and position, focus position and aberrations [30].

By comparison, in dark field microscopy, only the pure scattering term $\propto |s|^2$ is detected, and the intensity pattern of the PSF is obtained by squaring the scattered amplitude. The corresponding squared Jinc function is well known as the Airy pattern (Fig 4.2, right). Note that compared to the Jinc function, the Airy pattern has rings that are much weaker than the main central peak.

The radius ρ_{min} from the central peak to the first minimum of the Airy pattern

relates to the NA of the objective as

$$\rho_{min} = \frac{0.61\lambda}{\text{NA}} \ , \tag{4.10}$$

which is often used to describe the resolution of a diffraction limited imaging system.

4.1.3 Noise Considerations

As iSCAT is a highly sensitive imaging technique, it is important to suppress noise as much as possible. Static noise can simply be removed by background normalisation, where one way of obtaining the background image is given by taking the temporal median of the acquired video. However, time dependent noise requires more attention. The latter can come from a range of sources, such as vibrations, mechanical drift, dirt particles in the beam path or in the sample, interference from surfaces of the optics or the liquid-air interface of the sample itself, and readout noise of the camera [29].

An elegant improvement compared to the simple wide-field illumination setup (Fig 4.1) is given by the beam scanning setup, where the illumination beam is loosely focused on the sample and rapidly scanned across the entire FoV several times during the exposure of a single acquired frame, using accousto-optic deflectors. This reduces speckle noise, any effects of out-of-focus interfaces and objects, and the extended rings of the iSCAT PSF. [31]

When all addressable sources of noise have been sufficiently suppressed, a shot-noise limited detection is possible [31, 32]. Shot-noise is due to fluctuations in the discrete number of photons that are detected, and follows a Poisson distribution. This means that the signal is proportional to the number of photons N_{ph}, and the noise amplitude is given by $\sqrt{N_{ph}}$, which yields a signal-to-noise ratio of

$$SNR = \sqrt{N_{ph}} \ . \tag{4.11}$$

In a shot-noise limited regime, the SNR can therefore be improved by simply increasing the number of photons detected per frame, i.e. by increasing the illumination intensity. However, the camera sensor will saturate at a certain intensity. If this point is reached, temporal averaging can push the SNR even further. In order to do so, the acquisition frame rate is sped up by a factor m of the target frame rate, and the resulting image stack is then average binned in time, with bin size m. Higher frame

rates will require smaller integration times, which means that the illumination intensity can be increased by the same factor m without saturating the detector. The resulting binned frames contain m times more photons, which in a shot-noise limited system increases the SNR by $\sqrt{m}$.

4.1.4 Properties of the Back Focal Plane

As will be seen in the following section, the BFP can be accessed and manipulated in order to enhance the iSCAT contrast. The current section describes the relation between the front focal plane (FFP) and the BFP of a lens, as illustrated in Fig 4.3. In case where the lens is a simple bi-convex lens, the front focal distance f_F and the back focal distance f_B are the same; for a more complex composite lens system like the oil immersion objective used here, f_F and f_B can differ by as much as an order of magnitude.
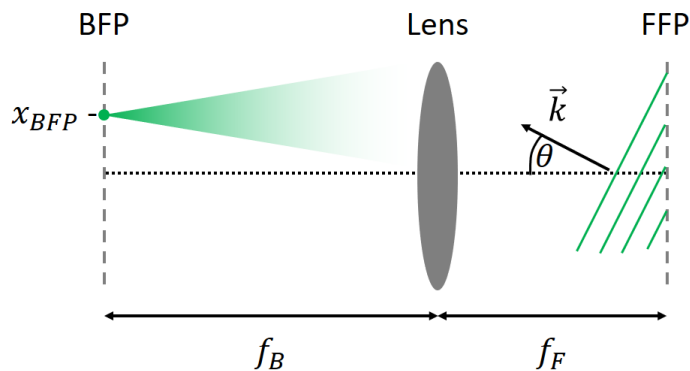
Figure 4.3: Schematic of a lens system. The back focal plane (BFP) shows the Fourier transform of the front focal plane (FFP). A spatial frequency k_x in the FFP relates to a specific plane wave emission angle θ_x in the FFP, and is proportional to the coordinate x_{BFP} in the BFP.

The lens collects light from the FFP. Let's first consider the x-axis, which corresponds to the vertical in-plane axis in the figure. The same relation holds along the y-axis, i.e. in the out-of-plane direction of the figure.

The intensity distribution in the FFP can be composed of a range of spatial frequencies $\nu_x = \frac{k_x}{2\pi}$, where each frequency corresponds to a plane wave with diffraction angle θ_x, as

$$\nu_x = \nu_n \sin(\theta_x), \tag{4.12}$$

57

where $\nu_n = \frac{k_n}{2\pi} = \frac{nk_0}{2\pi} = \frac{n}{\lambda_0}$, and k_n is the wavenumber in the medium of refractive index n, and λ_0 is the wavelength in vacuum.

As known from Abbe's theory of imaging [33], the intensity distribution in the BFP corresponds to the Fourier transform $F(\nu_x)$ of the FFP [34], with

$$\nu_x = \frac{x_{BFP}}{\lambda_0 f_B} \; . \tag{4.13}$$

Combining Eq 4.12 and Eq 4.13 yields

$$\frac{x_{BFP}}{f_B} = n\sin(\theta_x) \; . \tag{4.14}$$

For an objective lens, the largest angle θ_{max} that can be collected is described by

$$\frac{x_{max}}{f_B} = n\sin(\theta_{max}) = \mathrm{NA} \; , \tag{4.15}$$

which is the definition of the NA.

4.1.5 Enhancement

It can be seen in Eq 4.8 that in order to enhance the normalised iSCAT signal, the ratio $\frac{|s|}{r}$ of scattered and reflected light must be increased. A range of different approaches to do so is described in this section.

A popular way of enhancing the iSCAT signal is NA-filtering [31, 35, 36], where a partial reflector is centred in the BFP of the imaging objective. The partial reflector is a little disc that only transmits a small fraction of light. As seen in the previous section, the centre of the BFP corresponds to light collected at an angle of zero degrees with respect to the optical axis, which mainly affects the reflected reference beam. Light collected at higher angles, i.e. higher NA, such as the scattered signal from the small object, will be located further way from the centre of the BFP and will hardly be affected. [31, 37]

Another way to selectively reduce the reference signal is to use polarisation filtering. This method can be applied when the scattering object alters the polarisation state of the incident light. Gold nanorods have been reported as a particularly promising example of this method. When illuminating such nanorods with a circularly polarised beam,

their scattered light is mainly linearly polarised. By appropriately setting a circular polariser in the detection path, the reference signal can be controlled to maximise the contrast from the nanorods. [38]

Selectively reducing the reference signal is not the only way to enhance the ratio of scattered and reference light. It is also possible to selectively enhance the amount of scattered light by creating strong optical fields on the substrate surface, e.g. by using thin metal films, where the particles to be detected interact with evanescent tails of the excited plasmons [39, 40].

A combination of both enhancement effects described above, plus a third one, can be obtained with resonant optical gratings [5]:

- The amount of reference light that reaches the camera depends on the spectrum of the grating, which can be controlled by tuning the grating parameters.

- On resonance, the strong fields created on the grating surface lead to an increased number of scattered photons.

- The scattered photons from small particles that strongly overlap with the resonant mode of the grating can couple to the grating modes, which results in increased extraction efficiency at lower angles, lifting the need for oil immersion objectives.

4.1.6 Application: Single Particle Tracking

For the study of transport mechanisms or diffusion properties of systems in the life sciences or in condensed matter physics, single particle tracking is a widely used technique. Trajectories of the particles are obtained from an acquired video by first determining the position in two or three spatial dimensions for each frame. In a second step, the positions are linked between frames in order to obtain the tracks, which can then be analysed, e.g. for determining diffusion coefficients.

A most popular imaging method for single particle tracking is fluorescence microscopy, with its efficient background suppression thanks to the spectral filtering of the excitation light, and its specificity that allows observation of particles in complex environments [41]. Despite its advantages, fluorescence microscopy has fundamental limitations. In cases where the fluorophores suffer from photo-blinking or photo-bleaching [4], the total number of photons that can be detected is limited, i.e. the total observation time is limited as well. Furthermore, since a single fluorescent emitter has a maximal number of

photons that it can emit per unit time, a trade-off must be made between the detected signal intensity and the temporal resolution. A high temporal resolution requires short integration times, which results in weaker signals and therefore higher noise in the determined particle position. A rule of thumb [29, 42] in standard fluorescence microscopy gives an approximate limit for the localisation precision σ at a given frame rate,

$$\sigma = 1 \; \frac{\text{nm}}{\sqrt{\text{Hz}}} \; , \tag{4.16}$$

which means for an acquisition at 1 Hz, the highest achievable localisation precision is ~ 1 nm, and for 100 Hz it would already be ~ 10 nm. For some applications, a much higher resolution in time and space would be desirable. As an example, the diffusion of lipids in a plasma cell membrane is characterised by a diffusion coefficient of $D \approx 1$ um^{2}s^{-1} [43], corresponding to a root mean square displacement of ~ 2 nm per microsecond.

Scattering based techniques, on the other hand, don't suffer from the drawbacks of fluorescence microscopy mentioned above. The total observation time is not limited, as the particles will keep scattering as long as they are illuminated. Furthermore, if a stronger signal is required, the illumination intensity can simply be increased. With a higher signal intensity, the temporal resolution can be increased without loss of localisation precision. The intensity is then limited by the performance of the illumination laser and possibly the damage threshold of the sample under study [44], and the acquisition speed is only limited by the performance of the camera.

However, the sensitivity of most scattering based techniques is limited, e.g. standard dark field microscopy that can only detect gold nanoparticles (AuNP) down to 30 nm in size [45]. For observing weaker scatterers, a higher sensitivity is required. This can be achieved by using an interferometric detection of the scattered light - as is done in iSCAT, with which AuNPs as small as 2 nm can be detected [46]. With its high sensitivity, iSCAT is not limited to AuNPs, but can detect much weaker scatterers. This is well demonstrated by the reports of label-free tracking of single proteins [47].

With iSCAT, it is possible to track particles in three dimensions with a localisation precision of a few nanometres and temporal resolution up to a microsecond, with observation times of up to tens of minutes [48]. These numbers show the superior performance in terms of spatio-temporal resolution compared to fluorescence microscopy.

The advantage of iSCAT being label-free can be a disadvantage when dealing with complex samples, where distinguishing different scatterers is a challenge. In such a case, the specificity of fluorescence microscopy would be extremely useful. Fortunately, it is possible to combine both methods, i.e. to perform simultaneous iSCAT and fluorescence microscopy, harnessing the advantages of both methods [29].

4.1.7 Application: Mass Photometry

As mentioned above, single proteins can be detected with iSCAT in a label-free fashion. The lowest successfully measured protein mass reported so far is as small as 10 kDa [49].

The standard way of detecting proteins with iSCAT consists in observing the attachment of the proteins on the substrate surface, in combination with a particular processing method yielding ratiometric videos [31] (see schematic in Fig 4.4). In short, the ratiometric processing is a running average operation followed by a division of the new average frame by the previous average frame, which effectively corresponds to a background normalisation with a most up-to-date estimate of the background. The resulting ratiometric frames reveal the attachment (and possible detachment) of the proteins within a time window determined by the number of frames to average, which means that previously landed proteins - if they remain statically on the surface - fade out and become part of the background, allowing a clean detection of new arrivals. Note that the averaging also improves the SNR in the shot-noise regime, as previously discussed in section 4.1.3. However, if the number of averaged frames gets too large, other sources of noise begin to dominate, e.g. sample drift or other movements in the background.

As mentioned previously (section 4.1.1), the iSCAT contrast depends on a number of parameters. For a mixture of different proteins, which are suspended in the same medium and whose refractive index, to a good approximation, is the same, the main parameter that determines the contrast is given by the volume. Conveniently, in such a regime, the contrast varies linearly with the particle volume (Eq 4.1 and 4.2), and therefore its mass. This means that a linear calibration can be used to determine the mass of the protein from its iSCAT contrast [50]. This method is called mass photometry.

By comparison, the gold standard method for measuring the mass of proteins is mass spectrometry, which has a precision of the order of 1 Da [51]. This precision is orders
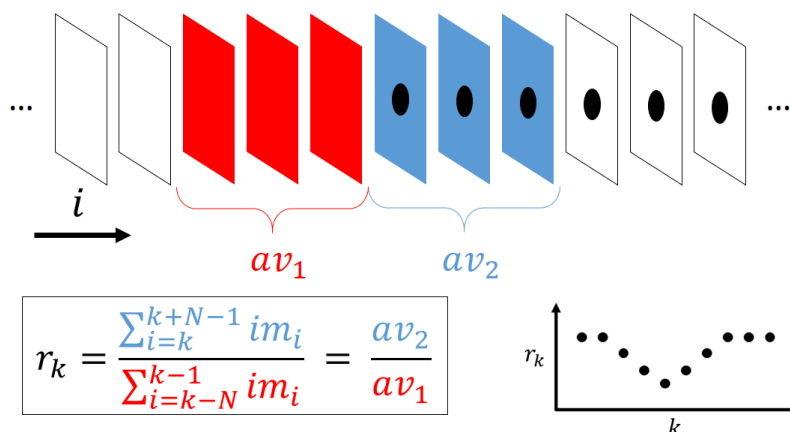
Figure 4.4: Illustration of ratiometric processing with averaging number $N = 3$. The raw video consists a number of images with frame number i. A ratiometric frame r_k is obtained by dividing the average of the following N frames by the average of the previous N frames. As a result, if a particle lands on the substrate at frame number $i = l$, a maximal signal is observed for the ratiometric frame r_l, since all previous frames ($i < l$) only contain the background, and all following frames ($i \geq l$) contain the signal of the landing particle. The signal in r_k ramps up to its maximal value and back to 1, each in N steps.

of magnitude higher than the one obtained by mass photometry (discussed below). However, the high precision of mass spectrometry comes at a price: The proteins must be ionised and be in a gaseous state, which is destructive, requires time and expensive equipment. On the other hand, mass photometry is able to directly measure the mass distribution of a mixture of bioparticles dropped on a coverslip with a pipette, and has a number of advantageous properties:

- label-free

- in solution

- only requiring small sample volumes of ~ 10 ul

- acquire, process and analyse the data within minutes

Mass photometry finds a variety of applications, such as sample characterisation [52], the study of protein oligomerisation [53], biomolecular interactions [54] and macromolecular assemblies [55].

The success of the mass photometry method is reflected in the fact that a spin-off

company has been created at Oxford University in 2018, now called Refeyn, making complete mass photometry kits commercially available. These include a bench top setup and the required software for operation and real-time analysis. With the current product, proteins in the mass range between 30 kDa and 5 MDa can be detected, with an accuracy of at least 5% and a resolution depending on the particle weight, e.g. ± 25 kDa for the measurement of a 66 kDa particle [56] or ± 60 kDa for the measurement of a particle weighing 660 kDa [57].

4.2   Setup Building, Testing and Optimising

I built a complete iSCAT setup from scratch, tested and optimised it with the end goal to study resonantly enhanced microscopy using optical gratings. Here, I present the progression of the setup from the very first version, along with the experiments that allowed me to identify a number of problems and how I solved them.

4.2.1   Camera Frame Rate Test

Before considering the entire setup, let's have a look at a key element: the camera. As described in the introduction, iSCAT can investigate particles at high-speed. In order to do so, it needs a camera with a high frame rate.

I use the Mikrotron EoSens CL (MC1362) camera, as it can achieve extremely high frame rates and has a high sensitivity with its large pixel size (14 um). The camera is connected to a frame grabber from National Instruments (NI PCIe-1433). This frame grabber is an expansion card that plugs directly into the motherboard of the computer, and is able to acquire and write a large amount of data using the camera link (CL) standard. To control the image acquisition, I wrote a custom LabVIEW program[1] and continuously developed it according to the requirements of the experiments. For setting camera parameters via serial commands and the data acquisition itself, the functions of the NI-IMAQ API for LabVIEW are used. I chose a producer/consumer architecture, where user inputs from buttons on the front panel trigger the producer loop to add a given task (e.g. initialise, live view, single frame acquisition or high speed image sequence acquisition) to a queue, which the consumer loop then reads and executes.

During the acquisition of high-speed image sequences, a large amount of data must

---

[1]Thanks to Dr George Duffett for introducing me to LabVIEW and providing me with a starting point for my code.

be handled in a short amount of time. If the control program was not written correctly, the acquisition speed might be slower than the set frame rate. In order to test the custom LabVIEW program, especially to make sure that a set frame rate is indeed reached by the camera, the experiment illustrated in Fig 4.5 is performed: A laser beam shines straight into the camera, without saturating it. In the beam path, a light chopper (EG&G Princeton applied research, Model 197 Light Chopper) is placed. The light chopper is a device that consists of a spinning disc with holes. The laser beam will therefore alternatively be blocked or transmitted, at a frequency f_s that can be set precisely. A video that is acquired in this configuration will show the laser spot appear and disappear, so that the frequency can be measured as described below. The measured frequency f_m will be equal to the true chopper frequency f_s only if the camera acquires at the desired frame rate f_r.
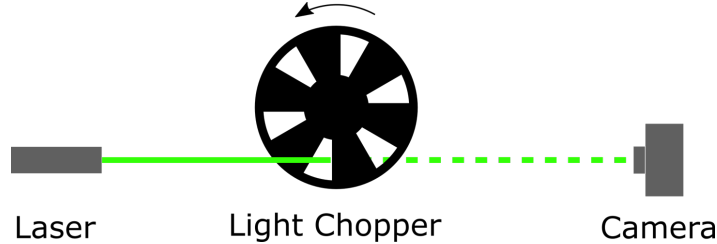
Figure 4.5: Schematic illustration of the experiment to test the frame rate of the camera with a light chopper.

For each frame of an acquired video, the graylevels of all pixels are summed up, which yields a measure of the total intensity I. The frame number i is proportional to the time

$$t_i = \Delta t \cdot i, \tag{4.17}$$

where the time step between two consecutive frames is $\Delta t = 1/f_r$, i.e. the inverse of the camera frame rate.

The frequency of $I(t)$ can be determined by using the fast Fourier-transform (FFT)

$$\hat{I}(f_j) = \sum_{i=0}^{N-1} I(t_i)e^{-i2\pi f_j t_i}, \tag{4.18}$$

defined at frequencies $f_j = \Delta f \cdot j$. The frequency steps are given by

$$\Delta f = \frac{1}{N\Delta t} = \frac{f_r}{N}, \tag{4.19}$$

ROI number	size [pixel]	f_s [Hz]
1	1280 x 1024	15
2	640 x 480	15
3	96 x 96	130

Table 4.1: Table of the defined ROIs with their size and the fixed chopper frequency f_s to be measured. ROI number 1 corresponds to the full frame.

where N is the total number of time steps of I.

The magnitude squared of the transformed signal, $|\hat{I}|^2(f)$, is proportional to the power spectral density (PSD). The stronger the magnitude of a certain frequency, the stronger the response of the PSD. With the signal $I(t)$ oscillating at one single frequency, $|\hat{I}|^2(f)$ is expected to show a distinct peak, corresponding to the measured chopper frequency f_m.

For simplicity, the measured frequency f_m is defined as the frequency f_j for which $|\hat{I}|^2(f_j)$ is maximal, and the measurement uncertainty is $\Delta f_m = \Delta f/2$.

An arbitrary maximal target value for the relative measurement error of f_m is set to $\frac{\Delta f_m}{f_m} \leq 0.01 = 1\%$. With Eq 4.19, it is possible to determine the minimal number of required data points

$$N_{min} = \frac{f_r}{\Delta f} = \frac{f_r}{2\frac{\Delta f_m}{f_m}f_s} = 50\frac{f_r}{f_s} \ , \tag{4.20}$$

assuming a correct measured frequency $f_m = f_s$. The number of frames N acquired for the experiment is obtained by rounding up N_{min}.

The experiment is performed for three different regions of interest (ROI), which have a different size and therefore different maximal acquisition frame rates. For each ROI, an appropriate chopper frequency f_s is set (see table 4.1), and a range of frame rates f_r is chosen, including the highest possible frame rate. Note that in order to successfully measure f_s, the frame rate must be at least

$$f_r > 2f_s \ , \tag{4.21}$$

which is known as the Nyquist-Shannon sampling theorem [58].

An example of the raw images and the integrated intensity I is shown in Fig 4.6 A). Notice how the chopper blocks and unblocks the beam with a small transition time
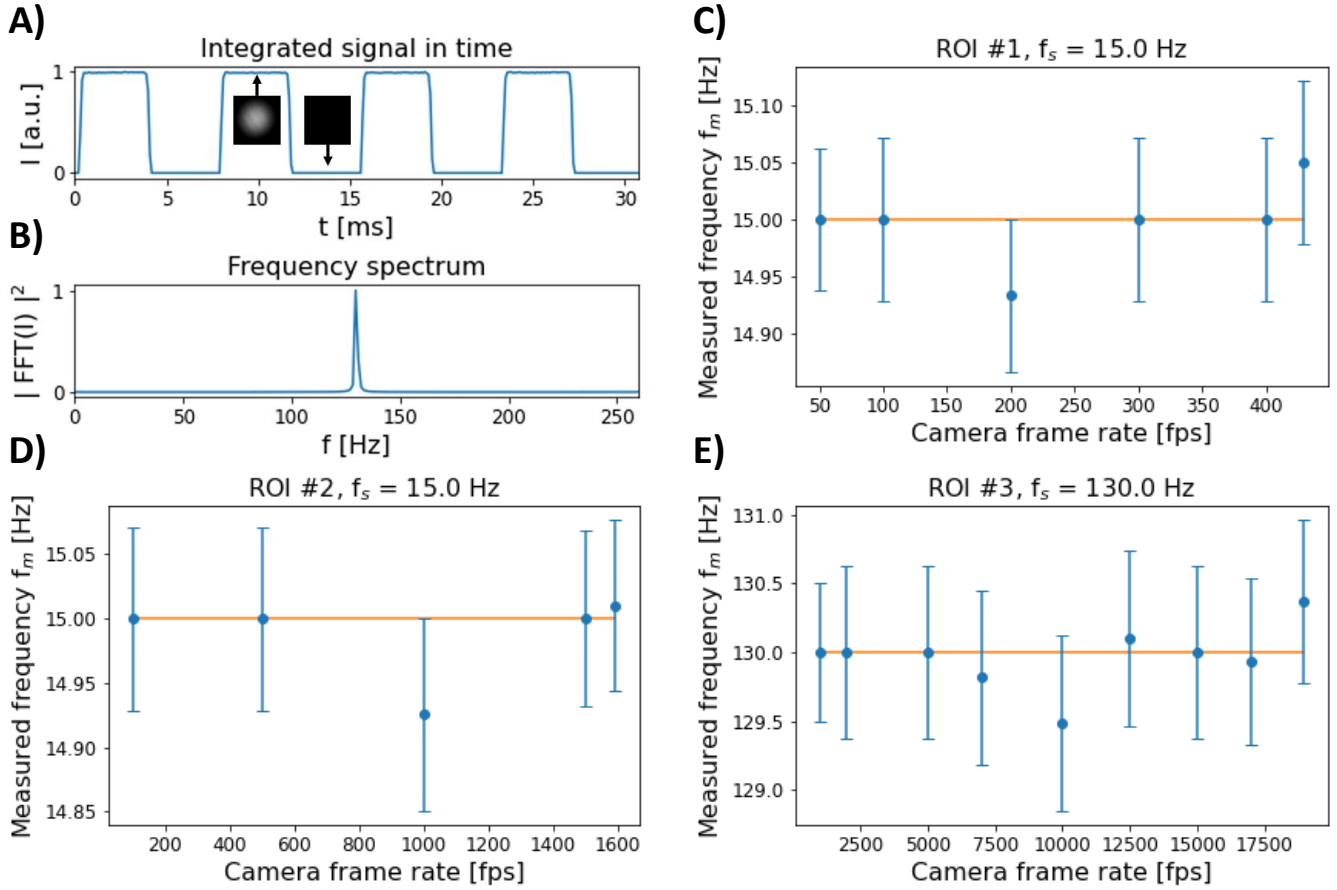
Figure 4.6: Results of the camera frame rate test. A) Example of raw images (insets) and integrated intensity as a function of time, for a chopper frequency of $f_s = 130$ Hz and camera frame rate $f_r = 10\,000$ frames per second (fps). The intensity is normalised to its maximum. B) The absolute squared FFT of the time signal, showing the peak corresponding to the measured frequency f_m. The spectrum is normalised to the peak value. C-E) The measured frequencies for different frame rates (blue) and the true chopper frequency f_s (orange), for the three different ROIs.

of the order of ~ 1 ms, and the beam is blocked during half the cycle period. The corresponding absolute squared FFT of the time signal is shown in Fig 4.6 B). The peak is located at the expected chopper frequency of $f_s = 130$ Hz. For each ROI, the fixed chopper frequency is measured with various frame rates as shown in Fig 4.6 C-E). The true chopper frequency is plotted as an orange line for comparison. In all cases, the chopper frequency is accurately measured within error. The fact that some measured f_m are greater and some are smaller than the true chopper frequency implies that there is no significant bias of the measurement.

This experiment shows that the camera reliably reaches the desired frame rates, even when pushed to the highest speed for a given ROI. Therefore, the camera can now be used in an iSCAT setup with confidence.

4.2.2 First Setup Versions

As described in section 4.1.3, a beam scanning setup has a number of advantages in terms of image quality and noise reduction, but it adds complexity to the setup. Here, a wide field illumination setup is chosen nevertheless, not only for simplicity of the setup, but more importantly because of the intended application - since the goal is to study resonantly enhanced microscopy, where it is important that the grating modes can be excited efficiently. As described in chapter 2, the GMR modes need to excited with collimated light, i.e. not with focussed light. If a grating is illuminated with a focused spot, as is done in the beam scanning setup, a potentially large proportion of the illumination intensity would be lost on angles that don't excite the resonance. In a wide field Köhler illumination setup, practically all the intensity hits the grating at the same angle, i.e. a great angular overlap with a desired mode can be achieved.

A photo of the first version of the iSCAT setup is shown in Fig 4.7 A). The setup consists of two floors. The illumination arm is located on the top floor, a schematic of which is shown in Fig 4.7 B). A fibre-pigtailed laser (Thorlabs LP520-SF15, $\lambda = 520$ nm) is collimated to free space using a fibre collimator (Thorlabs F240FC-B), and the beam is then reflected by two mirrors (M1-2), which are mounted in kinematic mounts (Thorlabs KM100). The beam passes the Köhler aperture (KA) and enters the Köhler lens (KL, f = 20 cm). While the beam is focused by the KL, it reflects at the beam splitter (BS, Thorlabs CM1-BP133), which sends it up vertically, so that the focused spot coincides with the centre of the BFP of the oil immersion objective (Olympus PlanApo N, 60x, NA 1.42), see schematic side view in Fig 4.7 C). This Köhler illumination creates a collimated beam impinging on the sample, which is held in place by a xyz-stage (combination of three Thorlabs PT1A/M), onto which a microscope slide holder (Thorlabs MAX3SLH) is mounted. In order to hold the thin glass coverslip substrate (#1.5, thickness 170 um, Menzel Gläser), which is required when working with high NA oil immersion objectives, a custom 3D-printed coverslip holder has been designed to fit on the microscope slide holder. Reflected and scattered light from the sample is collected by the objective and travels back down through the beam splitter, until it is reflected on a triangular mirror (M3) on the ground floor. From there, the
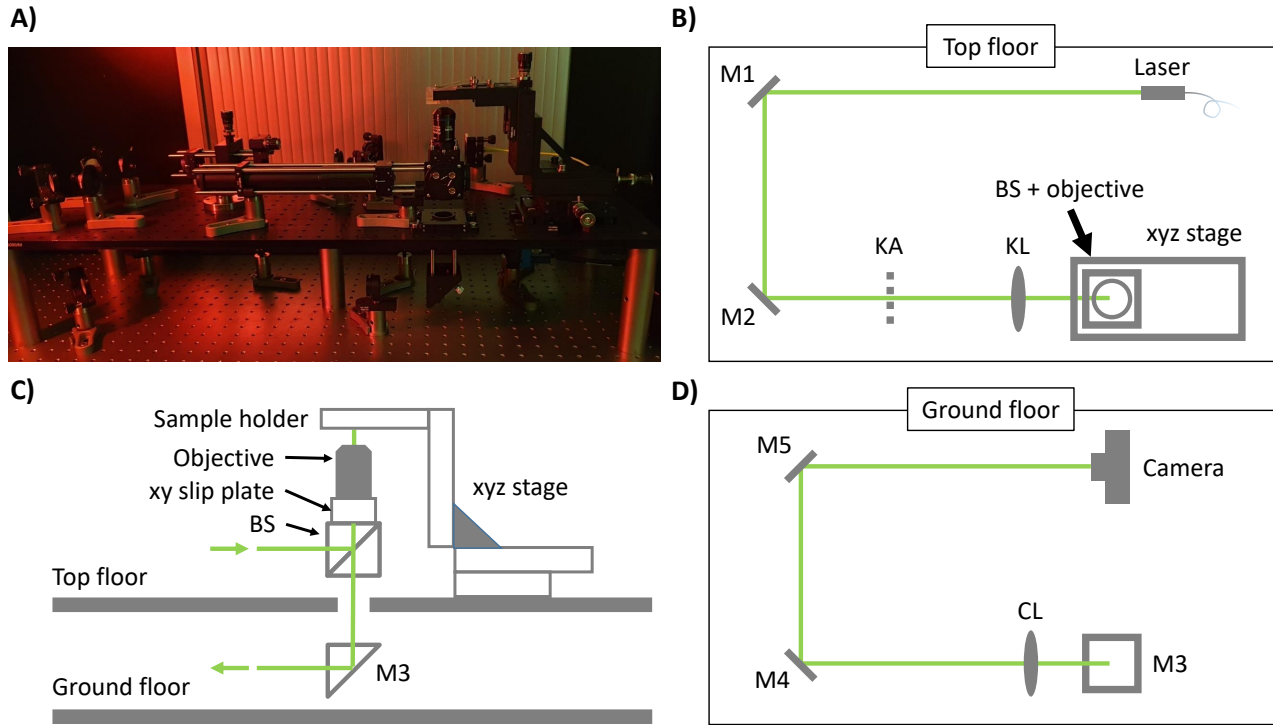
Figure 4.7: First version of the iSCAT setup with a top floor for the illumination arm and a ground floor for the detection arm, connected by the vertical arm containing the objective and sample holder. A) Photo of the setup. B) Schematic of the top floor. M1-2: mirrors, KA: Köhler apperture, KL: Köhler lens, BS: beam splitter. C) Schematic side view of the vertical arm. The xyz-stage is formed by three individual one-dimensional stages. M3: triangular mirror. D) Schematic of the ground floor. CL: camera lens, M4-5: mirrors.

light is focused by a camera lens (CL, f = 1 m) onto the camera sensor via two mirrors (M4-5), see Fig 4.7 D). The distance between the lens and the camera is equal to the focal distance of the lens, in order to focus the "image at infinity" received from the objective.

In order to calculate the resulting magnification, the effective focal distance f_{eff} of the objective is first determined. Olympus objectives are designed for a standard tube lens of $f_{std} = 180$ mm, i.e. the magnification stated by the manufacturer is given by

$$M_{std} = \frac{f_{std}}{f_{eff}} = 60 \ , \tag{4.22}$$

which yields $f_{eff} = 3$ mm. When using a tube lens that has a focal distance f_{CL} different from f_{std}, the obtained magnification is

$$M = \frac{f_{CL}}{f_{eff}} = \frac{f_{CL}}{f_{std}} M_{std} \; . \tag{4.23}$$

With $f_{CL} = 1$ m, a magnification of M $= 333.\bar{3}$ is obtained. Hence, one camera pixel of 14 x 14 (um)^2 size images an area on the sample of approximately 42 x 42 (nm)^2.

With this setup, I was able to acquire first iSCAT images. I note that it can be challenging to find the correct focus, especially with properly cleaned substrates that have no strong scatterers as visual references on their surface. This is where the Köhler aperture comes in handy (Fig 4.7 B). It is placed exactly at focal distance to the Köhler lens, which means that when the aperture is almost closed, the lens produces an image "at infinity" of the aperture edges on the objective side. When this light passes through the objective, it will be focused in the front focal plane of the objective. Therefore, when the reflecting substrate surface is exactly placed in the front focal plane, the edges of the aperture are sharply in focus on the camera; the aperture can then be opened and the setup is in focus. If needed, the focus can be finely adjusted using small scatterers as visual reference, which should now be visible.

Up to this point, the vertical translation stage is used for focusing. However, this stage can not be adjusted sufficiently finely for a reliable focus. Hence, I replaced the initial microscope slide holder by a small, one-dimensional piezo stage (Thorlabs KPZNF15/M), onto which a kinematic mount (Thorlabs KM100) is mounted. I also developed a new design of a 3D-printed sample holder in order to clamp the coverslip to this mount using two standard M3-screws. A photo of the upgraded stage with the piezo controller is shown in Fig 4.8. In the following, this stage configuration will be referred to as the "cantilever stage".

4.2.3 Stage Vibrations

I noticed that when imaging a scattering dirt particle on the substrate with this stage over time, small displacements were apparent in the video. The fact that instabilities could be detected visually means that the vibrations are too strong for a highly sensitive, interferometric microscope.

In order to find the source of this instability, I examined the vibration spectrum of the stage. The corresponding PSD of the vibrations can be obtained by tracking the
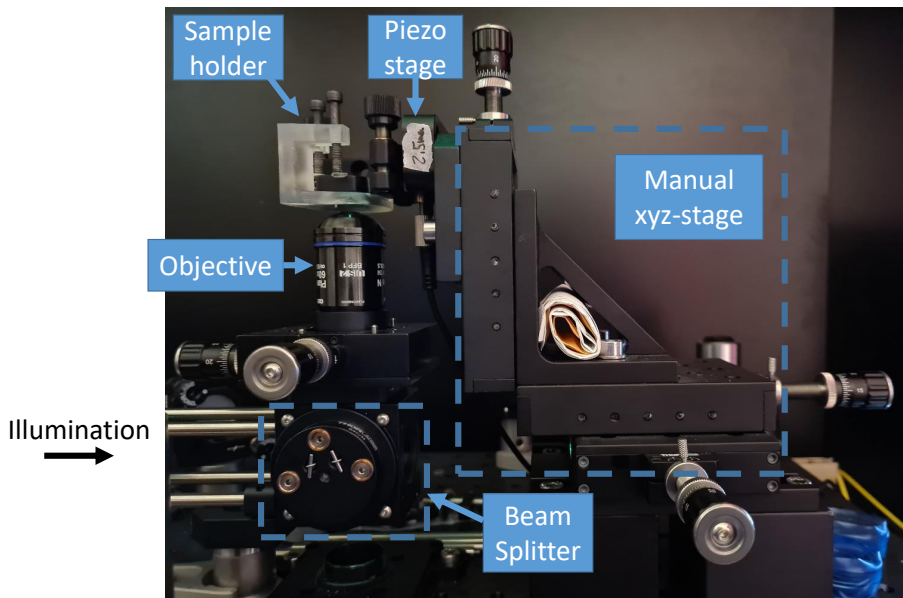
Figure 4.8: Photo of the cantilever stage. Coarse positioning in x,y and z is achieved by the combination of three one-dimensional manual stages. In addition, there is a piezo stage for fine-focusing in z. Coverslips are clamped to the kinematic mount using a 3D-printed sample holder, which also allows the adjustment of the sample angle.

displacement of an immobile scatterer on the substrate over time. For each frame of an acquired video, the central x and y coordinates of the imaged PSF of the scatterer are extracted by means of a two-dimensional Gaussian fit. The PSD is then given by the squared absolute Fourier transform of the displacement (same procedure as in section 4.2.1). With real data of unknown PSD, it can be useful to reduce the noise with the so-called Welch method [59]: The initial signal, i.e. the displacement over time, is cut into several separate sub-signals by a window function, and for each sub-signal the estimated PSD is computed. The final PSD is obtained by averaging the separately measured PSDs. With the Python package SciPy [60], an open source implementation of this method is available, and was used for the processing described here.

Figure 4.9 (top, blue line) shows the displacement of an immobile scatterer along the y-axis of an imaged scattering particle with the cantilever stage setup. A clear, periodic displacement is observed. The corresponding PSD (Fig 4.9, bottom, blue line) shows a distinct peak at 61 Hz. This frequency is not far from the standard mains electricity supply frequency of 50 Hz. In order to find out if this peak is due to mains

noise or indeed due to the suspected mechanical oscillation of the stage, the following test was carried out: Small weights are attached to the stage. Adding weights at the end of an oscillating cantilever decreases its vibrational eigen-frequency. Therefore, if the measured frequency of the peak decreases with more weight, then it is likely due to the cantilever vibrations.
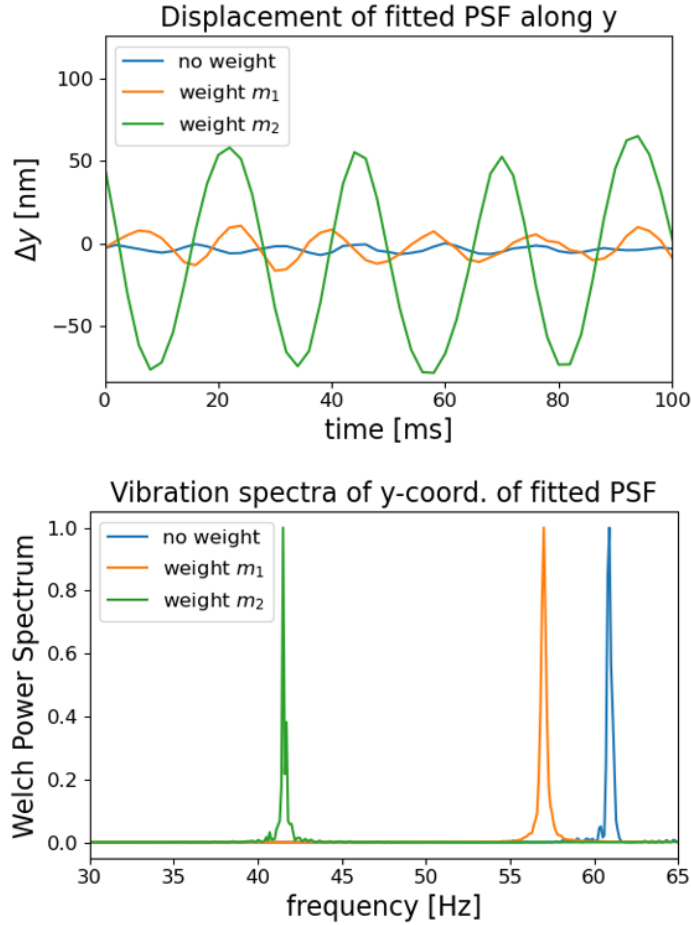
Figure 4.9: (top) Displacement of a scatterer of the along the y-axis, imaged with the cantilever stage and different weights attached to it. (bottom) Corresponding PSD computed using the Welch method, normalised to the maximum value for comparison. $m_1 \approx 23$ g and $m_2 \approx 182$ g.

I added weight by screwing post spacers of 25 mm diameter onto the side of the kinematic mount that holds the coverslip. The first weight m_1 consisted of a 2 mm thick spacer (Thorlabs RS2M), which together with the screw gives a total mass of $m_1 \approx 23$ g. The second weight m_2 consisted of three spacers of thickness 2 mm (Thorlabs RS2M), 6 mm (Thorlabs RS6M) and 10 mm (Thorlabs RS10M), which resulted in $m_2 \approx 182$ g.

The corresponding vibration spectra are shown in Fig 4.9 (bottom). It can be seen that the weights shift the peak to lower frequencies, which confirms that the vibration of the stage arm causes the oscillation.

As the stage has been identified as a major contributor to the mechanical instability, I completely re-designed it. The new stage (see photos in Fig 4.10), inspired by [29] and [61], consist of four solid aluminium posts, each 1.5" in diameter, onto which a custom aluminium plate (1.25 cm thick) is screwed. The plate was made by the team in the mechanical workshop at the University of York. On this cage plate, an xy-stage (Thorlabs CXY2) with a 3D-printed coverslip platform (Fig 4.10 B) is attached with four M6-screws. The objective is screwed into a one-dimensional z-translation stage (Thorlabs SM1ZA), which is attached to the plate from below via four M6-screws and a 3D-printed spacer. The spacer thickness is chosen to be 1 cm, so that the objective focus is roughly at the height of the sample surface. The z-stage is then finely adjusted for best focus.

With the new, improved stage, the vibration spectrum is measured again (Fig 4.10 D). As expected, the peak that was seen in the vibration spectrum of the previous cantilever stage has disappeared.

4.2.4 Confirming iSCAT Images with Fluorescence Microscopy

In order to characterise the setup and its limitations, a range of different, known particles were imaged, starting with stronger scatterers, e.g. big particles, and progressively decreasing the scattering amplitude by changing material or size. Especially with a newly built setup, it is helpful to confirm that any signal detected with iSCAT arises indeed from the expected particle and not from some impurity swimming in the suspension of particles. A popular way of doing so consists of simultaneous iSCAT and fluorescence imaging [29]. To this end, I added a second imaging arm to the ground floor of the iSCAT setup (Fig 4.7 D) via a dichroic mirror, as illustrated in Fig 4.11 A). The green laser at $\lambda = 520$ nm is used as the excitation source for the fluorescent particles. The dichroic mirror is chosen according to its spectrum, so that it transmits the green laser, but reflects the longer wavelengths corresponding to the fluorescence emission. The latter is reflected at another mirror (M6) and focused with a lens (CLF) onto the camera (CS, CoolSnap Myo).
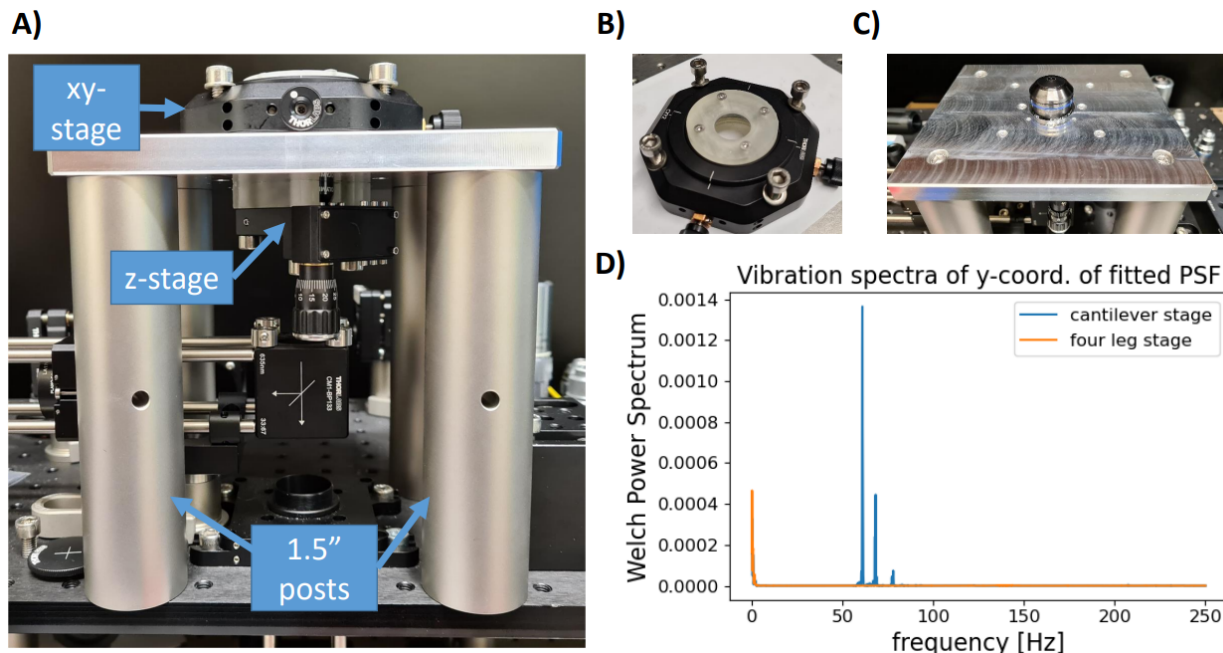
Figure 4.10: A) Side view of the stage consisting of an aluminium plate screwed onto four 1.5" posts for improved stability. The objective is mounted on a z-stage, which is attached to the plate via a 3D-printed spacer. B) Separate photo of the xy-stage with 3D-printed coverslip holder. C) Top of the stage plate without the xy-stage, showing the head of the objective. D) Vibration spectrum of the new four leg stage, with the old cantilever stage spectrum for comparison.

The first particles tested are 1 um sized Nile Red polystyrene beads (Thermo Fisher Scientific, F8819, carboxylate-modified), which have their excitation peak at 535 nm and emission peak at 636 nm. A suitable dichroic mirror for separating excitation and emission wavelengths is the Thorlabs DMSP550R, which is designed for a cut-off wavelength of 550 nm at $45°$ incidence. The fluorescence signal is usually several orders of magnitude weaker than the excitation laser, and the dichroic mirror alone can't suppress the excitation light sufficiently, as it still reflects a few percent of the excitation light. Therefore, a long pass filter (Thorlabs FELH0550), which is guaranteed by the manufacturer to suppress the excitation wavelength of 520 nm by at least five orders of magnitude, is mounted on the camera entrance.

The beads have a coating that consists of a hydrophilic polymer with carboxylic acid moieties. Therefore, in an aqueous solution of pH ~ 7, the surface will be negatively charged. As the glass substrate will be negatively charged as well [62], the beads will experience an electrostatic repulsive force from it. If the beads are suspended in an

electrolyte, the negative charges are partly screened by the ions in the solution, making the beads more likely to stick to the glass surface, which in turn simplifies observing them. In order to obtain a reasonable concentration of $c \approx 3.5 \cdot 10^{10}$ beads/ml in the desired salt solution, the beads are diluted 1:100 in a solution of 10 mM NaCl (aq). For imaging the beads, a small volume of 10 ul of the resulting suspension is dropped onto the glass coverslip with a pipette.

An example image of a 1 um bead with the setup configuration in Fig 4.11 A) is shown in Fig 4.11 B). The bead doesn't appear circular and cannot be focused properly, which means that the point spread function (PSF) is far from the ideal Airy pattern. Nevertheless, it is possible to image the suspended beads simultaneously with iSCAT and fluorescence microscopy, as shown in Fig 4.11 C) and D), respectively. Three beads are stuck on the surface, see the blue arrows. Three swimming beads, slightly out-of-focus, are easily spotted in the fluorescence image. They are not easily recognised in the static iSCAT image, but are better identifiable when playing back consecutive frames of the video. A few seconds later, the swimming beads have diffused away, and one bead has landed on the surface, see Fig 4.11 E-F).

While the fluorescence images presented so far can confirm the iSCAT images with the sparsely suspended, big and bright beads, their non-ideal PSF is unacceptable for moving onto more complex samples. This is why the cause of the observed PSF must be found and corrected.

As a first test, the dichroic mirror was removed and the long pass filter was mounted on the camera that is usually used for imaging the iSCAT signal. The beads were imaged as clear, round circles. This led to suspecting the dichroic mirror as the source of the incorrect PSF. As a second test, the long pass filter is mounted back on the fluorescence camera, as in the initial setup (Fig 4.11 A), but the dichroic mirror is replaced by a regular mirror. This resulted again in a correct, circular PSF. In the following, it was made sure that the dichroic mirror was not by chance placed in the wrong orientation. However, placing the flipped dichroic mirror back into its place did not fix the PSF either. As the undesired PSF (Fig 4.11 B) shows selective horizontal and vertical blurring, but no diagonal blurring, i.e. it is aligned with the rotation axis of the dichroic mirror, I carried out a final test: The dichroic mirror was rotated so that the incidence angle is $\alpha = 3°$, i.e. almost normal incidence, as illustrated in Fig 4.11 G). This does indeed fix the PSF, the beads appear circular and can be focused satisfyingly, as shown in Fig 4.11 H).
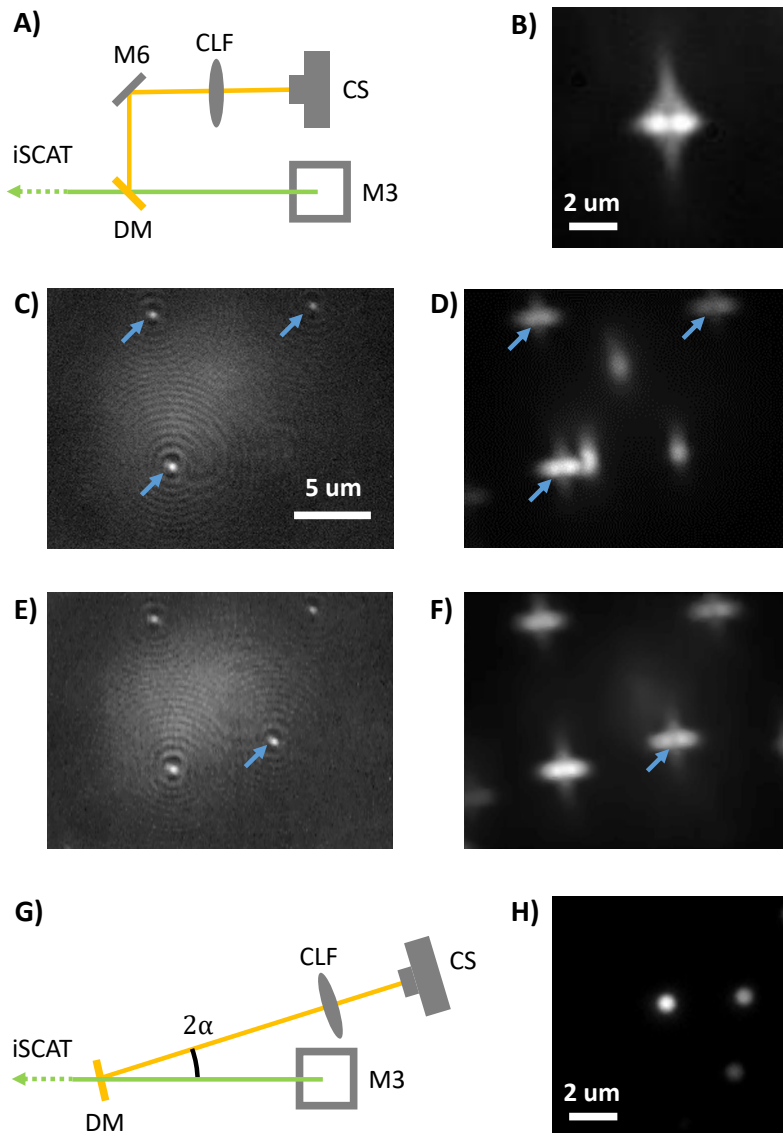
Figure 4.11: Fluorescence imaging arm added to the setup for simultaneous iSCAT and fluorescence microscopy of 1 um Nile Red polystyrene beads. A) Schematic of the fluorescence imaging arm with dichroic mirror (DM) at $45\,^\circ$. B) Fluorescence image of a bead, with cross-shaped PSF. Integration time 10 ms. C) iSCAT image of beads in suspension. Integration time 50 ms. Three beads are stuck on the surface (see arrows). D) Corresponding simultaneous fluorescence image. The three beads can be identified (see arrows), as well as three moving beads in the centre. E-F) The same FoV a few seconds later, again imaged with iSCAT and fluorescence, respectively. Another bead has landed (see arrow). G) Schematic of the setup with the dichroic mirror at $\alpha = 3\,^\circ$ incidence. H) Fluorescence image of beads using configuration G), with an improved PSF.
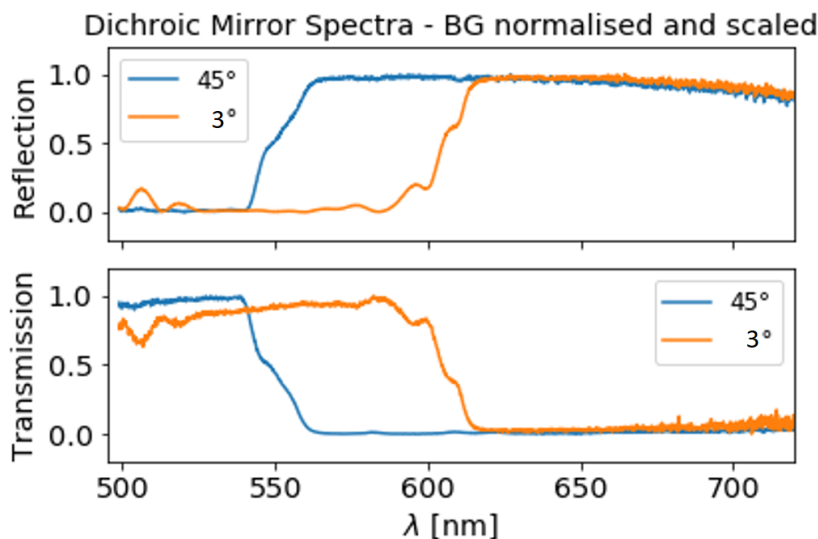
Figure 4.12: Reflection (top) and transmission (bottom) spectrum of the dichroic mirror (Thorlabs DMSP550R) at two different incident angles α (legend).

Although changing the angle of the dichroic mirror has fixed the PSF, attention must be paid to the effect that this has on its spectrum. The mirror was designed for $45\,^\circ$ incidence, but a change in the incidence angle shifts the cut-off wavelength λ_c. In order to characterise this shift, the reflection and transmission spectra of the dichroic mirror are measured for both $\alpha = 45\,^\circ$ and $\alpha = 3\,^\circ$, using a simple setup consisting of a torch and a spectrometer (Thorlabs CCS175/M). Before inserting the dichroic mirror between the torch and the spectrometer, a spectrum of the torch alone was acquired, which I used to normalise the dichroic mirror spectra. I then scale the normalised spectra to the range of [0,1] for visualising the shift of λ_c, see Fig 4.12. As specified by the manufacturer, $\lambda_c = 550$ nm at $\alpha = 45°$ incidence. For $\alpha = 3°$ incidence, $\lambda_c \approx 600$ nm, i.e. it is red-shifted by ~ 50 nm. When imaging Nile Red beads, with their excitation maximum at $\lambda = 637$ nm, a cut-off wavelength of 600 nm is acceptable, however for different fluorophores with maximum emission at lower wavelengths, the 50 nm red shift could reduce the detected signal significantly. In such a case, one could consider a different dichroic mirror, designed for a lower λ_c, anticipating the red shift of approximately 50 nm.

4.2.5 Towards Smaller Particles

Having benchmarked the setup on images of the relatively big 1 um beads in the previous section, it is now interesting to reduce the particle size in order to more fully assess the performance of the setup.

The next particles to be imaged are gold nanoparticles (AuNP)(Sigma-Aldrich 742023-25ML stabilised in citrate buffer), which are 80 nm in size. This is a generous reduction in particle size, more than one order of magnitude. However, as seen in section 4.1.1, for small particles the scattering amplitude of gold is almost an order of magnitude stronger than for polystyrene, which justifies the strong decrease in particle size.

Since the particle size is now significantly smaller than the wavelength, its image is not expected to show any geometrical features of the particle, but merely the diffraction limited PSF (discussed in section 4.1.2). As described by the Stokes-Einstein relation [63], reducing the particle size also results in a higher diffusion coefficient. Both the reduced length scale of the imaged signal and the increased speed, with which the particles move, increase the risk of motion blur. To avoid this, the particles can be immobilised on the substrate surface by functionalising it. This can be done with Poly-L-lysine (Sigma-Aldrich P8920), which creates a positively charged substrate surface, which attracts and immobilises AuNPs with their negatively charged citrate surface.

In order to observe single 80 nm AuNPs, a relatively sparse suspension containing only $7.8 \cdot 10^8$ AuNP/ml was prepared by diluting the stock suspension with a ratio of 1:10 in DI water. A volume of 10 ul of the diluted suspension was dropped onto the Poly-L-lysine functionalised glass coverslip substrate. Example images of the AuNPs are shown in Fig 4.13. Before the AuNP meets the substrate surface it diffuses in the bulk liquid out-of-focus (Fig 4.13 A). The corresponding PSF is characterised by a relatively wide central spot with a large number of visible rings around it. After the AuNP lands and sticks to the surface (Fig 4.13 B), it is in focus and its PSF has a bright, narrow peak in the centre. A profile along the x-axis of the PSF is shown in (Fig 4.13 C). The asymmetry close to the centre may be explained by the illumination beam being slightly misaligned.

Since the 80 nm AuNPs are easily visible even in the raw iSCAT images, a smaller size of 20 nm was tested, in order to get closer to the limit of the setup. The 20 nm
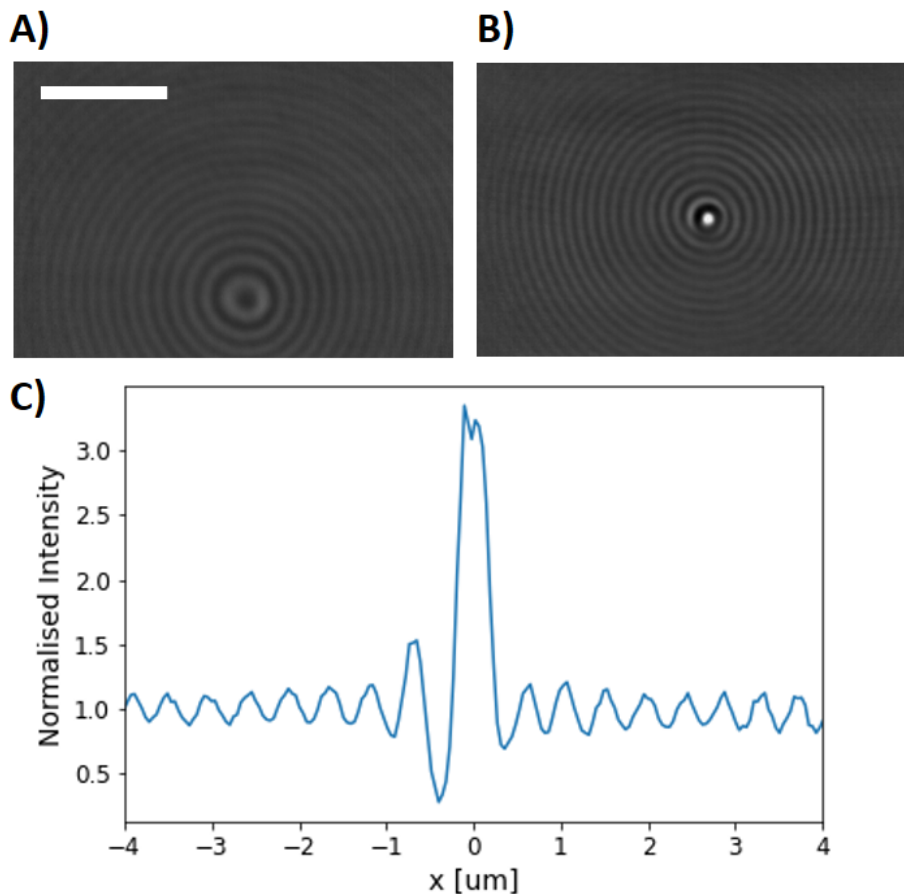
Figure 4.13: Background normalised iSCAT images of an 80 nm AuNP in suspension. Exposure time 1 ms. Scale bar 5 um. A) AuNP undergoing Brownian motion slightly out of focus. B) AuNP sticking to the substrate surface, thanks to the Poly-L-lysine surface functionalisation. C) Corresponding profile plot along the x-axis, through the centre of the PSF.

AuNPs (Sigma-Aldrich 741965-25ML) are diluted 1:10 in DI water in order to obtain a relatively high concentration of $\sim 6.5 \cdot 10^{10}$ AuNP/ml. To reduce noise from the moving liquid-air interface at the top of the drop, a polydimethylsiloxane (PDMS) well is used. A well is obtained by creating a ~ 2 mm thick PDMS layer, cutting it into squares with a scalpel and punching a 3 mm diameter hole in it with a biopsy punch (Instapac Skin Biopsy Punch). A 10 ul drop of the AuNP suspension is then placed inside the well with a pipette.

Fig 4.14 A) shows a raw iSCAT image of the 20 nm AuNPs. The contrast is too weak for a clear observation of the 20 nm AuNP in the raw images. However, the

A)

B)

C)

D)
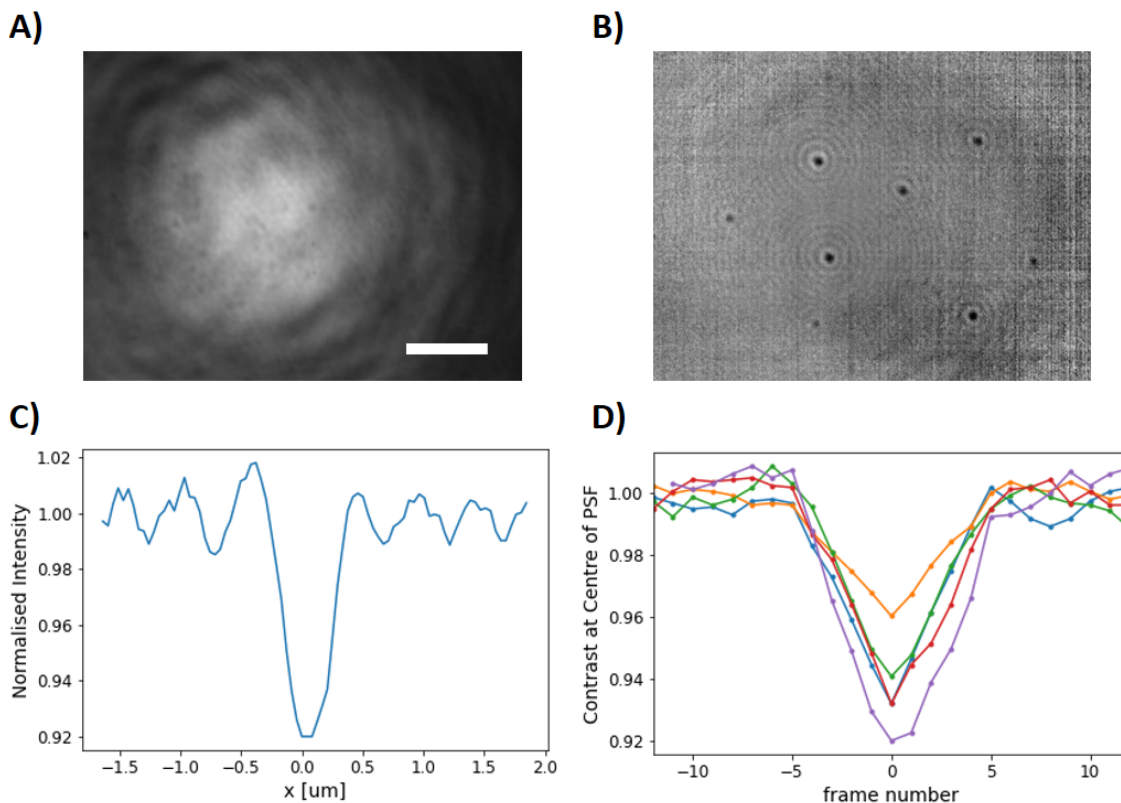
Figure 4.14: iSCAT images of 20 nm AuNP. A) Raw images, acquired with an exposure time of 3 ms at 10 fps. Scale bar 5 um. B) Ratiometric frame revealing the landing AuNPs, with number of averaged frames $N = 5$. C) Profile plot along the x-axis of one PSF. D) Contrast in the centre of the PSF for a number of frames with respect to the landing frame, example shown for five different AuNPs.

surface attachment of the AuNPs can be made visible by ratiometric image processing (described in section 4.1.7). An example of a ratiometric frame is shown in Fig 4.14 B).

A number of PSFs can be seen, all with a dark centre (see profile in Fig 4.14 C), unlike the PSF of the 80 nm AuNP shown before (Fig 4.13). In fact, a small z-translation of the objective focus can flip the sign of the central peak, as discussed in detail in [30]. Here, the best appearing contrast of the 20 nm AuNP was obtained for the PSF with a dark centre. Some of the PSFs in the ratiometric frame show higher contrast than others. This is not necessarily due to a difference in the scattered intensity, but PSFs appearing weaker in this frame might have landed a few frames before (after) the current frame, i.e. the contrast might be already ramping down (still ramping up). This characteristic appearance and disappearance of the PSF is illustrated by plotting

the contrast value of the central peak of the PSF versus the frame number. The five examples in Fig 4.14 D) show how the contrast increases and then decreases, each in five frame steps, which corresponds to the number N of frames to average for the ratiometric processing. More than N frame steps away from particle attachment, the ratiometric contrast should be equal to 1. The contrast variations of ~ 0.01 around the expected value are due to noise. Noise can arise from extended rings of other particles that land close to each other in time and space. Two other types of noise are directly visible in the ratiometric frame. We note that horizontal and vertical lines are present, which are commonly observed in CMOS cameras [64]. On the other hand, big areas appear darker than their surroundings and stretch out over ~ 10 um, e.g. in the top right or bottom right corner. These areas alternate from bright to dark with increasing frame number and are likely due to reflections from the moving interface between the liquid-air interface of the drop, or due to setup instabilities.

The 20 nm AuNP are the smallest particles that I have been able to image successfully in this work. Weaker scatterers, namely 20 nm polystyrene beads, have also been tested. The expected signal with polystyrene is almost one order of magnitude smaller (see section 4.1.1) than the ~ 0.06 obtained with the 20 nm AuNP, and assuming the same noise level of ~ 0.01, the SNR would be $\sim \frac{0.005}{0.01} = 0.5$, which is very low. In light of these considerations, it is no surprise that the 20 nm polystyrene beads have not been detected successfully.

4.3 NA-filtering with Partial Reflectors

4.3.1 PR as Beam Splitter

As mentioned in section 4.1.5, the iSCAT signal can be enhanced by placing a partial reflector (PR) in the BFP of the objective. This way, the reference beam is attenuated, whereas the scattered light is hardly affected. It is worth noting that the objective used here has its BFP located within the objective, i.e. it cannot be accessed directly.

Even if the PR is not placed exactly in the BFP, but close enough to it, NA filtering is possible [31]. A relatively simple implementation, requiring only a minor change in the standard setup (Fig 4.1), consists in replacing the beam splitter by the PR, while making sure that the distance between the objective and the PR is kept small. A schematic of the setup with a PR as the beam splitter is shown in figure 4.15.
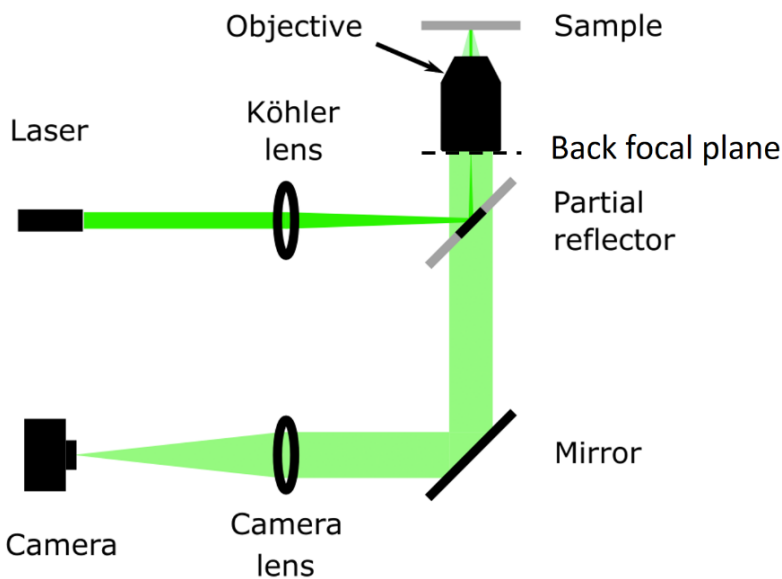
Figure 4.15: Schematic of a simple iSCAT setup with NA filtering, where the beam splitter is replaced by a partial reflector.

A first PR disc was fabricated by depositing 80 nm of silver on a glass microscope slide (schematic in Fig 4.16 A) by magnetron sputtering, using a mask consisting of an aluminium plate with a drilled hole of 2 mm diameter. As shown in Fig 4.16 B), the PR is mounted with a filter holder (Thorlabs FFM1) onto a kinematic platform (Thorlabs B4C/M), which can be inserted into a cage cube (Thorlabs C6W), replacing the previously used beam splitter cage cube. During the alignment of this PR, it became
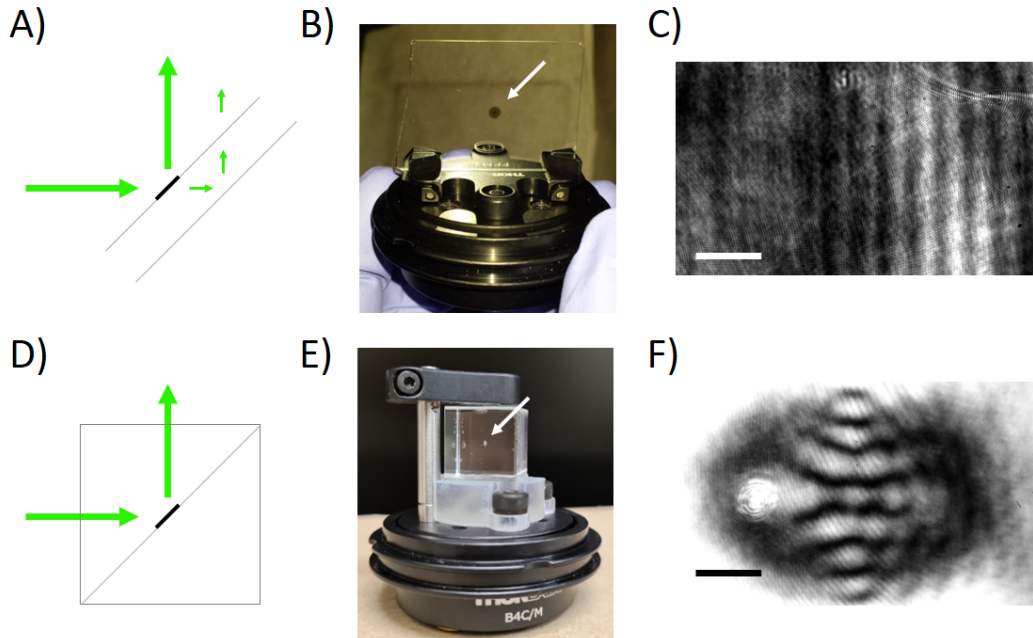
Figure 4.16: Partial reflectors used as beam splitters in the iSCAT setup. A) Schematic of a PR on a microscope slide. B) Corresponding photo of the PR mounted on its platform. The arrow points to the silver disk. C) Corresponding iSCAT background image. D-F) Schematic, photo and background image with the partial reflector cube, consisting of two glued prisms. Scale bars 5 um.

apparent that a silver disc diameter of 2 mm is bigger than necessary, which is why for the following PRs, the size has been reduced, in order to affect the scattered light as little as possible.

The iSCAT images obtained with this PR show vertical fringes in the background, especially when the PR is slightly misaligned (Fig 4.16 C). This can be explained as follows: Light that is either transmitted by the silver disc or passes next to it can be reflected on the bottom glass interface (represented by small arrows in Fig 4.16 A). As a result, two points are created in the BFP. The desired first spot corresponds to light reflected by the PR disc and is located in the centre of the BFP, which produces the collimated illumination beam at normal incidence. The second spot in the BFP, corresponding to the light reflected at the bottom glass-air interface of the PR substrate, is off-centred by a distance of $\tilde{d} = 0.76$ mm, which can be calculated using Snell's law and trigonometry (see Appendix B). This second spot in the BFP produces another

collimated illumination beam at an angle, with corresponding spatial frequency of

$$\nu_x = \frac{\tilde{d}}{\lambda f_{eff}} = 0.48 \text{ um}^{-1} , \tag{4.24}$$

where $\lambda = 520$ nm is the wavelength and $f_{eff} = 3$ mm is the focal distance of the objective (see section 4.2.2). This corresponds to a fringe spacing of

$$\Lambda_x = \frac{1}{\nu_x} = 2.1 \text{ um}, \tag{4.25}$$

which agrees well with Fig 4.16 B), where the scale bar of 5 um approximately covers 2.5 fringes.
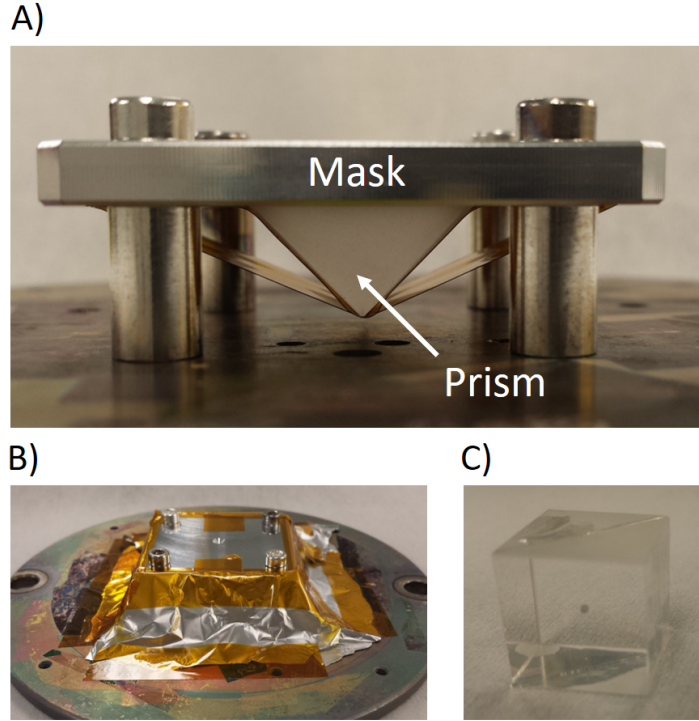
Figure 4.17: Fabrication of the PR cube. A) Close-up photo of the prism taped to the aluminium mask from below. The mask has a central 1 mm diameter hole and a rectangular area milled out, which holds the prism in place. The mask is mounted on the sputtering stage using four screws and spacers. B) Photo of the mounted mask with prism after taping the aluminium curtain around the mask, which prevents the deposition of metal under the mask from the sides. C) Final PR cube, with the second prism glued onto the first one. All side lengths of the cube are 15 mm.

In order to remove the parallel glass-air interface at the bottom of the substrate, which creates the unwanted fringes, an alternative PR design is proposed: The PR cube (schematic Fig 4.16 D). To fabricate it, a silver disc is first sputtered onto the diagonal face of a triangular prism (Thorlabs PS915). Due to its triangular shape, a more elaborate design of the sputterer mask is required, as shown in Fig 4.17. Once the disk is sputtered, a second prism is glued on the first one, with index matching glue (Norland Optical Adhesive 61). The result is a cube (Fig 4.17 C), whose only diagonal optical interface is the one containing the silver disc. A photo of the PR cube on the cage cube platform and corresponding iSCAT background image obtained with it are shown in Fig 4.16 E) and F), respectively. It is seen that the regularly spaced, vertical fringes are not present any more, as expected. However, another inhomogeneous background is observed, which is likely due to diffraction by the silver disc. It might be possible to optimise the PR disc dimensions for a more homogeneous background. Due to the resources that an iterative optimisation would require, and the fact that a PR as beam splitter adds considerable complexity to the setup alignment, I decided instead to use a regular beam splitter and to implement a different approach of NA filtering, as described in the next section.

4.3.2   Setup for Imaging the BFP

Instead of placing a PR only in the vicinity of the BFP, NA filtering can be performed by accessing the exact BFP of the objective by imaging it with additional lenses in the imaging path [31].

One advantage of this implementation is the ability to keep the iSCAT illumination arm and the focused field of view the same and in focus while inserting or removing PRs, which allows a direct comparison of regular iSCAT and NA-filtered iSCAT.

The chosen implementation for forming the image of the BFP in free space is illustrated in Fig 4.18 A). It builds on the fact that each lens produces in its BFP the Fourier transform of the intensity distribution in its FFP and the other way around (see section 4.1.4).

The first Fourier transform is performed by the objective, which takes light from the sample plane P_1 and produces the transform in its BFP (plane P_2). A first lens (L1) is placed at its focal distance f_1 from the plane P_2. At a distance f_1 behind L1 (plane P_3), the Fourier transform of P_2 is obtained, which simply corresponds to the image of the sample magnified by $M_1 = \frac{f_1}{f_{eff}}$, where f_{eff} is the effective focal distance
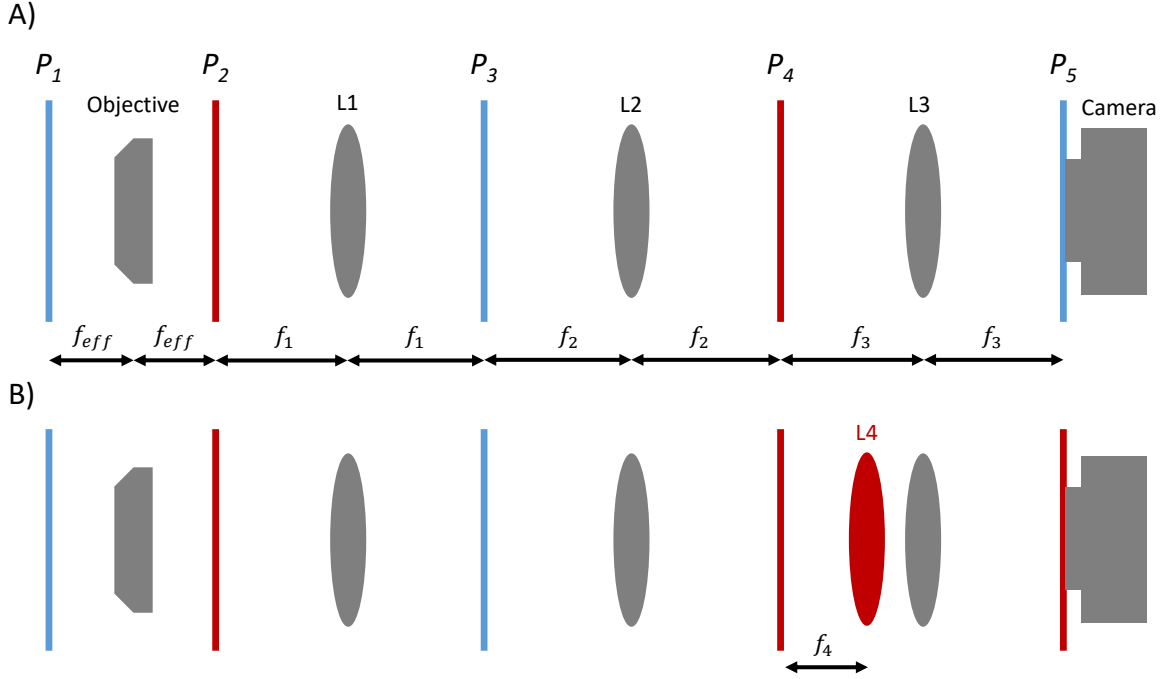
Figure 4.18: Schematic of the imaging arm in the setup used for accessing the BFP of the objective by forming an image of it in free space with three lenses (L1-3). Planes P_i correspond to planes where the image of the sample is in focus (blue) or where the BFP is in focus (red). A) Setup as to be used for iSCAT imaging. A PR can be placed in the plane P_4 for NA filtering. B) A lens L4 can be flipped into the imaging path in order to focus the BFP on the camera.

of the objective (see section 4.2.2).

The same principle is continued with a second lens (L2), which creates an image of the objective BFP in the plane P_4, with magnification $M_{BFP-1} = \frac{f_2}{f_1}$. It is in this plane in free space, where the PR can be placed for NA filtering. In order to obtain the final iSCAT image of the sample, a third lens (L3) is placed between P_4 and the camera sensor (P_5), again at distance f_3. Note that L2 and L3 create an image of P_3 with a magnification of $M_2 = \frac{f_3}{f_2}$.

The final magnification of the image is given by

$$M_{tot} = M_1 M_2 = \frac{f_1 f_3}{f_{eff} f_2} \ . \tag{4.26}$$

For the choice of the focal distances of the lenses, three factors are taken into account:

- For consistency, keep the imaging path length the same as with the previous one-camera-lens setup. The previous camera lens with $f_{CL} = 1$ m was at a distance of ~ 50 cm from the objective BFP, resulting in a path of $l \approx 150$ cm. The new path length is given by $l = 2 \sum_{i=1}^{3} f_i$.

- Keep the total magnification the same as well, i.e. $M_{tot} = 333.\bar{3}$.

- Make sure none of the planes P_3 and P_4 coincide with the surface of any other optics, such as the mirrors M4 and M5 (from Fig 4.7 D), or the dichroic mirror if in use. The first reason being that P_4 must remain accessible for NA filtering. Secondly, if the plane P_3 coincides with the surface of an optical element, any scattering dust particle or scratch will be directly imaged onto the camera, unnecessarily deteriorating the iSCAT image quality.

The chosen focal distances satisfying these criteria, are $f_1 = 40$ cm, $f_2 = 10$ cm and $f_3 = 25$ cm.

For making sure that a PR is well aligned in the BFP, it is useful to be able to image the BFP on the camera. This can be achieved by using a fourth lens L4 at its focal distance f_4 away from P_4, as shown in Fig 4.18 B). If L4 is flipped in, it puts the image of the BFP in $P4$ to infinity, which is focused on the camera sensor by L3, with a magnification of $M_{BFP-2} = \frac{f_3}{f_4}$. The original BFP of the objective is therefore imaged with a total magnification of

$$M_{BFP} = M_{BFP-1} M_{BFP-2} = \frac{f_2 f_3}{f_1 f_4} = 0.8\bar{3} , \qquad (4.27)$$

where the focal distance $f_4 = 7.5$ cm is chosen according to the space that is available between P_4 and L3.

4.3.3 Testing the BFP Images: NA and TIR

In order to make sure that the BFP is correctly imaged, I conceived the following experiment: The angular reflection spectrum of a glass-air or glass-water interface is measured and used to determine the radius of the NA-circle of the objective and the critical angles θ_c for total internal reflection (TIR) in the corresponding medium.

A beam of light that propagates in the substrate and hits the glass-medium interface at an angle θ_g will be refracted, i.e. transmitted at a different angle θ_m, according to

Snell's law

$$n_g \sin(\theta_g) = n_m \sin(\theta_m) \,, \tag{4.28}$$

where n_g and n_m are the refractive indices of glass and the medium, respectively. In cases where the medium has a lower index than the glass, i.e. $n_m < n_g$, the beam will propagate at a higher angle in the medium. The upper limit of the angle in the medium is $\theta_m = 90°$, which corresponds to propagation parallel to the interface. The corresponding angle in glass is known as the critical angle

$$\theta_c = \arcsin\left(\frac{n_m}{n_g}\right) \,. \tag{4.29}$$

This means that any angle $\theta_g > \theta_c$ incident from the glass side has no corresponding beam that can propagate on the medium side, and is therefore completely reflected, which is known as TIR (see section 2.4).
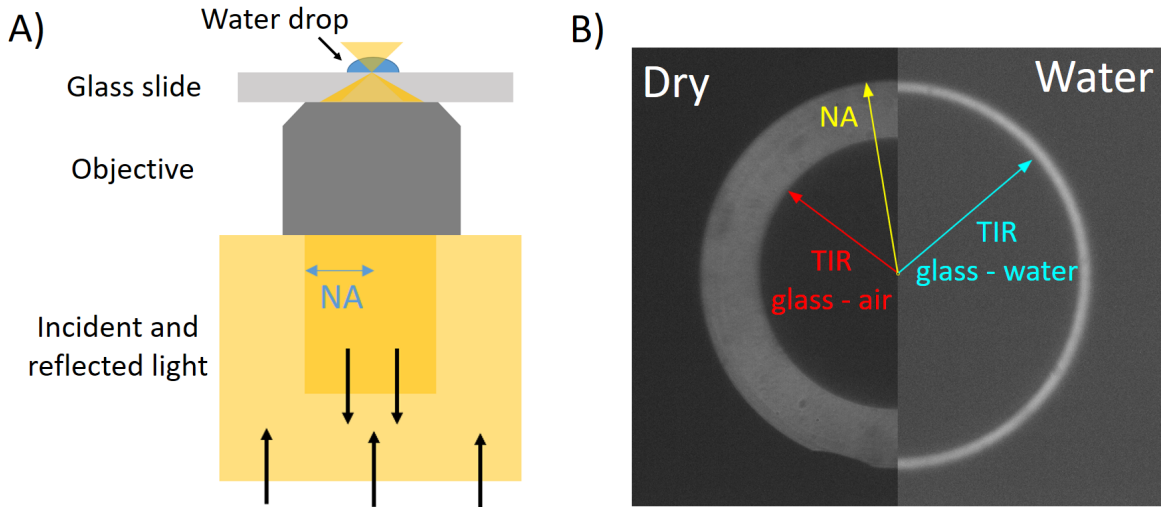
Figure 4.19: A) Schematic of the objective with a wide beam overfilling the back aperture. The beam is focused on the surface of the glass slide and reflects back down. The reflected beam width is limited by the NA of the objective. B) Images of the BFP with air (left) or water (right) as medium. In order to illustrate the fact that the radius of the NA-circle doesn't depend on the medium, the two images were cut in half and combined to one single montage.

The angular reflection spectrum is measured as follows: A wide, roughly collimated beam from a Halogen light source (Thorlabs SLS202L) is used to overfill the back aperture of the objective, as illustrated in Fig 4.19 A). This creates a focused spot on the glass surface, i.e. the glass-medium interface is illuminated with all possible angles

that the objective allows, where the maximal angle is determined by the NA equation (Eq 4.15). The reflected light is collected by the objective and travels down to the imaging system (described above in Fig 4.18).

The resulting images with air or water as medium are shown in Fig 4.19 B). For both media, a ring is observed in the BFP, where the outer radius corresponds to the NA of the objective, and doesn't depend on the medium. The inner radius corresponds to θ_c, and changes considerably when depositing a drop of water on the dry glass slide - as expected. Thus, the bright ring corresponds to light that undergoes TIR.

As seen in section 4.1.4, an angle θ in the front focal plane of the objective relates to a radius r_{BFP} in the BFP as

$$\theta = \arcsin(\frac{r_{BFP}}{n_g f_{eff}}) \ . \tag{4.30}$$

The radii r_{px} in units of pixel are extracted from Fig 4.19 B) by opening the raw images in the ImageJ software [65] and visually determining the best matching circular overlay, from which the radius can be read directly. The uncertainty of such a radius measurement is estimated to be 1 %. The resulting radii can then be converted to their corresponding distance in the objective BFP using the relation

$$r_{BFP} = r_{px}\frac{s_{px}}{M_{BFP}} \ , \tag{4.31}$$

where $s_{px} = 14$ um is the pixel size of the camera and $M_{BFP} = 0.8\bar{3}$ the magnification of the imaged BFP. Each r_{BFP} is plugged into Eq 4.30 in order to obtain the corresponding angle θ, the results are reported in table 4.2. These angles can be compared to the values θ_{th} expected from theory, which are computed using Eq 4.15 and NA=1.42 for the NA circle, and Eq 4.29 for the critical TIR angles, with the refractive indices of glass $n_g = 1.51$, air $n_{air} = 1$ and water $n_{water} = 1.333$.

Measured Quantity	r_{BFP} [mm]	Measured θ [°]	θ_{th} [°]
NA circle	4.29 ± 0.04	69.2 ± 1.5	70.1
TIR glass-air	2.97 ± 0.03	41.2 ± 0.5	41.5
TIR glass-water	4.03 ± 0.04	62.9 ± 1.1	62.0

Table 4.2: Table of the radii extracted from Fig 4.19 B), with corresponding angles θ and expected angles θ_{th} from theory.

Note that all three measured angles contain the expected value within their measurement uncertainties, which confirms that the BFP is correctly imaged, which was the goal of this experiment. In the next section, the BFP will be manipulated in order to enhance the iSCAT contrast.

4.3.4 External Partial Reflector

Having confirmed that the BFP is measured correctly when the lens L4 is flipped into the beam path, a PR can now be easily aligned in the intermediate image plane of the BFP (plane P_4 in Fig 4.18). In order to see the PR in the BFP, an illumination other than the iSCAT illumination laser is useful, as the latter is focused to a small spot by the Köhler lens. In order to obtain an additional, wider beam in the BFP, and therefore see a brightfield-type of contrast from the PR, a slightly un-collimated beam is added to the illumination path of the iSCAT laser by means of a dichroic mirror (Thorlabs DMSP550). The focused laser spot and the bigger spot from a halogen lamp in the imaged BFP are shown in Fig 4.20 A). The PR is placed close to the imaged BFP into the imaging path and moved along the optical axis until in focus (Fig 4.20 B). Then, it is laterally translated for best overlap with the iSCAT illumination beam, as shown in Fig 4.20 C).
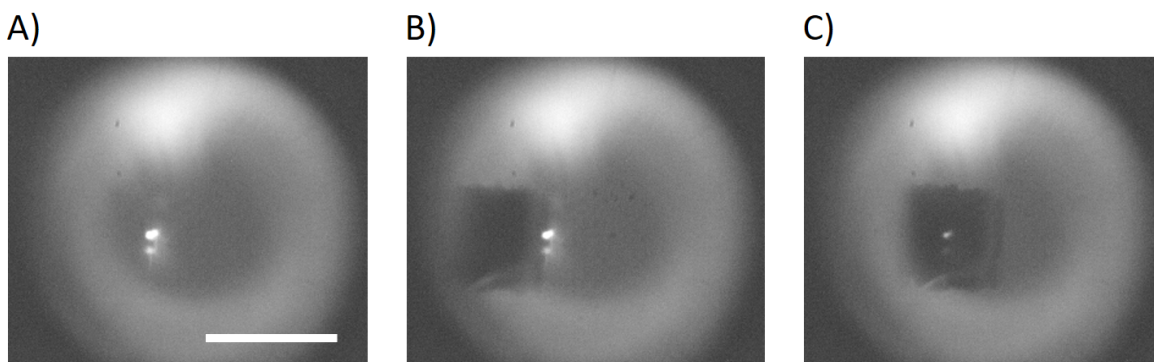
Figure 4.20: Alignment of a PR in the imaged BFP. A) Image of the BFP without PR, showing the tightly focused laser spot saturating the camera. An out-of focus beam (bright spot of ~ 1 mm diameter) from a halogen lamp provides the illumination for the PR alignment. B) BFP image after inserting a square-shaped PR in plane P_4 (from Fig 4.18), creating a shadow in the halogen light. The PR is in focus, but not laterally aligned. C) Aligned PR. Scale bar 0.5 mm.

It is important to note that since the exact BFP is accessed, the illumination beam appears as a focused spot, unlike the previous configuration with the PR as beam

splitter (section 4.3.1). This means that the size of the silver disc can be reduced, while still overlapping with the entire iSCAT reference signal. Furthermore, the radius of the NA circle in this plane is only

$$r_{BFP-1} = r_{BFP} M_{BFP-1} \approx 1.08 \text{ mm} , \qquad (4.32)$$

where $r_{BFP} \approx 4.3$ mm is the radius of the NA circle in the original BFP (table 4.2), and $M_{BFP-1} = 0.25$ the magnification of the BFP in plane P_4. Hence, the PR diameter must be smaller than ~2.1 mm, otherwise it would reduce the entire scattered signal collected by the objective as well, instead of the reference signal only, which would result in a non-selectively reduced iSCAT signal without any enhancement. The smaller the PR, the less of the scattered signal is affected, i.e. the more the iSCAT signal is enhanced.

In order to fabricate smaller PRs, a new method is needed, since drilling a sub-millimetre diameter hole into the relatively thick aluminium mask is challenging and not likely to yield reliable sputtered films, due to the high aspect ratio of the resulting hole. In order to obtain a thinner mask, which is in good contact to the glass surface and able to produce small features, an alternative straightforward approach was chosen. Two stripes of copper tape are first attached to the substrate, only leaving a narrow line gap. In a second step, two additional stripes are put down on top, in the same configuration but at $90\,°$ with respect to the first stripes. The intersection of the two narrow line gaps, corresponding to a small rectangle, is the only feature that remains unmasked. The substrate is then ready for sputtering. With this method, squares of side length smaller than 0.5 mm can be obtained (Fig 4.20). The exact size and shape of the PR can not be reproduced well with this method. This is not of great concern [31], as the priority is to block the entire focused spot of the laser, while keeping the PR as small as possible.

The effect of the PR in the BFP is demonstrated in Fig 4.21, where a regular iSCAT PSF is compared to NA-filtered iSCAT with two PRs of different thickness. Note that for obtaining a real-space iSCAT image of the sample, the lens L4 must be flipped out of the beam path. At first, the regular iSCAT PSF from a dirt particle on a glass slide is imaged, without PR in the BFP, showing the well defined rings. While keeping the exact same illumination and field of view on the sample, a PR of thickness $t = 40$ nm is then inserted. The resulting PSF shows a ~ 5 times brighter central peak. The
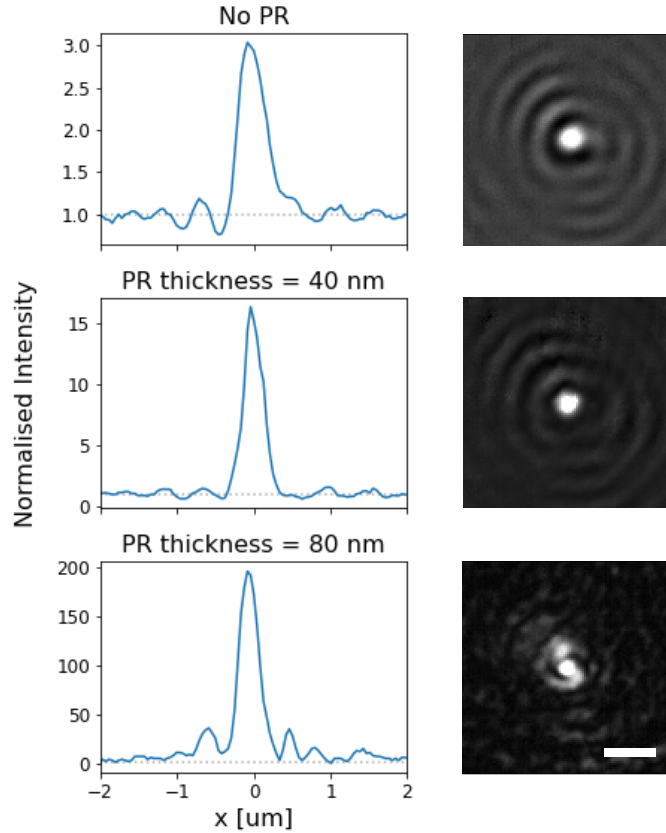
Figure 4.21: Three normalised iSCAT images of the same dirt particle on a dry glass coverslip. The right column shows the normalised PSFs, the left column shows the corresponding profiles along the x-axis through the PSF centre. (top) Regular iSCAT without PR in the BFP. (middle) and (bottom) iSCAT with PR of thickness $t = 40$ nm and $t = 80$ nm, respectively. Scale bar 1 um. Exposure times are 0.4 ms, 10 ms and 30 ms, from top to bottom, while the laser intensity is kept constant.

extended rings are still visible. When changing the PR to a thickness of $t = 80$ nm, the peak is further enhanced, by a factor of ~ 65 compared to the regular iSCAT peak. Note that the corresponding PSF appears significantly different now, with its peak and only a single, small and bright ring around it. This corresponds much more to the PSF expected in a dark field regime (Fig 4.2 B), rather than the iSCAT PSF, which suggests that the reference light has been attenuated so much that $\frac{|s|}{r} << 1$ doesn't hold anymore, and the pure scattering term $|s|^2$ in Eq 4.1 can't be neglected. Note that when considering the area in the PSF further from the peak centre, a noisy appearing pattern is observed, which is the expected iSCAT signal from glass surface roughness [31].

4.4 Discussion & Conclusion

In this chapter, iSCAT was described and its implementation with combined fluorescence microscopy was presented. A range of tests to confirm, characterise and improve the setup has been carried out. With the resulting setup, the smallest particles that could be imaged by regular iSCAT were 20 nm AuNP. In order to push the limit to weaker scatterers, such as proteins, the noise would need to be further reduced. Increasing the mechanical stability of the setup would be one important step to take. A non-exhaustive list of improvements, inspired by [29] and [61], is given by:

- Change the entire setup architecture. Instead of having a separate floor for the illumination and imaging arm, both could be mounted directly onto the optical bench. The only elevated structure would be the stage plate on the four posts, with the sample stage and the objective. A vertical coupling mirror would be used to connect the horizontal illumination and imaging paths with the vertical axis of the objective. The beam splitter would be mounted on the optical bench, separating illumination and imaging light horizontally.

- The objective is the most important and sensitive optical element in the setup. It should be screwed directly into the stage plate, instead of mounting it on a z-stage with a 3D-printed spacer. With an immobile but stable objective, focusing would then be done with a z-stage that moves the sample. This sample stage should be symmetric and stable, preferably not hanging from one side like the cantilever stage built here for the first setup version.

- Mechanical movement of all optics and their effect on the beam path can be generally improved by reducing the height and length of the beam path, i.e. reducing the height of the posts holding the optics and the space between them.

- Enclosing the beam path helps in two ways. On one hand, clean optics will remain free of dust, and hence not deteriorate the beam quality. On the other hand, vibrations and air currents are reduced.

- The pellicle beam splitter used here consists of a thin, fragile membrane, and is therefore very susceptible to vibrations and air currents. It could be replaced by a thick, wedged beam splitter with an AR-coating. Thanks to the wedged shape, interference artefacts are avoided.

- Any 3D-printed parts might be floppy and unstable, and should be replaced by solid metal parts.

As mentioned in section 4.1.3, a beam scanning setup would be an excellent way of improving the iSCAT image quality. However, as explained in section 4.2.2, it would not be a good choice for studying enhancement with resonant optical gratings.

In section 4.3, the enhancement of the iSCAT signal via NA-filtering was demonstrated, and possible challenges that come with the different approaches were discussed.

As the setup is able to perform both iSCAT and fluorescence microscopy with acceptable performance, it offers a range of possibilities to study grating resonance enhanced microscopy, which is investigated in the next chapter.

Chapter 5

GMR Enhancement of Fluorescence Microscopy

5.1 Introduction

By exploiting the concept of resonant enhancement, the performance and limits of optical microscopy can be pushed further. This does not only apply to scattering-based microscopy, as discussed in chapter 4, but also to fluorescence microscopy [66, 67]. There, fluorophores are excited into a higher energy state by absorbing light of a certain wavelength λ_{ex}, after which they might lose some energy by dissipation of heat and can relax back to a lower energy state via emission of light at wavelength $\lambda_{em} \geq \lambda_{ex}$.

A way of increasing this fluorescence signal is to locally enhance the optical field of the excitation light, resulting in an increased excitation rate. Excellent field hot spots can be obtained with plasmonic nanostructures, leading to reported enhancement factors up to a factor of 1000 [68, 69]. However, the lossy nature of metals limits the amount of generated photons that radiates into free space. Dielectric resonances are able to create enhanced fields as well, but in contrast to metals, they do not suffer from absorption loss, so can store more energy. Additionally, dielectric structures can be designed to enhance the emission rate into resonant modes [70]. Moreover, these modes can have a preferable far field radiation pattern with smaller angles with respect to the sample normal, allowing efficient collection even with a lower NA objective [71]. In a recent report, simultaneous excitation and emission enhancement has been combined in a single GMR grating, resulting in a total enhancement factor of nearly 3000 [6].

94

For the application of resonant grating enhanced microscopy, it is of interest to use gratings of constant period that support a resonance in the entire FoV of the microscope in order to homogeneously enhance all the imaged particles. The required period for a resonance at a given wavelength can be simulated, but a fabricated grating typically does not exactly correspond to the ideal simulated structures, due to fabrication uncertainty. In practice, a number of gratings with a range of different periods is fabricated and measured individually in order to find the exact period required for the real structure to resonate. To quantify any enhancement, it is then useful to image particles both on the resonant grating and on a detuned grating off-resonance, for comparison.

In order to reduce the number of gratings and experiments required both for finding the resonant period in the first place and for the quantification of the enhancement, I chose to use the chirped GMR grating design (see chapter 3). As it inherently contains a continuous range of periods, a single structure is sufficient both for identifying the resonance and for quantifying the contrast enhancement in a single FoV, i.e. in one single experiment.

I demonstrate this capability with excitation enhancement of fluorescent beads on the setup presented in chapter 4. A small particle size is desirable for a significant overlap with the resonant modes. A low NA objective with a sufficiently long working distance is required for the GMR fabricated here in the high quality commercial Si_3N_4 on a 500 nm thick substrate. Fluorescent beads of a relatively small size can still yield strong signals that are detectable with an objective of low NA, even without enhancement, which is important for the control measurement.

5.2 Methods

5.2.1 Setup & Fluid Channel Design

The fluorescent beads chosen for this experiment are 100 nm orange beads (Thermo Fisher Scientific, F8800, carboxylate-modified). These beads can be excited with the green laser of wavelength $\lambda_{ex} = 520$ nm. In order to provide a homogeneous illumination of the entire field of view, the laser is mounted above the sample in a transmission setup, where the transmitted excitation beam and the fluorescence signal are collected with a 20x objective (Olympus, NA 0.4) from below.

The emission peak of the orange beads is at $\lambda_{em} = 560$ nm. An appropriate dichroic

mirror for separating the transmitted excitation light from the fluorescence signal and directing them into their respective imaging paths is given by the Thorlabs DMSP505R, which has a cut-off wavelength of $\lambda_c = 505$ nm at $45°$ incidence. Remember that in the setup, the dichroic mirror is mounted at a small incident angle of $3°$, which red-shifts the cut-off wavelength by ~ 50 nm, resulting in an effective cut-off at $\lambda_c \approx 555$ nm (compare to Fig 4.12).
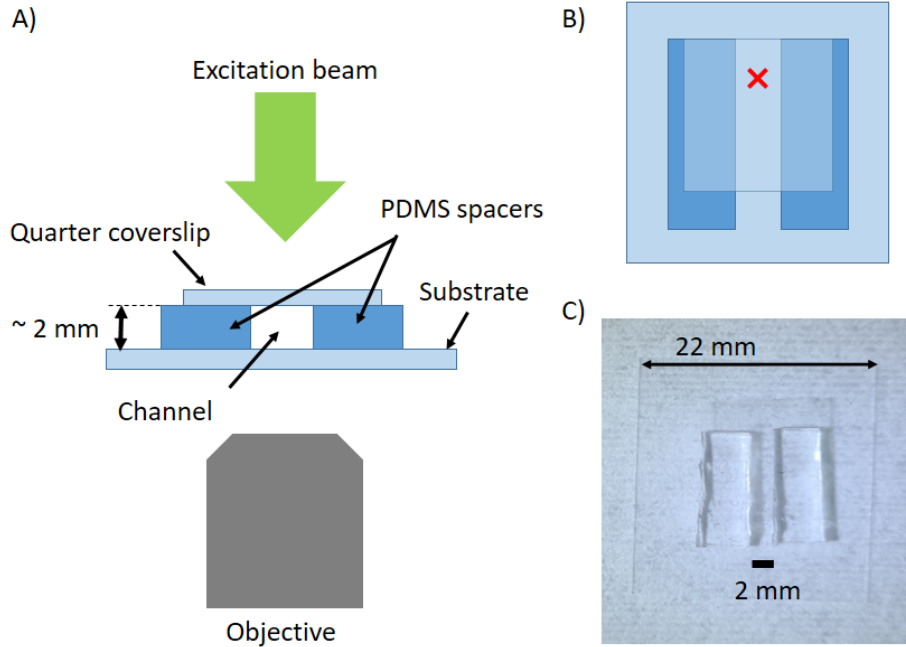
Figure 5.1: Fluid channel for transmission illumination. Schematic front view (A) and top view (B) of the channel. The red cross indicates where the grating is to be located in the channel. C) Photo of a channel in top view.

For the excitation beam not to be distorted, a channel with a flat top surface is required. In the proposed design shown in Fig 5.1, two PDMS stripes are placed on either side of the grating, which are used both as side walls and as spacers supporting the coverglass that is placed on top. This channel can be filled with 30 ul of DI water with a syringe accessing from the front opening of the channel. The water is held inside the channel by capillary forces. With the grating immersed in water, it is possible to focus the optical system on the grating surface and move the FoV to the resonance.

The stock suspension contains $3.6 \cdot 10^{13}$ beads/ml. For an appropriate bead concentration on the grating, the suspension is diluted 1:1000 in DI water. A 3 ul drop of the diluted bead suspension is gently injected at the front channel opening. From

there, the beads diffuse towards the grating and can be observed as they arrive and land on the grating surface. The surface is functionalised with polylysine (details in section 4.2.5) in order to immobilise the beads once they make contact.

5.2.2 GMR Design

A chirped GMR-grating is designed in Si_3N_4 on a glass substrate with water as medium, see chapter 3 for details on the choice of materials. I chose the TM^{-1} GMR mode, as it has field hotspots on the surface of the ridges facing the top, where they are accessible for the beads, unlike the TE^{+1} GMR mode with its hotspots in the gap between the ridges (see Fig 2.10). The resonant period is found by simulating the period spectrum in S^4, see Fig 5.2 A). The TM^{-1} resonance is found at period $a_{res} = 316$ nm. Therefore a range of several tens of nm's around a_{res} is fabricated in order to make sure that the desired resonance can be observed.
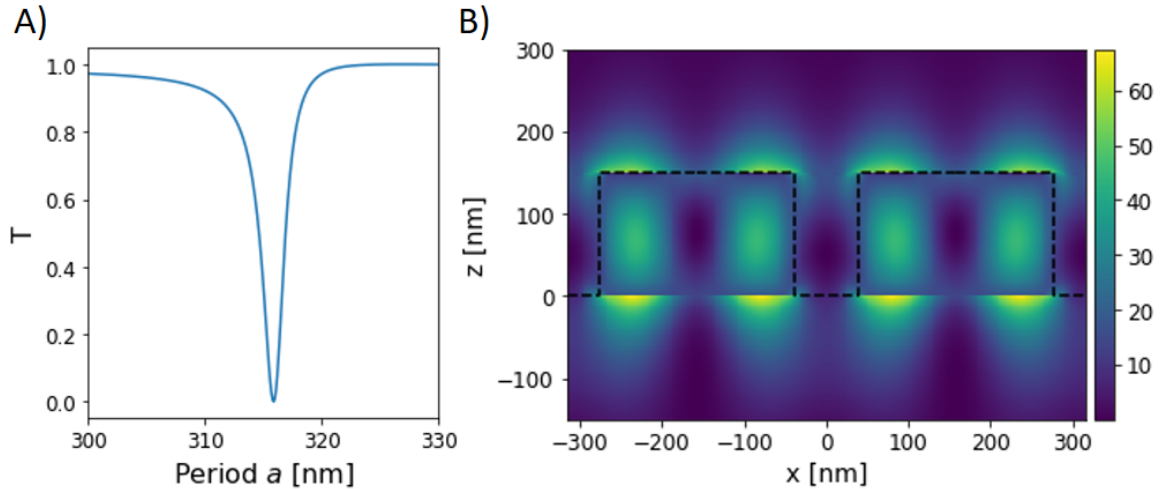
Figure 5.2: S^4 simulations for GMR grating design. A) Transmission period spectrum with TM-polarised light at normal incidence and $\lambda = 520$ nm. Q-factor = 142. B) Electric field intensity $|\mathbf{E}|^2$ for the TM GMR mode at period $a = 316$ nm. Black dashed line: edge of grating.

Fig 5.2 B) shows the simulated electric field intensity $|\mathbf{E}|^2$ of the GMR mode. As the intensity is normalised to the incident wave, it directly shows the expected excitation enhancement at given points in space. Local intensity maxima are observed above the grating ridges, with intensity enhancement of ~ 50. At 100 nm above the grating, the enhancement drops to ~ 10. The expected enhancement for a 100 nm bead is given by an average over the entire bead volume, and therefore limited to a factor a few 10's.

It is worth noting that in the centre of the ridge, the field is very weak, which means that a bead experiences different field strengths depending on its lateral position on the grating.

5.2.3 Spot Detection

In order to quantify the enhancement of the fluorescence signal, single beads are detected and measured. A high number of measured spots is desirable for the results to be statistically meaningful. However, for the detection and measurement of one bead not to be disturbed by the signals of neighbouring beads, the density of beads on the surface would have to be kept sufficiently low. Moreover, if there is a background signal, e.g. due fluorescent particles in the out-of-focus volume, it should be subtracted for a correct spot intensity measurement.

In order to address these points, a relatively high bead concentration is used, in combination with a differential pre-processing step. For each frame i in the raw video, the average of frame $i-2$ and $i-1$ is subtracted from the average of the frames i and $i+1$. Note that this differential processing is similar to the ratiometric processing discussed in section 4.1.7, only that the average frames are subtracted instead of divided. The resulting differential frames successfully reveal the arrival of new beads on the substrate surface despite the presence of other immobile beads, as demonstrated in Fig 5.3.

With the chosen averaging number $N = 2$, the intensity of a landing spot in the differential video ramps up to its maximal value and down to zero in a total of three frame steps. These small tracks are detected with the TrackMate plugin [72] for ImageJ. If a track contains less than three spots, it is likely due to noise that was wrongly detected as a spot, and is hence filtered out in a post-processing step.

5.3 Results

A schematic of the fabricated chirped grating is shown in Fig 5.4 A) and illustrates the orientation of the chirp for the acquired images. An image of the green laser transmission through the grating is shown in Fig 5.4 B). The GMR mode of interest can be identified by the dark vertical line in the centre. This image can be averaged along the y-axis in order to obtain a period spectrum, see Fig 5.4 D). A resonant period of $a_{res} = 344$ nm is observed.
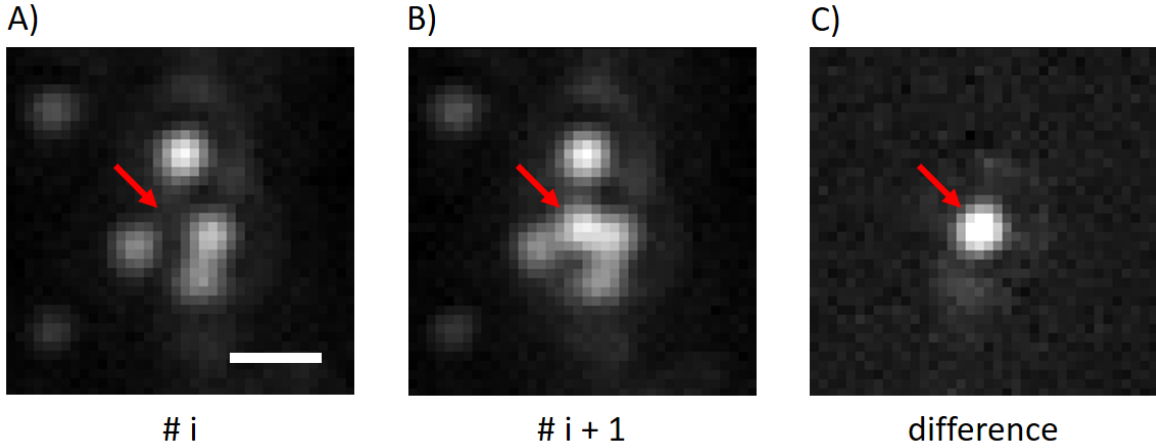
Figure 5.3: Landing of a fluorescent bead. A) A fluorescence image of several beads immobilised on the substrate surface. B) One frame later, another bead has landed (red arrow). C) Differential frame revealing the landing bead.

The fluorescence image in Fig 5.4 C) shows beads that have landed on the grating surface. It is clearly apparent that a number of beads are significantly brighter than others, and they appear on a vertical line in the centre of the image. To make sure that this enhanced brightness corresponds indeed to the resonance observed in the transmission image discussed above, a simple estimation of the enhancement period spectrum is obtained by averaging the fluorescent image along the y-direction, see Fig 5.4 E). In fact, the peak of fluorescence brightness agrees with the $a_{res} = 344$ nm found with the transmission period spectrum.

Fig 5.4 F) shows the histograms of the measured spot intensities in the bright central region (on resonance) and the darker regions on either side of it (off resonance). Off-resonance (blue), the intensity peak is centred at $I = 10^{1.4} = 25$. In contrast, the intensity on resonance (red) has a wider peak centred at $I = 10^{2.1} = 125$, reaching maximal values of $I \approx 10^{2.9} \approx 800$, corresponding to enhancement factors of 5 and 32 with respect to the off-resonance peak, respectively. The wide spread of the on-resonance intensities can be explained by the non-uniform field distribution, i.e. the position dependence of the enhancement (see Fig 5.2 B).
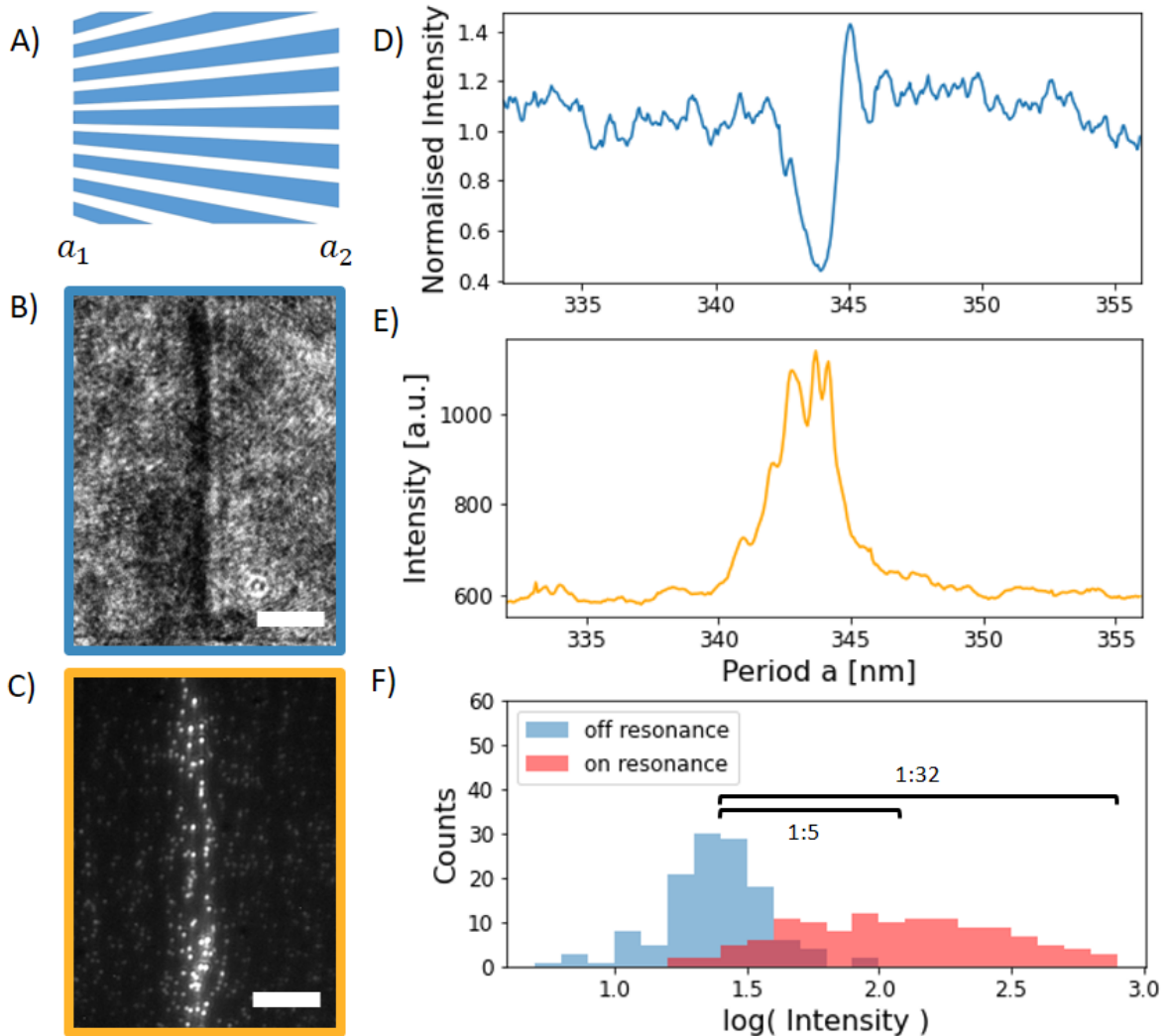
Figure 5.4: Excitation enhancement of fluorescent beads. A) Schematic showing the orientation of the chirped grating, with a smaller period a_1 on the left, linearly increasing along the x-axis to the higher period a_2. B) Image of the grating with green laser illumination in transmission. C) Fluorescence image of beads on the grating surface. Scale bars 20 um. D) and E) are corresponding period spectra, i.e. averages along the y-axis of B) and C), respectively. F) Histogram of spot intensities measured in the bright central line in C) (on resonance) and in the dark regions on the either side of it (off resonance).

5.4 Discussion & Conclusion

In this chapter, I demonstrated how a chirped GMR grating can be used in a simple and efficient experimental setup to show and quantify excitation enhancement in fluorescence microscopy.

The experimentally observed enhancement is centred at a factor of 5, reaching values up to 32. This is in agreement with the maximal predicted excitation enhancement of the order of a few 10s. Moreover, the values are comparable with the enhancement factor of ~ 23 (solely due to excitation enhancement) reported for a similar dielectric grating in [6].

Despite the broadened distribution of the enhanced signals, the intensity can be enhanced significantly, which is most desirable for applications where the particle count is of interest, and a sufficient SNR is required.

It can be interesting to compare GMR enhanced microscopy to the well established technique of total internal reflection fluorescence (TIRF) microscopy. In TIRF, a prism or a high-NA oil immersion objective is used to create an evanescent excitation field on the surface of a regular glass substrate via TIR. When choosing the correct high angle of incidence, an excitation enhancement factor of ~ 3 can be obtained [73], which is almost as high as the values I reported with the GMR. In terms of complexity, both techniques are comparable: TIRF requires the specific illumination setup but no nanofabrication. In contrast, the GMR method can be used with a simpler setup at normal incidence (no need for a prism or oil immersion objective), but the nanofabrication of the gratings is an additional required step. With both methods, advantageous evanescent fields on the substrate surface help suppressing background signals of fluorophores in the bulk liquid further away from the surface. Finally, the main advantage of the GMR method is the possibility to design the grating such that not only the excitation but also the emission is enhanced, which can also lead to an improved collection efficiency [6].

Chapter 6

2D Material Lasing

6.1   Contributions and Publication

This chapter is the result of a collaborative project led by Dr Yue Wang. I joined the project after it started and contributed at first with simulations assisting the choice of grating parameters and supporting the interpretation of the measured spectra. I was then involved with the design and performance of experiments allowing the polarisation dependent characterisation of the excitation and emission enhancement. I further contributed with finding and implementing a suitable method for the processing of cold cavity spectra, in order to successfully fit and extract the information of interest. Additionally, I took part in the planning and building of the extension of the existing setup that allowed measuring the far field radiation patterns. I was also involved with the interpretation of results and project planning.

The results are about to be submitted in the form of a research article with the title "Comprehensive evidence of lasing from a 2D material enabled by a dual-resonance metasurface", of which I am joint first author together with Dr Isabel Barth. The contributors will appear in the article in the following order: Isabel Barth, Manuel Deckart, Donato Conteduca, Guilherme S Arruda, Zeki Hayran, Sergej Pasko, Simonas Krotkus, Michael Heuken, Francesco Monticone, Thomas F Krauss, Emiliano R Martins, and Yue Wang.

6.2   Introduction

Transition-metal dichalcogenide (TMD) monolayers are promising gain materials for lasing applications where high output power is not necessary. When optically pumping a TMD, it can absorb a photon of larger energy than the band gap, which excites an electron from the valence band into the conduction band. The electron in the conduction band and the hole that it leaves behind in the valence band are attracted to each other through coulomb interaction, which allows the formation of a bound state called an exciton. The energy it would take to separate the pair in order to obtain a free electron and a free hole corresponds to the binding energy of the exciton. In TMD monolayers, excitons have a high binding energy ~ 0.5 eV [74, 75] - one to two orders of magnitude higher than the binding energies of conventional gain materials [76, 77] - which makes them stable at room temperature. The high exciton binding energy is important, because it increases the probability for radiative recombination, corresponding to a small radiative life time.

A photon can be emitted through the recombination of the electron-hole pair, which is referred to as photo-luminescence (PL). Unlike the bulk material, a TMD monolayer has a direct band gap [78], making it an efficient light emitter. WS_2 is a particularly interesting material, as it has a longer exciton lifetime [79] and higher gain [80] than other TMDs. Despite the high quantum efficiency, the gain is limited by the extremely thin geometry of the monolayers (thickness <1 nm). In order to achieve lasing, a high quality cavity is therefore required.

A number of 2D-material laser devices with high-Q dielectric resonators have been reported. Microdisk resonators [81, 82] and photonic crystal defect cavities [83] can provide the necessary Q-factor, but the lasing area is small (micron-scale), which limits the output power. Larger lasing areas can be achieved with distributed cavities, e.g. with a vertical cavity surface emitting laser [84] or a photonic crystal slab geometry [85]. The latter can support extremely high-Q BIC modes [16], with which laser designs using conventional gain media have been demonstrated [86–88]. A "pseudo-BIC" laser with 2D-material gain medium was reported with a distributed cavity that is laterally confined to an area of diameter $d \approx 10$ um [89], where the size and quality of the monolayer flake may be the limiting factor for the lasing area. With the common mechanical exfoliation methods, monolayer flakes with diameters on the micron-scale are usual. However, it was shown in recent reports that high quality wafer scale WS_2

monolayers can be grown by metal-organic chemical vapor deposition [90], which lifts this limitation.

Here, we introduce a rectangular lattice nanohole array for enhancement of both the excitation and the PL emission with distributed cavity resonances. Similar resonant pumping approaches to improve the pump efficiency and lower the lasing threshold have been reported in the literature with conventional gain material [91, 92]. Together with the large area monolayer, we achieve a large lasing area for high spatial coherence and high output power compared to other 2D-material lasers. Because of its high output power, it is possible to fully characterise the laser. The lasing criteria for 2D-material lasers with microcavities are summarised in [93], and include the threshold behaviour, linewidth narrowing, polarisation, coherence in time and space as well the quantum condition, which stipulates that there should be at least one lasing photon in the cavity at any one time.

6.2.1 Threshold

Below threshold, spontaneous emission slowly increases with the pump power P_{pump}. In the classic definition, the threshold is reached when P_{pump} is sufficiently high for the gain to compensate the cavity losses. Above threshold, with the light amplification through stimulated emission and the feedback from the cavity, the output power increases much faster with P_{pump}. A plot of the output power versus P_{pump} therefore shows a characteristic "kink" at the threshold. For macroscopic lasers with weak coupling β of the spontaneous emission to the cavity, the kink is very clear. However, for microcavity lasers with high spontaneous emission coupling and high absorption loss, the kink is less well defined. The extreme case of $\beta = 1$ would correspond to a situation where each pumped exciton emits a photon into the cavity mode for any P_{pump}, i.e. the output power versus P_{pump} would simply be a straight line without any kink at all.

Especially in cases where β is high, a more suitable definition definition of the threshold is given by the pump power required for stimulated emission to overtake spontaneous emission. This corresponds to the quantum threshold condition, where the mean photon number is unity. [94]

6.2.2 Linewidth Narrowing

As described in Chapter 1 and 11 of [95], below the lasing threshold, both the amplitude and phase of the field in the cavity slowly fluctuate, following the statistics of a narrow

band Gaussian noise source. The Schawlow-Townes equation describes the linewidth of a laser oscillator, which below threshold is given by

$$\Delta\omega_{osc} = 2 \cdot \frac{N_2}{N_2 - N_1} \frac{\pi\hbar\omega\Delta\omega_c^2}{P_{osc}} \ , \tag{6.1}$$

where N_1 and N_2 are the populations in the lower and higher energy level, respectively, $\Delta\omega_c = \frac{\omega}{Q_c}$ the cold cavity linewidth and P_{osc} the free running output power of the laser.

Above the lasing threshold, the light in the cavity corresponds to a coherent sinusoidal oscillator, where the amplitude is stable and only fluctuates little around its steady-state value and the phase slowly drifts or fluctuates as random noise. The linewidth above threshold is then given by

$$\Delta\omega_{osc} = \frac{N_2}{N_2 - N_1} \frac{\pi\hbar\omega\Delta\omega_c^2}{P_{osc}} \ . \tag{6.2}$$

The two equations clearly show that passing the threshold leads to a linewidth narrowing of a factor of 2. Note that these equations describe a system that is limited by quantum fluctuations due to spontaneous emission, i.e. other sources of noise may broaden the linewidth, e.g. thermal drift, accoustinc noise or mechanical vibrations.

6.3   Methods

6.3.1   Simulations

The nanohole array is designed via simulations of the reflection spectra using S^4. Same as for the 1D gratings simulated in section 2.8.6, the spectra converge sufficiently for 21 spatial harmonics.

The simulated layers and their thickness and refractive index are listed in Fig 6.1. The refractive indices do not change significantly between the two wavelength ranges of interest, hence they can be assumed constant for simplicity.

6.3.2   Transmission Band Diagram

The photonic band structure of the nanohole array is obtained from transmission spectra at various incidence angles. The angle θ_i relates to the in-plane wave vector component $k_i = k_0 \sin(\theta_i)$, where $i \in \{x, y\}$.

Incident light

material	thickness [nm]	index @532 nm	index @655 nm
Air	∞	1	1
PMMA	400	1.4934	1.4881
Si_3N_4	150	2.0559	2.0368
Borofloat33	∞	1.4739	1.4693
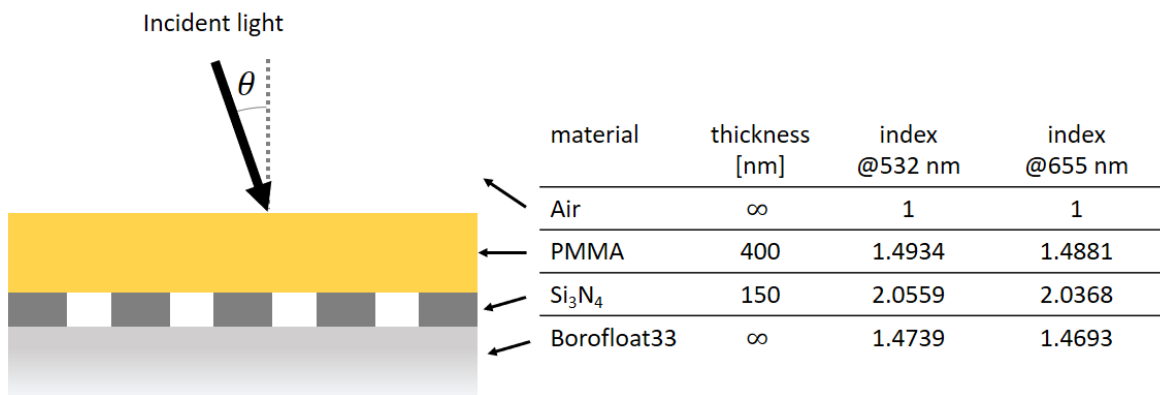
Figure 6.1: Illustration of simulated layers with corresponding thickness t and refractive index n of the Borofloat glass substrate [96], Si_3N_4 [23] and optional PMMA layer [97]. The holes in the grating layer consist of air with $n = 1$.

For visualising the band gap of the resonances along the short period a_y, the sample is rotated to vary θ_y, while keeping $\theta_x = 0$. On the other hand, for the resonances along a_x, θ_x is varied, while keeping $\theta_y = 0$.

WL   Sample   Spectrometer
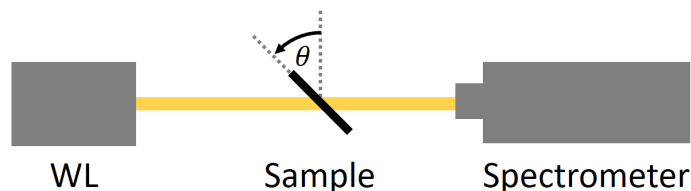
Figure 6.2: Schematic of the setup for angle resolved transmission spectra. Light from a white light source (WL) is directed onto the sample on a rotation mount. The transmitted light is analysed by the spectrometer (Acton Spectrapro 2750).

6.3.3   WS$_2$ Laser Fabrication

We use monolayer WS$_2$ grown on a 2 inch sapphire substrate by AIXTRON Ltd. using metal-organic vapour deposition. A 400 nm thick Poly(methyl methacrylate) (PMMA) layer is spun onto the WS$_2$ as a carrier layer. Centimetre-sized monolayers are then delaminated from the sapphire substrate through buffered oxide etching. In a final step, the monolayers on PMMA are transferred from the sapphire substrate onto the nanohole array, using a wet-transfer process.

6.3.4 Laser Characterisation

The laser device is characterised on a micro-PL setup, as illustrated in Fig 6.3. For optical pumping, a CW laser (Novanta Photonics gem532) is focused by a 4x objective (Olympus, NA=0.1) onto the sample.

The PL from the sample is collected by the same objective and directed towards the spectrometer. A mirror can be flipped into the optical path in order to focus a real space image onto the camera (CoolSNAP Myo). This image is used for determining the pump spot size, which is 154 um in diameter.

A second lens (L2) can be flipped into the beam path in order to image the BFP of the objective, which yields the far field radiation pattern of the PL. A long pass filter (Thorlabs FEL0550) is used to block out the pump light and only image the PL. In a BFP image, the axes are proportional to the in-plane wave vector components $k_i = k_0 \sin(\theta_i)$, for $i \in \{x, y\}$. The pixel number along each axis can therefore be transformed to k_i by centring and multiplying with a calibration factor, which can be found with the radius of the NA-circle.
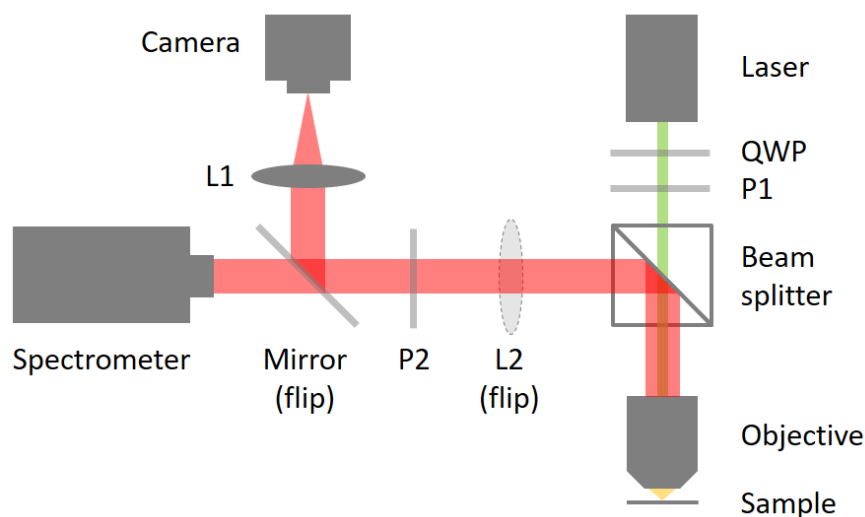
Figure 6.3: Schematic of the micro-PL setup. A mirror and a lens (L2) can be flipped in or out of the beam path for different measurements. Optionally, the orientation of the linear polarisation of the pump laser can be rotated with a quarter wave plate (QWP) and a linear polariser (P1). The polarisation of the PL emission is analysed with the use of a second linear polariser (P2) on the imaging side.

6.4 Results

6.4.1 Grating Design

A schematic top view of the rectangular lattice nanohole array is shown in Fig 6.4. For each direction of periodicity in the nanohole array, a resonant mode has to be chosen and corresponding parameters need to be found. The resonance along the short period a_y is used to match the pump laser in order to enhance the excitation (Fig 6.4 B). The pump laser is focused onto the sample, covering a small angular range of incidence angles. In order to efficiently couple to the resonance with sufficient tolerance, we choose to use the TE^{+1} mode. This mode has a relatively low Q-factor and the electric field is parallel to the grating plane, i.e. it will be well aligned with the WS$_2$ layer in the final device.
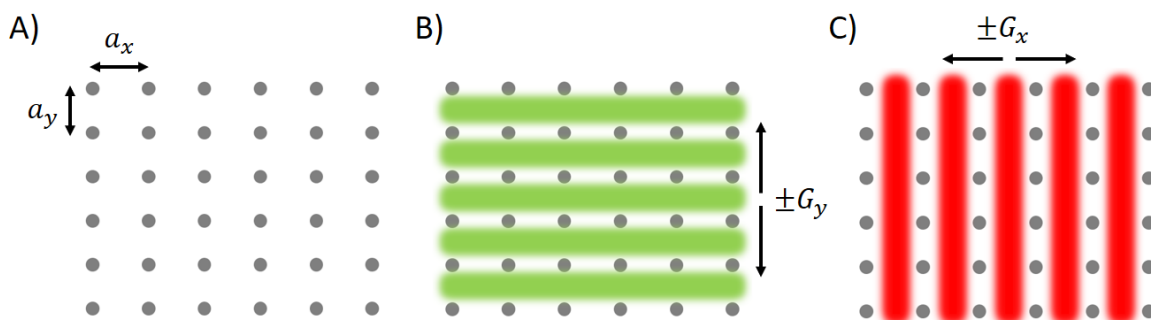
Figure 6.4: Schematic of a rectangular lattice nanohole array and resonances in x and y. A) Array with different periods a_x and a_y. B) Resonance for the pump wavelength $\lambda = 532$ nm, which couples to the reciprocal grating vector G_y corresponding to the shorter period a_y. C) Resonance for the emitted PL of $\lambda \approx 655$ nm, which couples to the reciprocal grating vector G_x corresponding to the longer period a_x.

Along the longer period a_x, a resonance with high Q-factor is wanted, as it will support the lasing mode (Fig 6.4 C). In TM polarisation, two high Q modes are available: The bright TM^{-1} and the TM^{+1}. The latter turns into a BIC at the $\Gamma-$Point, which has an infinite Q in theory. In practice, this mode should yield the highest achievable Q, which is limited by losses of the system, such as scattering and absorption. On the other hand, while the bright TM^{-1} mode has a lower Q, it offers more efficient extraction of photons from the lasing mode into the out-of-plane propagating radiation.

With the choice of the 150 nm thick Si$_3$N$_4$ films on glass substrate, the nanohole array has three geometrical parameters that can be varied in order to obtain the wanted

resonances: the periods a_x, a_y and the hole radius r.

As the aim is to obtain high Q lasing modes, the radius is chosen to be the smallest that can be fabricated reliably, which is estimated to be $r = 75 - 95$ nm. This leaves the two periods to be determined by S^4 simulations. The periods $a_y = 320$ nm and $a_x = 410$ nm yield the desired resonances, as shown in Fig 6.5.
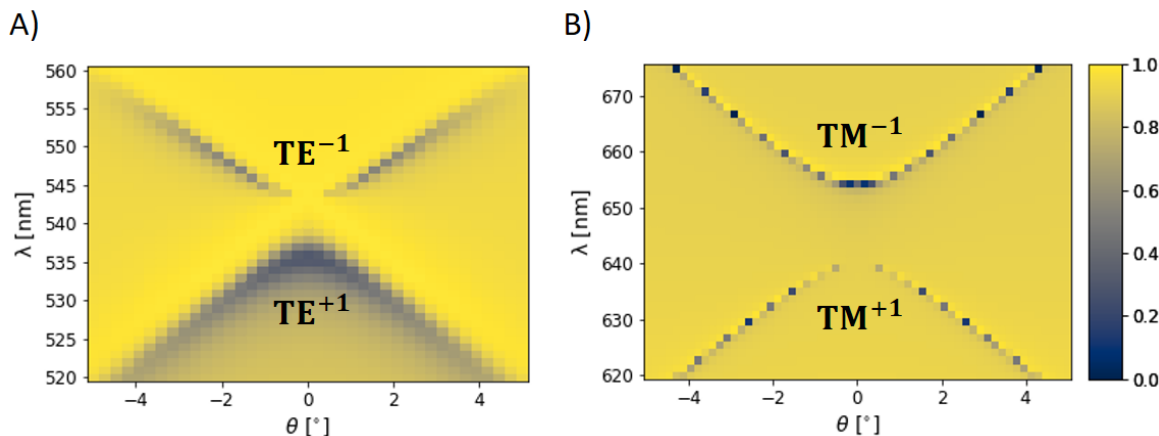
Figure 6.5: Simulated transmission band diagrams of the rectangular lattice nanohole array. A) TE resonances along the shorter period $a_y = 320$ nm. B) TM resonances along longer period $a_x = 410$ nm. Hole radius $r = 95$ nm.

6.4.2   Effect of PMMA layer

During fabrication, a PMMA layer is used as carrier for transferring the WS_2 monolayer from its native substrate to the nanohole array. Once transferred, it is interesting to explore whether the PMMA should be kept or whether it should be removed. One argument for keeping the layer is to protect the WS_2 from the environment. As the refractive index of PMMA is significantly higher than air, it will also affect the mode distribution.

Consider the reflection spectra close to normal incidence shown in Fig 6.6. Removing the PMMA does not only shift the resonances to lower wavelengths, but it also reduces the Q-factor by a factor of 4 for the TM^{+1} and a factor of 2.5 for the TM^{-1} mode. This reduction of Q may be explained by the fact that a lower index of the surrounding medium results in a tighter out-of-plane confinement of the guided mode to the grating layer. Therefore, it has an increased overlap with the vertical side walls of the grating ridges, which leads to stronger scattering, i.e. coupling to the out-of-plane radiation. Why is the Q-factor of one mode more affected than the other? A possible explanation
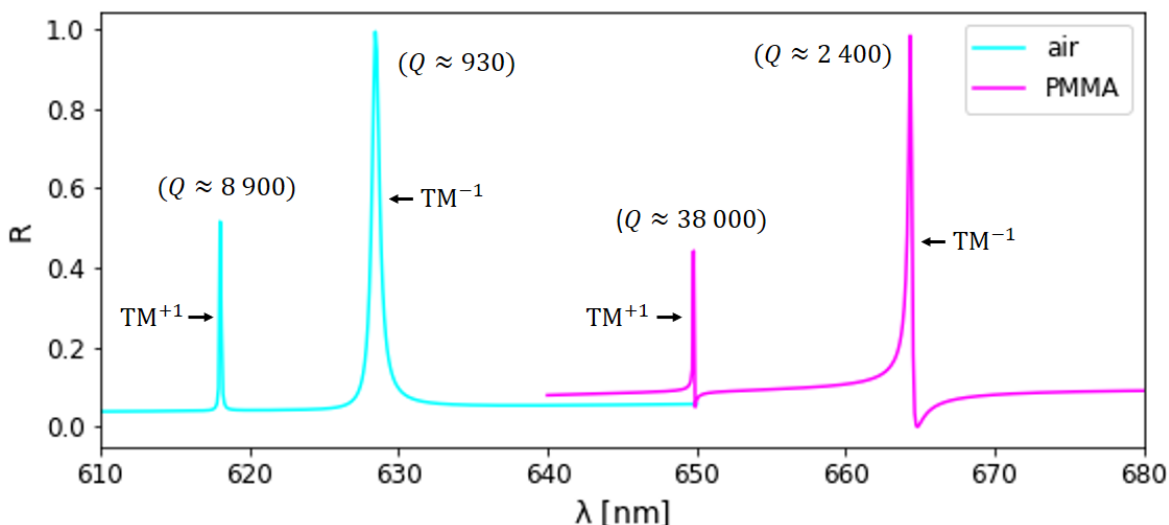
Figure 6.6: Spectra of TM resonance peaks with and without PMMA layer. Periods $a_x = 410$ nm and $a_y =320$ nm, hole radius $r = 75$ nm, $\theta = 0.5°$.

for this difference is given by the effective index. The TM^{-1} mode is on the red side of the band gap, i.e. it occurs at a longer wavelength and has a higher n_{eff} than the TM^{+1} mode, which means its field overlaps more with the high index grating layer, and less with the surrounding layers. Therefore, it is less affected when the index of the top layer is changed.

An important property of the resonance for lasing is the mode overlap with the gain material. It is therefore useful to examine how the PMMA layer changes the field distribution. Fig 6.7 A) shows the electric field intensity $|E|^2$ for the TM^{-1} mode in air. It is clear that the mode is pulled towards the substrate (bottom), since the substrate has a much higher index than air. With the PMMA layer in place, (Fig 6.7 B), the field is much more symmetric in z, as the substrate below and the PMMA above have a very similar index. For comparison, a line profile at a fixed y-coordinate through the hot spots of the fields is plotted in Fig 6.7 C). Note that the maximal intensity in air is ~ 2.5 times lower than for the system with the PMMA layer - the same factor as found previously with the ratio of the Q-factors. In air, the field on the grating surface ($z = 150$ nm) is only half of the global maximal value (at $z = 0$), whereas in PMMA, the maximum itself is reached at z $= 150$ um. This qualitatively shows the advantageous mode overlap obtained with PMMA. The same behaviour is observed for the TM^{+1} mode (Fig 6.7 D-F).
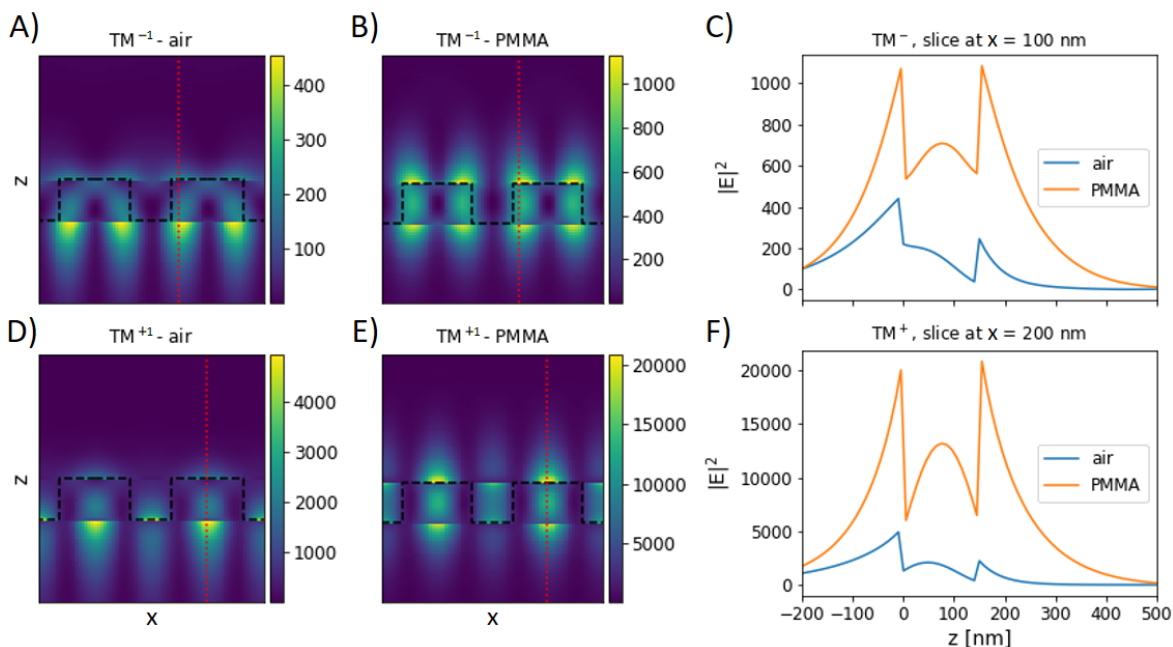
Figure 6.7: Effect of the PMMA layer on the field confinement of TM modes of the longer period a_x. A) and B) Electric field intensity $|E(x, 0, z)|^2$ of the TM^{-1} mode without and with PMMA layer, respectively. Black dashed lines: edge of grating. The substrate is below and the medium is above the grating. C) Corresponding profile plot along z through the hotspots. D-F) The same for the TM^{+1} mode. The top of the grating is at $z = 150$ nm, where the WS_2 is to be placed.

As the PMMA layer improves both the Q-factor and the field overlap, it is not removed in the final lasing devices. Note that this decision is also supported by the fact that no lasing was observed when removing the PMMA layer.

6.4.3 Cold Cavity Characterisation

First of all, collaborators verified that the required geometry of the nanohole array was successfully fabricated, see the SEM micrograph in Fig 6.8. Note that the rectangular lattice has the desired periods of $a_x = 410$ nm and $a_y = 320$ nm. Holes of radii $r \approx 60$ nm have also been achieved.

In a second step, I made sure that the required modes exist and are resonant at the correct wavelengths. To do so, I processed and analysed the transmission spectra that were acquired by collaborators. Recall that the final lasing device has the PMMA layer on top of the WS_2 layer on the grating. In order to characterise the passive nanohole array without the WS_2 layer, a 400 nm thick PMMA layer is spun directly onto the

grating.

Let us first consider the transmission band diagram for the pump resonance, in the green wavelength range (Fig 6.9 A). The TE^{+1} mode is close to the wavelength of the pump laser at $\lambda = 532$ nm. In the red wavelength range (Fig 6.9 B), both TM modes are observed. The TM modes in the red range have a higher Q-factor than the green TE modes, as required by the design. As we are trying to achieve lasing on the TM modes, they are considered in more detail and fitted with a Fano lineshape in order to extract the quantities of interest, such as the resonant wavelength λ_{res} (Fig 6.9 C), the Q-factor (Fig 6.9 D) and the peak amplitude (Fig 6.9 E). The amplitude shows the expected trend, with the TM^{+1} mode disappearing at normal incidence. However, the Q-factor of the TM^{+1} does not show the expected trend towards infinity. Instead, it appears constant in the considered range of angles and exhibits a large uncertainty at $\theta \approx 0°$, which can be easily explained since the amplitude is extremely low, hence the signal-to-noise ratio is near or below unity. We note that the Q-factors are similar for both TM modes, which is not due to the spectrometer resolution of ~ 0.03 nm. The Q-factor limitation is in fact explained by the presence of loss (section 2.12), which is due to scattering at imperfections and surface roughness. The TM^{+1}, which has a much higher theoretical Q, is more affected by the losses than the TM^{-1} mode, as they both have a similar total Q.
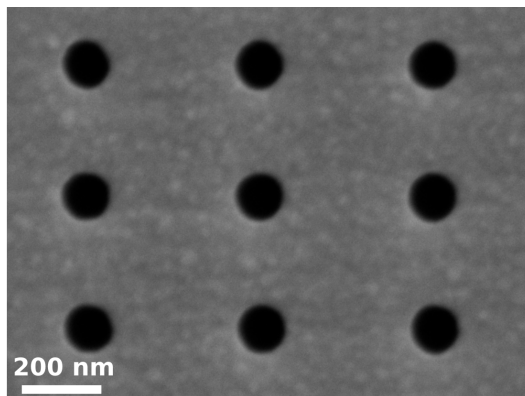
Figure 6.8: SEM micrograph of the rectangular lattice nanohole array.

6.4.4 PL Emission Enhancement

We now consider the final device including the active WS$_2$ monolayer. By using a quarter wave plate and a linear polariser in the illumination path, the incident light can be linearly polarised to match the pump resonance or to be completely orthogonal
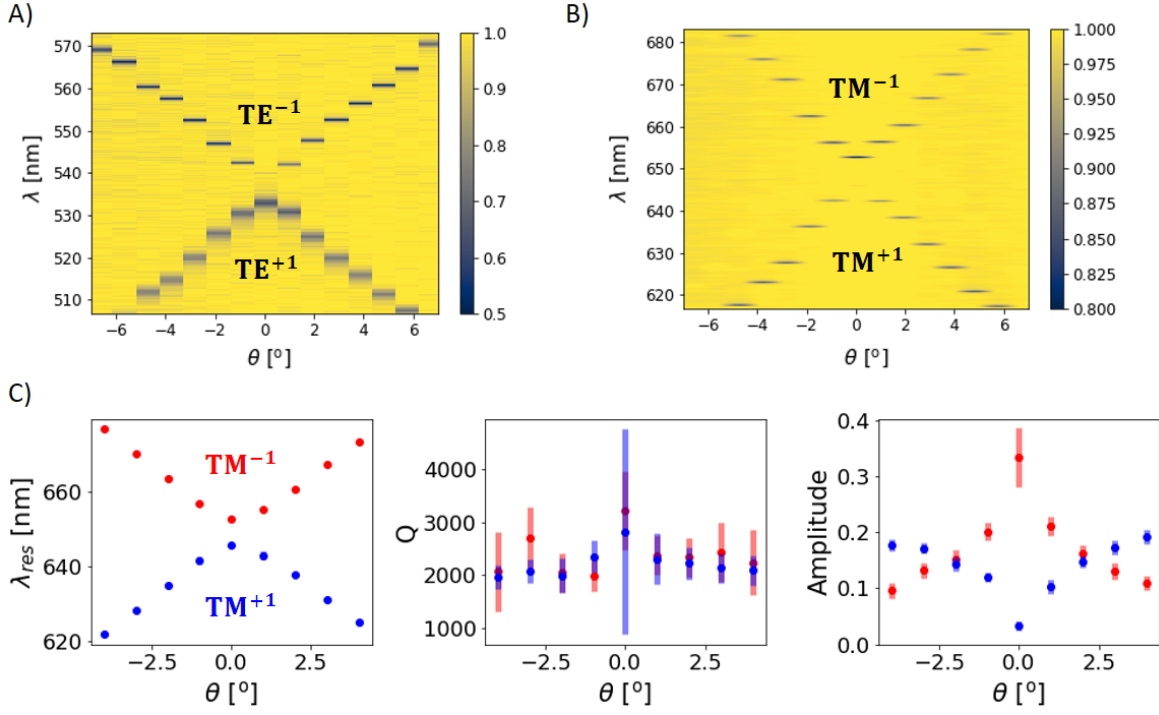
Figure 6.9: Measured transmission band diagrams, normalised to the thin film background of the grating. A) TE resonances along the shorter period $a_y = 320$ nm. B) TM resonances along the larger period $a_y = 410$ nm. C) Parameters extracted from B) by fitting Fano lineshapes to each peak.

to it. This way, the enhancement from the resonant pump can be investigated. Fig 6.10 shows the PL spectra on unpatterned Si_3N_4 background and on the nanohole array for polarisation angles $\phi = 0°$ and $\phi = 90°$. The background spectra are very similar for both input polarisations, as expected. A much stronger difference is seen on the nanohole array, where both spectra have the same shape but an amplitude strongly depending on the input polarisation. In order to quantify the enhancement, both spectra are integrated in the wavelength range $\lambda \in [590, 690]$ nm. This wavelength range has been chosen to capture the full spectrum. The input polarisation at $90°$ matches the TE^{+1} pump resonance and has an integrated spectrum that is enhanced by a factor of ~ 2.6 compared to the $0°$ polarisation, which does not excite the pump resonance.

The background spectra show the emission peak of the WS_2 monolayer exciton at $\lambda \approx 618$ nm. The PL on the nanohole array shows additional peaks in the range $\lambda \in [630, 680]$ nm, corresponding to emission enhancement thanks to the resonances
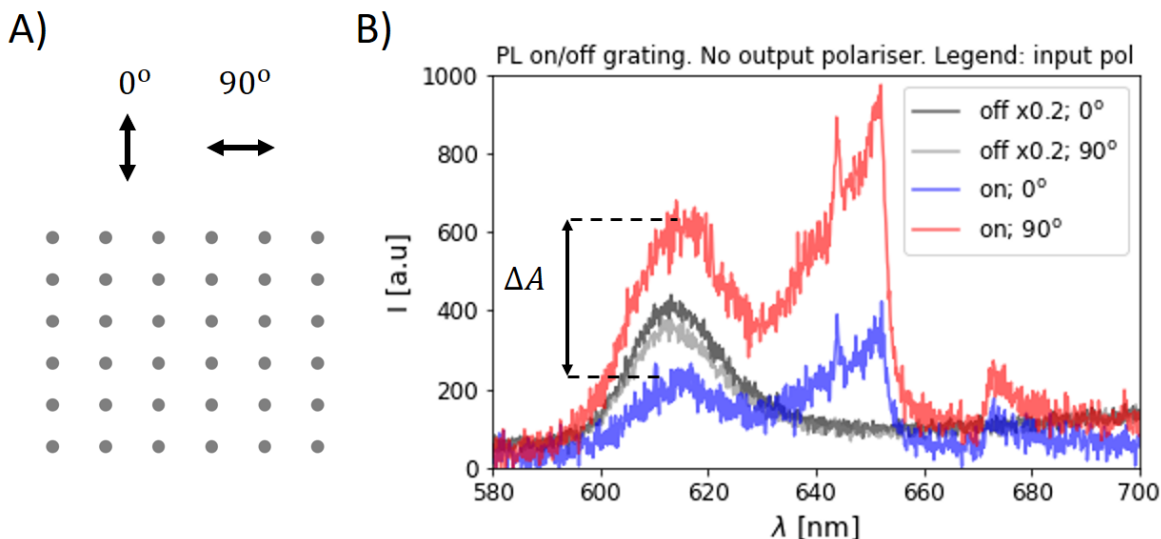
Figure 6.10: Enhancement of the PL emission with a nanohole array of periods $a_x = 405$ nm and $a_y = 325$ nm. A) Schematic top view of the nanohole array, with the orientation of the incident light polarisation for $0°$ and $90°$. No polariser is used on the imaging side. B) PL spectra of the unpatterned Si_3N_4 background and the nanohole array. Off-grating spectra have been integrated for 10 s and are multiplied by a factor of 0.2, in order to allow comparison with the on-grating spectra, for which the integration time is 2 s.

along the longer period a_x. In order to investigate these peaks, a linear polariser is introduced in the optical path before the spectrometer, see the resulting spectra in Fig 6.11. With the imaging polariser at $90°$, the TM-polarised resonances along a_x are measured, see Fig 6.11 A). A single sharp peak is seen at $\lambda = 645$ nm (see comments in the next paragraph). With the imaging polariser at $0°$, the TE-polarised resonances are revealed (Fig 6.11 B). The bright TE^{+1} peak at $\lambda \approx 650$ nm is separated from the smaller TE^{-1} peak at $\lambda \approx 675$ nm by the photonic band gap. Both peaks have a shoulder on the side that faces away from the band gap. The shoulders correspond to off-normal emission angles.

The brightest peak is observed for the TE^{+1} mode, as it couples well with the in-plane electric dipole of the WS_2 layer and the mode has the best coupling to out-of-plane radiation (i.e. lowest Q). The TE^{-1} peak on the other side of the band gap appears less intense, as this mode turns into a BIC at the $\Gamma-$Point, which can not couple to propagating radiation. The sharpest peak is seen for the TM polarisation. As only a single peak appears in this spectrum, it can not be determined with certainty if the peak
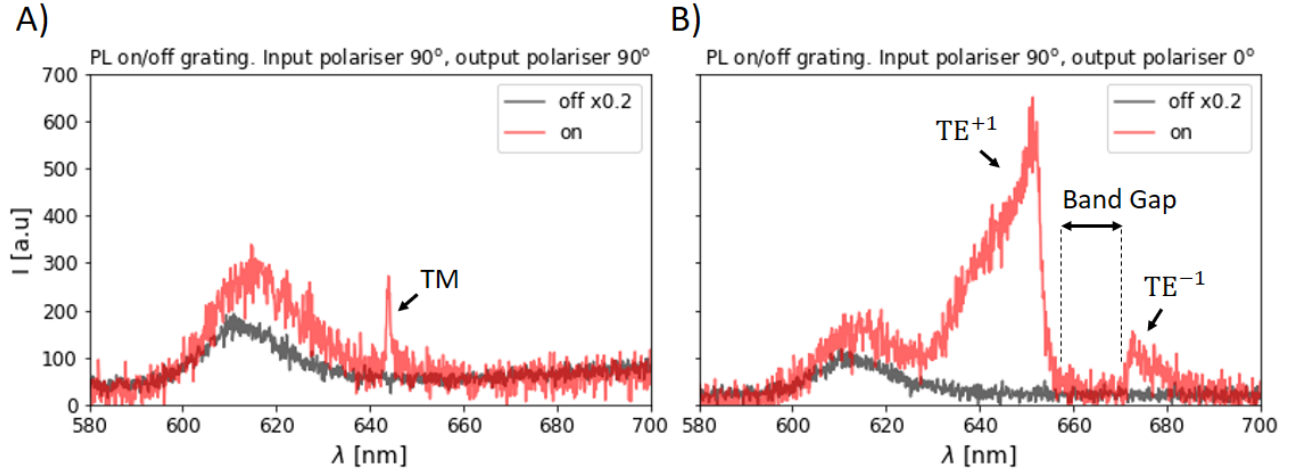
Figure 6.11: PL spectra on and off the rectangular lattice nanohole array, with linear polariser on the imaging side ("output"). The incident light is linearly polarised and excites the TE-mode of the grating along the shorter period. The output polariser at $90°$(A) and $0°$(B) corresponds to TM-polarisation and TE-polarisation along the longer period of the grating, respectively.

corresponds to the TM^{-1} or the TM^{+1} mode, however the hint of a shoulder towards longer wavelengths suggests that it is on the red side of the band gap, corresponding to the TM^{-1} (see band structure in Fig 6.9 B). This is supported by the fact that the TM^{+1} peak is expected to be less intense, as it is on the BIC-side.

6.4.5 Laser Threshold and Linewidth Narrowing

Having characterised the enhancement of both the PL excitation and emission, I now consider the lasing characteristics, starting with the threshold behaviour.

The narrow TM peak in the PL emission is characterised for a range of pump powers, see examples shown in Fig 6.12 A). Note that for low pump powers, the peak can hardly be distinguished from noise, whereas for higher a pump power, the peak becomes clearly visible. All peaks are fitted with a Lorentzian line shape, which is typical for a lifetime-broadened laser peak. The parameters of interest are the amplitude A (Fig 6.12 B), as it is a measure of the laser output power, and the half width γ (Fig 6.12 C). In the amplitude plot, a first threshold can be seen at a pump power $P_{pump} \approx 0.1$ mW. The slope appears to flatten out for increasing P_{pump}, until it abruptly increases to its maximal value for $P_{pump} \geq 0.45$ mW. The transition range $P_{pump} \in [0.1, 0.45]$ mW may correspond to amplified spontaneous emission. With the central pump power of
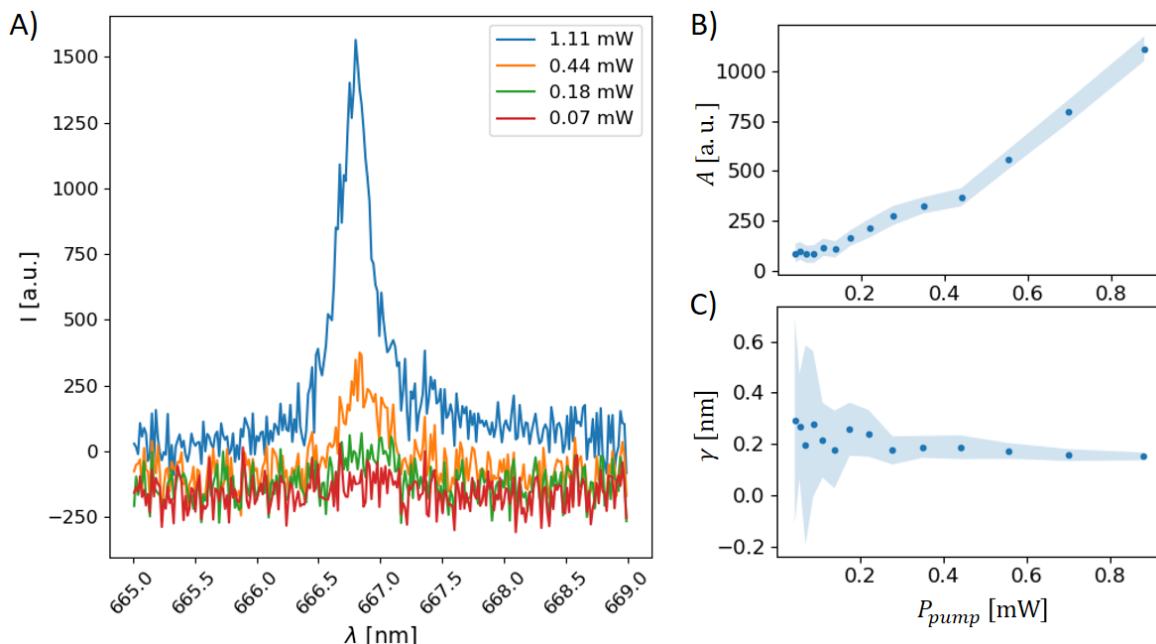
Figure 6.12: Threshold behaviour of a nanohole array with periods $a_x = 425$ nm and $a_y = 325$ nm. A) Example PL spectra at different pump powers. B) Amplitude and C) half width at half maximum of the fitted Lorentzian line shape. The shaded areas correspond to 95 % confidence intervals of the fitted parameters.

this range and the spot size of diameter $d = 154$ um, a threshold pump intensity of $I_{pump} \approx 1.5$ W/cm^2 is calculated. A comparable threshold is obtained with 15 different devices lasing at $\lambda \in [645, 670]$ nm. When pumping at a pump power $P = 1.1$ mW (above threshold), an output power $P_{out} > 20$ nW is measured. This power is an underestimation of the total laser output power, as discussed more in detail in section 6.4.7.

Fig 6.12 C) shows that the half width γ has a significant fitting uncertainty below threshold, due to the low SNR. As the amplitude of the peak increases, the uncertainty of the γ decreases. There are two data points around $P_{pump} \approx 0.2$ mW that show an acceptable uncertainty and a half width of $\gamma \approx 0.25$ nm, which drops down to $\gamma \approx 0.2$ nm for higher pump powers. This corresponds to a linewidth narrowing by a factor of 1.25, which is less than the factor of 2 expected from an ideal laser oscillator (section 6.2.2). A possible explanation is given by the small spatial coherence length in the y-direction (see section 6.4.6), i.e. orthogonal to the oscillation direction x of the lasing mode. The short coherence length is $\sim$ two orders of magnitude smaller than the

pump area. Therefore, if the total lasing area can be considered as ~ 100 independent segments in y that lase without coupling to each other, phase noise between them may cause the broader linewidth.

For most measured lasing devices, a single TM peak is observed, which makes it challenging to tell whether it is the TM^{-1} or the TM^{+1} mode. In rare cases, both modes and the band gap between them can be observed simultaneously, as shown in Fig 6.13 (blue curve). In this case, the modes can be identified according to which side of the band gap they are located on. Minute translations of the sample stage can cause either mode to dominate and lase (yellow and green curves).
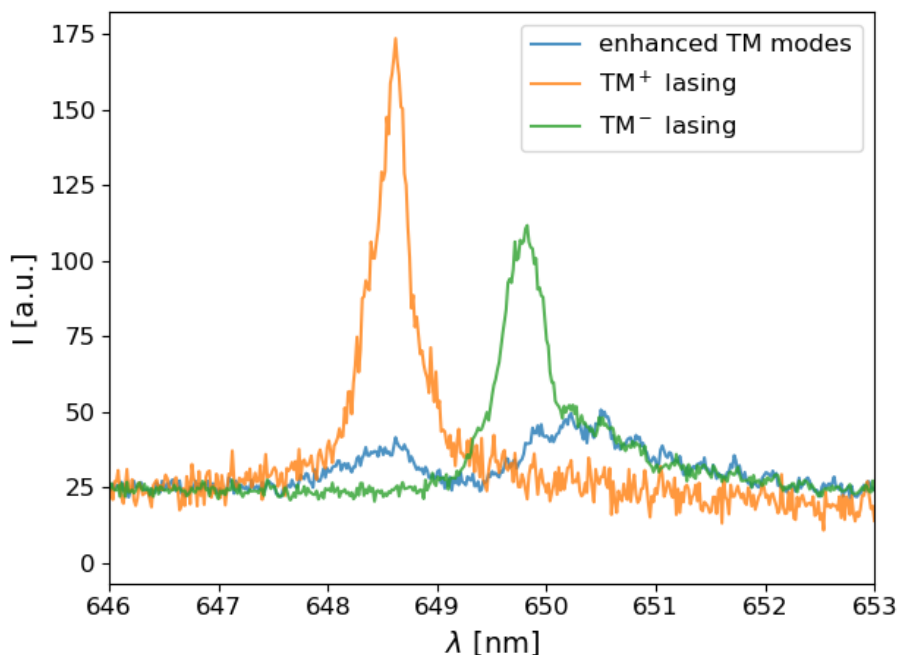
Figure 6.13: Lasing spectra with different TM modes. Periods $a_y = 325$ nm, $a_x = 410$ nm. Spectra are normalised by the integration time and pump power for comparison.

6.4.6   Far Field Radiation Pattern

Coherence is an important property of a laser. Temporal coherence manifests itself as a narrow emission peak in the PL spectrum, since the width of the peak is inversely proportional to the photon lifetime inside the resonator cavity. In contrast, spatial coherence is manifested by the lateral extent of the laser beam.

An example far field radiation pattern for a laser being pumped above threshold
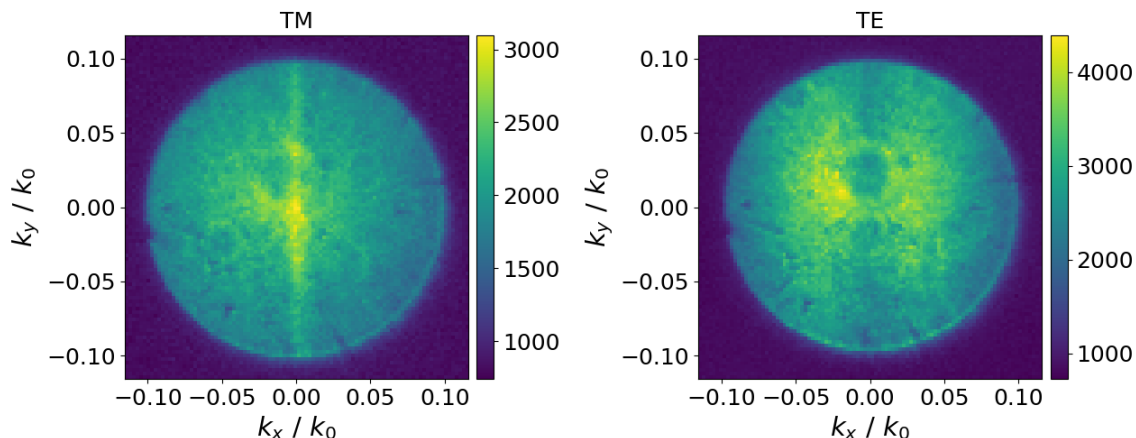
Figure 6.14: Far field radiation pattern for different imaging polarisations.

is shown in Fig 6.14. The angles $\theta_i \approx \sin(\theta_i) = k_i/k_0$ are limited by the NA $= 0.1$ of the objective. A linear polariser is used on the imaging side in order to only detect light from TM (left) or TE-polarised (right) light. The stimulated laser emission is linearly TM-polarised and appears as a bright line at $k_x = 0$. In TE polarisation, the central line disappears, only showing enhanced spontaneous emission at larger, non-zero emission angles corresponding to $|k_x|/k_0 \in [0.01, 0.05]$.

I expected to see a different far field emission pattern when lasing either with the TM^{-1} or the TM^{+1} mode [98]. The TM^{-1} mode can radiate at an angle normal to the surface. As shown in Fig 6.15 (left), the TM^{-1} shows a line in the emission pattern going through the Γ−point. The divergence angle extracted from the k_x-profile (lower panel) is $\theta = 3.5$ mrad. As the TM^{+1} is a BIC at the Γ-Point, it is expected not to couple to propagating waves at $k_x = 0$, therefore showing two narrow bright lines at small $|k_x| > 0$, separated by a dark line, as supported by [98, 99]. However, a dark line is not observed for the TM^{+1} mode, see Fig 6.15 B). Comparing to the TM^{-1} mode, the only difference is the ~ 2.5 times larger divergence angle of $\theta = 8.8$ mrad. The absence of the expected dark line for the TM^{+1} mode might be due to an unintentional systematic asymmetry in the shape of the nanoholes or a phase shift between different lasing regions [100]. Alternatively, it might be explained by an insufficient resolution in the BFP images. The expected width of the dark line can be estimated from [99] as $\sim 20\%$ of the full extent in k_x of the two bright lines together, which would in our case

correspond to a dark line of width $w \approx 3.5$ mrad. The resolution of our BFP imaging system can be roughly estimated by the smallest feature that was imaged with it, i.e. the 3.5 mrad width of the sharp line from the bright TM^{-1} mode. This resolution might indeed just be too low for resolving the expected the dark line.
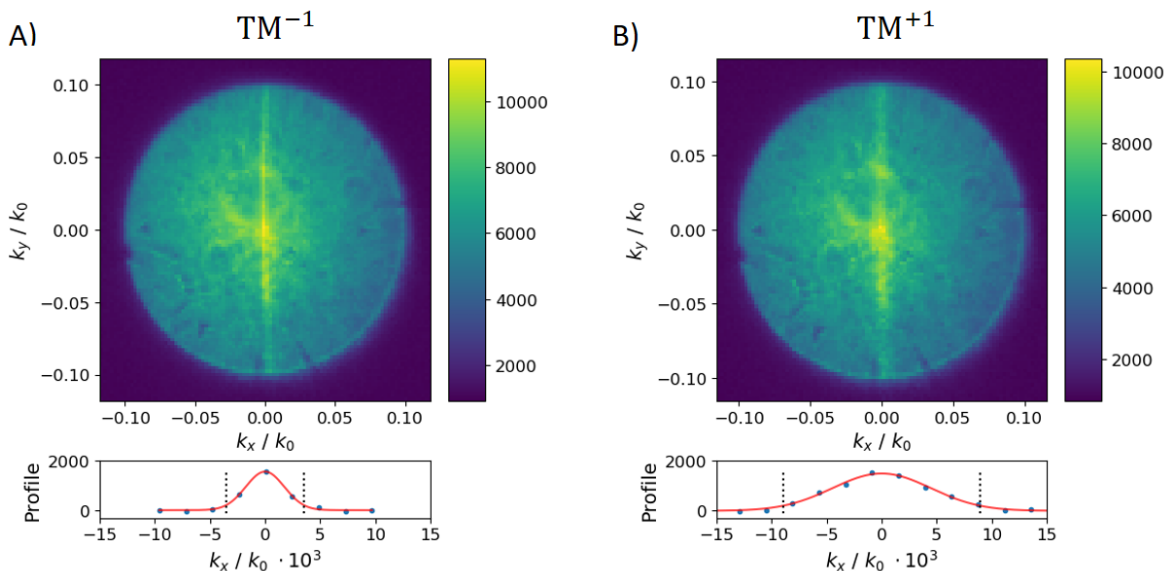
Figure 6.15: Far field radiation patterns for the TM^{-1} and the TM^{+1} mode. The lower panels show the profiles along k_x, averaged in k_y over a central region, baseline corrected and fitted with a Gaussian. The black dotted lines indicate the k_x for which the intensity drops by a factor of $1/e^2$ compared to its peak value, which is a measure for the divergence angle.

For estimating the spatial coherence of the laser, the active area can be considered as a rectangular emitting area with side lengths l_x and l_y, corresponding to the coherence lengths in x and y. Such a rectangular, spatially coherent emission area is equivalent to a rectangular aperture illuminated by a plane wave, for which the divergence angles are given by

$$\theta_{i,min} = \pm \frac{\lambda}{2l_i}\,, \qquad i \in \{x, y\}, \tag{6.3}$$

corresponding to the first minima in the diffraction pattern.

With this equation, a coherence length $l_x \approx 93$ um (TM^{-1}) and $l_x \approx 36$ um (TM^{+1}) along x is determined for the patterns in Fig 6.15. In the y-direction, the emission angle exceeds the maximal measured angle of 0.1 rad, which provides an upper bound of the coherence length of $l_y \leq 3$ um.

6.4.7 Quantum Condition

The quantum condition stipulates that at the lasing threshold, the mean photon number in the cavity is equal to one. Assuming this condition is met and using the measured Q-factor of the lasing peak, the corresponding expected output power can be calculated. Comparing this value to the measured output power allows the assessment of whether the quantum condition is indeed met.

The photons in the resonant mode of $Q \approx 3000$ and $\lambda = \frac{c}{\nu} \approx 650$ nm have a lifetime (section 2.10) given by

$$\tau = \frac{Q}{2\pi\nu} \approx 1 \text{ ps} . \tag{6.4}$$

Assuming therefore that in each interval τ a photon of energy

$$E = h\nu \approx 1.9 \text{ eV} = 3 \cdot 10^{-19} \text{ J} \tag{6.5}$$

is emitted, which yields an output power of

$$P_0 = \frac{E}{\tau} \approx 300 \text{ nW} . \tag{6.6}$$

We measure a power of $P_{out} \approx 20$ nW. This measured power must be multiplied by numerous factors f in order to obtain an estimation of the total output power P_{tot}:

- We only collect the light emitted in the positive z-direction $\rightarrow f = 2$

- The objective with NA=0.1 does not collect all emission angles. Assuming a divergence along the y-direction of 0.35 rad as reported for a similar system in [99] $\rightarrow f = 3.5$

- We measure the light reflected from a 50/50 beam splitter $\rightarrow f = 2$

- We measure at a pump power ~ 3 times higher than the threshold pump power $\rightarrow f = 0.33$

  We can therefore estimate a total output power of $P_{tot} \approx 90$ nW at threshold. With this rough estimation, the expected output power of $P_0 \approx 300$ nm is not reached, but we reach the same order of magnitude, which is promising.

6.5 Discussion & Conclusion

The concept of a rectangular nanohole array has been introduced and demonstrated. The shorter period is designed to resonate with the pump laser for excitation enhancement. The larger period is designed to support TM resonances with a high Q-factor for the enhancement of PL emission and providing a distributed feedback cavity for achieving lasing with a WS_2 monolayer. The high Q-factor $Q \approx 3000$ of the cavity is a key feature allowing the low lasing threshold of the order of 1.5 W/cm^2, which is comparable to the lowest thresholds of other 2D-material lasers found in the literature [83, 84, 101].

In combination with a large area monolayer WS_2, we obtain a laser device with high spatial coherence length of several tens of microns and high output power. Thanks to the high measurable power on the order of $P_{out} > 20$ nW, it was possible to carry out the characterisation measurements, in particular of the far field radiation pattern and total emitted power.

For a more detailed analysis of the threshold behaviour, a Hanbury-Brown Twiss experiment to measure the equal-time second order auto-correlation function $g^2(0)$ [102] would allow a more precise determination of pump powers corresponding to amplified spontaneous emission ($g^2(0) > 1$) or coherent laser emission ($g^2(0) \to 1$).

Our promising approach of a large area laser with resonant pumping and a distributed cavity could be adapted for other gain media according to specific applications, e.g. 2D-material with PL emission at wavelengths relevant for communication or sensing applications.

Chapter 7

Thesis Conclusion & Outlook

7.1 Microscopy

7.1.1 iSCAT

In order to perform studies of contrast enhancement in microscopy with GMRs, I built a setup that is capable of both scattering and fluorescence based microscopy. Due to its high sensitivity, iSCAT is a very promising scattering based technique, which I implemented successfully. The smallest particles that could be detected with iSCAT on this setup were 20 nm diameter gold nanoparticles (AuNP). Although this is well below the limit of other scattering microscopy techniques, such as standard dark field microscopy [45], the iSCAT method should allow the detection of much smaller scatterers, such as single proteins down to the order of 10 kDa [49]. In order for the setup to reach this performance, however, it would have needed further improvements, e.g. in terms of mechanical stability, so as to reach a lower noise floor. I explored the enhancement of the iSCAT contrast using partial reflectors [31] via different approaches, such as the partial reflector cube that replaces the beam splitter, or the external partial reflector placed in an intermediate image of the objective back focal plane, but was not able to go beyond the 20 nm particle limit.

Here, I draw a conclusion on the iSCAT part of this work, highlighting mistakes that I made and how I think I should have conducted this part of the project instead - in hindsight. My supervisor accepts partial blame as he had also underestimated the difficulties involved in constructing a successful iSCAT setup. I started this project with the goal of studying GMR enhanced iSCAT. I made a number of mistakes that

prevented me from making useful progress on this idea:

- **The wrong goals: Proteins**

  My approach was to first build a state-of-the-art iSCAT setup, and then study the enhancement. The numerous reports in the literature of the high sensitivity of iSCAT that allows it to see single proteins made me believe that a setup is only a valid iSCAT setup if it is indeed able to detect single proteins - which therefore became my goal. I wanted to see single proteins first and then image the proteins on a resonant grating to explore the enhancement. For protein detection at the limit of the iSCAT technique, the high NA oil immersion objective is paramount. While I put a lot of time and effort into trying to see the proteins with regular iSCAT (see next bullet point), I started fabricating GMR gratings in parallel. The high quality commercial Si_3N_4 films are on 500 um thick substrates, which can therefore not be used with the oil immersion objective, as it has a working distance of only 150 um. I therefore explored ways of fabricating the gratings on thinner substrates, which included growing the Si_3N_4 films myself by sputtering on glass coverslips. These Si_3N_4 films have lower quality and repeatability, which posed additional challenges.

- **Why did I need to see proteins?**

  A good question that I asked myself much too late - because I didn't need to see them. The goal was to study enhancement of the iSCAT with GMRs. Only for imaging particles sufficiently close to the detection limit, a high NA objective is absolutely necessary. However, a lower NA objective that needs no oil immersion and has a longer working distance can also be used for iSCAT. It collects less of the scattered light, thus doesn't reach the performance of the high NA objective, but it is still using the iSCAT principle. Moreover, the low NA objective might be more forgiving concerning noise, as it is generally less sensitive. In light of this consideration, it seems like a more reasonable first goal of the project to use a lower NA objective, fabricate gratings in a high quality commercial Si_3N_4 film, quantify the enhancement with stronger scatterers and take it from there - with decent preliminary results in the bag. With significantly stronger scatterers, e.g. AuNPs of size ≥ 80 nm, the signal might even be strong enough to clearly see them in the raw images without need for ratiometric videos of landing particles in suspension. This would have further simplified the first experiment.

- **Thorough planning of the setup.**

  At the start, keen to build an iSCAT setup and motivated to make fast progress, I found some references containing abstract schematics of an iSCAT setup. The initial literature search I conducted was not sufficiently thorough to discover the references that would have properly illustrated the practical aspects of building the setup. Therefore, I designed the setup based on abstract schematics only. However, I had close to no experience in building an optical setup, and no other member of our group had experience with iSCAT and its specific requirements either. The result was a first setup whose global architecture and some specific parts, such as the sample stage, made little sense in hindsight. What followed was a long optimisation process of this setup, which in the end performed reasonably well compared to other optical imaging techniques, but is far from the state-of-the-art of iSCAT. What I should have done instead is to take the time at the start to plan the setup carefully, including a thorough search of the literature.

- **Looking for support.**

  Additionally, I should have contacted the Kukura Lab in Oxford, one of the leading research groups in the field, right at the start of my project. For example, a visit in their lab would have given me a much better idea of what is needed for a decent setup. Later interactions with this group showed me that they are open to giving their valuable support, which is much appreciated. As I sought the support only in a later stage of this project, a lot of time was already spent, so instead of re-starting from scratch with a better setup design, I tried to work with what I had.

While I was still working on the optimisation of my setup, a publication demonstrating GMR enhanced iSCAT appeared in the literature [5], including everything I planned to do and more. I appreciated the high quality reference and what I learned from it. However, it put the possibility of me contributing to the body of research in the field somewhat out of reach.

Nevertheless, I spent countless thoughts on the technique and how it could be applied or developed. An idea that I find particularly promising is, for example, GMR enhanced mass photometry, which uses the strength of the iSCAT signal to infer mass. It is now known that GMRs can be used to enhance the iSCAT contrast. Nevertheless,

the non-uniformity of the field distribution - and therefore of the enhancement - poses a challenge for mass photometry, since the contrast is used to determine the mass of the landing particles. This non-uniformity could be addressed by calibrating a map of the enhancement as a function of the landing location of a particle within a unit cell. When detecting various particles in a mixed sample during a mass photometry experiment on the resonant grating, each signal could then be normalised by a calibration factor corresponding to its location in the unit cell. This normalised signal should then once more only depend on the particle mass, as known from standard iSCAT, making GMR enhanced mass photometry possible.

7.1.2 Fluorescence

The fluorescence capability of the setup I built was not only interesting for benchmarking the iSCAT images, but also as a standalone imaging technique. The fluorescence imaging posed challenges initially, as the point spread function appeared as a cross-shape that could not be focused properly. The cause of this aberration issue was identified and addressed by using the dichroic mirror at a small incidence angle close to normal, instead of the $45\,°$-angle that it is designed for. With this adjustment, the setup was ready for experiments on fluorescence enhancement with GMRs.

I designed GMR gratings, then fabricated and characterised them. I verified the grating geometry by SEM inspection and characterised the resonances using reflection spectroscopy. The chirped gratings were particularly useful, as they allowed me to spatially encode the spectral information, enabling the measurement of the resonance peak in a single measurement.

With the setup I built, I was able to demonstrate how grating-enhanced microscopy can be achieved, again relying on the chirped GMR design. Only a single experiment, with one field of view and two imaging arms, was sufficient to simultaneously characterise the resonance peak of the grating spectrum and quantify the enhancement of fluorescence excitation, including the measurement of the reference contrast off-resonance.

The enhancement of fluorescence opens new possibilities in two ways: On one hand, the enhancement might make weakly fluorescent particles detectable, which would be below the detection limit without enhancement. On the other hand, for a given fluorescent particle, the enhancement may allow a simpler imaging setup to still detect it successfully. It is therefore of interest to maximise the enhancement. A most promising approach is to combine two resonances for simultaneous excitation and

emission enhancement. This has been demonstrated in [6] with a 1D GMR grating. The two modes used there (TE^{+1} and TE^{-1}) were accessed at the desired wavelengths via different angles. Incidence at an angle might slightly increase the complexity of the setup, but if the angle can be finely tuned, it lifts the need for a lithographic tuning step for the excitation resonance, which is very advantageous from a practical point of view. It would be interesting to explore how this approach can be improved with 2D-gratings, e.g. a square lattice nanohole array, whose higher Q-factor might be important for pushing the enhancement further. As an alternative to the pumping at off-normal incidence, it is possible to design 2D-gratings that support different resonances at normal incidence. In this case, it can be useful to be able to tune the resonances independently, which is what we achieved with the rectangular lattice nanohole array that we used here for the 2D-material laser design.

7.2 2D Material Lasing

As another application of resonantly enhanced light-matter interaction, I demonstrated a WS_2 monolayer laser supporting two resonances for simultaneous excitation and emission enhancement. We used a rectangular lattice nanohole array to provide a GMR mode along one direction to support the pump laser wavelength and along the other direction to support the light emission. Thanks to the high-Q resonant modes supporting the emission, we measured a low lasing threshold of the order of $1.5\ W/cm^2$, which is comparable with the lowest observed thresholds for similar devices in the literature. We obtain comparably high, measurable output power thanks to the large area of the laser which is enabled by the large area deposition of the WS_2 monolayer. In addition, the large lasing area leads to a long coherence length of tens of um along the direction of periodicity for the lasing mode, which is over an order of magnitiude higher than comparable devices reported in the literature.

In order to increase the power output of the laser further, inspiration can be found from reports of 2D-periodic gratings that have been optimised to yield a very high output power $P_{out} \geq 1$ W with III-V gain materials, achieved in Noda's group [103]. They used symmetry-breaking of the hole shape to increase the coupling of the high Q otherwise symmetry-protected BIC mode, whereby the symmetry breaking lifts the symmetry protection and allows it to couple even at the Γ-point, which makes the photon extraction more efficient. By adjusting the extent of the symmetry breaking and the fill factor, the coupling to out-of-plane radiation can be tuned [104]. In our

case with the 2D-material gain medium, it would be interesting look for a symmetry broken unit cell that results in a radiative Q factor that ideally matches the Q-factor describing the losses. This would present a promising trade-off between a high Q for low threshold and a low Q for high extraction efficiency.

For most industrial applications, it would be interesting to achieve lasing by pumping electrically, rather than optically. In such a scenario, the optical pump resonance along the short period of the rectangular lattice would not be required. Instead, a nanohole array with an alternative lattice might further improve the performance, in particular to achieve a low beam divergence in x and y. Furthermore, a different lattice might further lower the threshold, e.g. the honeycomb lattice that led to a lower threshold than a triangular or square lattice for a GaN laser in [105]. This approach could be investigated with 2D-material gain media, again with the possibility to break the hole symmetry in order to optimise the threshold-vs-power trade-off.

Appendix A

S^4 Simulations

A.1 Convergence
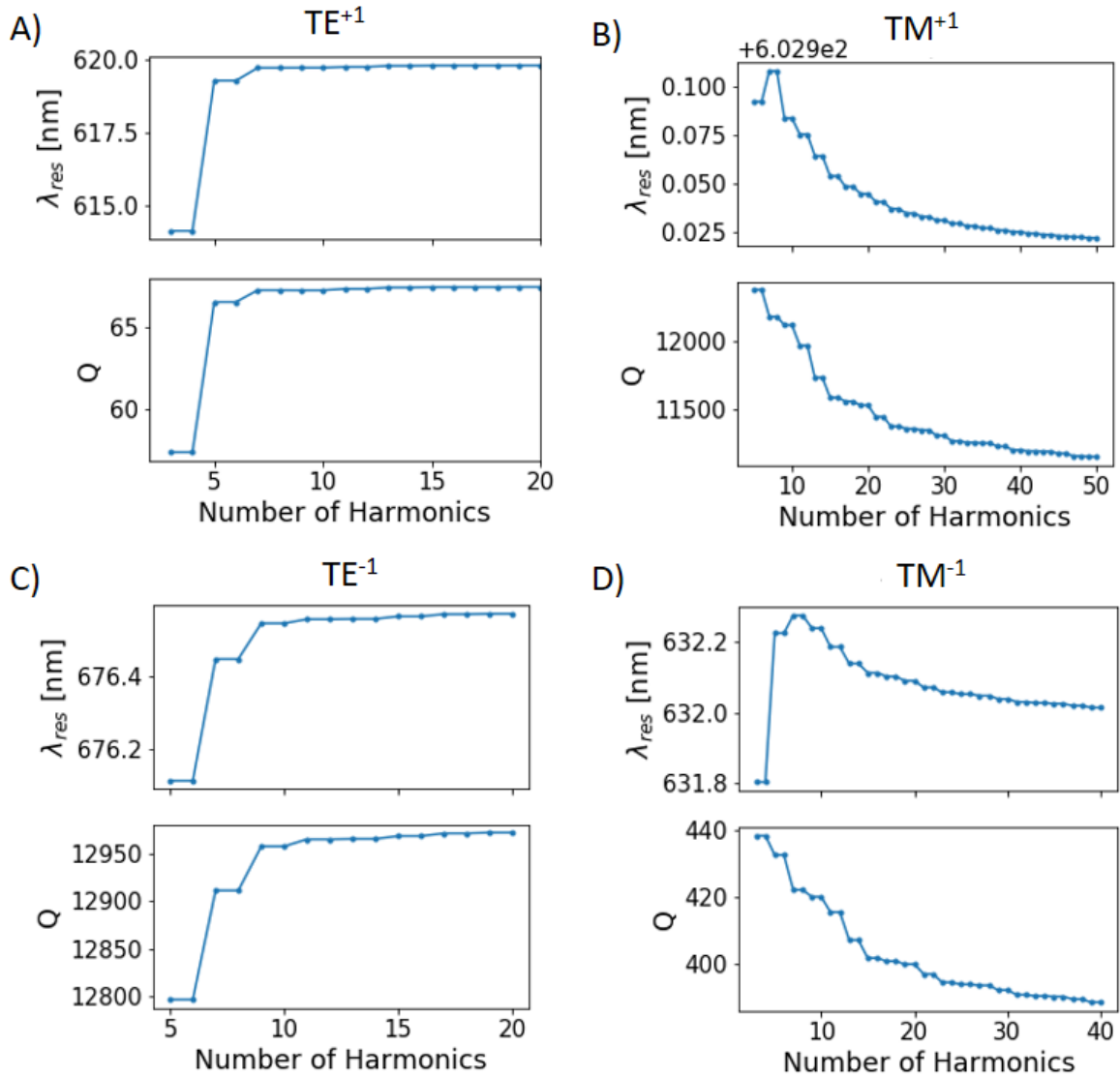
Figure A.1: Convergence of S^4 simulations of GMR modes in a 1D grating. The resonant wavelength and Q-factor are extracted from reflection spectra by fitting a Fano lineshape, then plotted as a function of the number of harmonics. The TE^{+1} (A) and TE^{-1} (C) modes show no significant change for $nHarm > 11$. The TM^{+1} (B) and TM^{-1} (D) converge slower. For this work, all simulations are simulated with 21 harmonics. Grating parameters: Period $a = 400$ nm, $FF = 0.75$, thickness $t = 150$ nm, medium = water.

A.2 TM GMR Modes
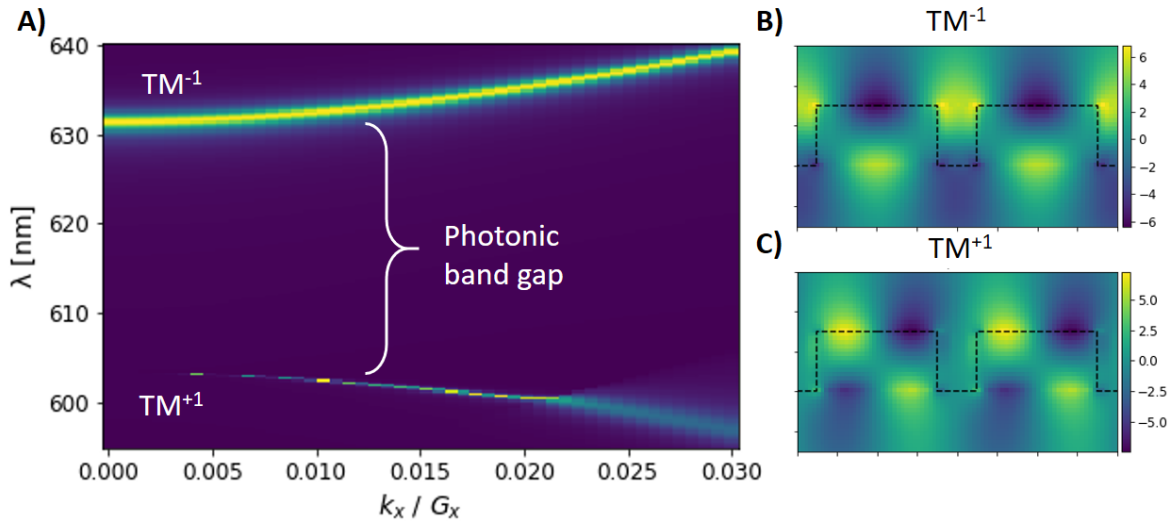
Figure A.2: First band gap around the Γ-point and fields for a GMR-grating with TM-polarised light. A) Band diagram, showing the photonic band gap between two resonances. B) and C) Imaginary x-component of the electric field of the TM^{-1} mode and the TM^{+1} mode (at 0.5º incidence), respectively. Black dashed line: edge of the grating. Grating parameters: Period $a = 400$ nm, grating thickness t=150 nm, fill factor FF=0.75, grating material: Si$_3$N$_4$, substrate: glass, medium: water. Incidence from substrate side.

Appendix B

Spacing Between Reflected Beams from Glass Slide

In section 4.3.1, interference fringes are observed with a partial reflector on a microscope slide, when using it in the position of the beam splitter in the iSCAT setup. To confirm that the fringes are due to interference between a first beam reflected on the partial reflector and a second beam reflected from the glass-air interface at the back of the microscope slide, the lateral spacing $\tilde{d}$ between the two beams is required. This is calculated here.

Consider a beam of light, here represented by one ray, impinging on a glass slide with an incidence angle of $\theta_{air} = 45\,°$, as illustrated in Fig B.1. The first beam is reflected by the first interface. The second beam is transmitted by this interface. Using Snell's law, one can find the transmission angle

$$\theta_g = \arcsin\left(\frac{n_{air}}{n_g}\sin(\theta_{air})\right) = 28.1\,°, \tag{B.1}$$

using the refractive index of air $n_{air} = 1$ glass $n_g = 1.5$. The beam inside the glass slide is then reflected by the bottom glass-air interface, after which it is again transmitted at the top interface. The distance w along the top glass surface, between the entry the exit point of the second beam, is given by

$$w = 2d\tan(\theta_g) = 1.07 \text{ mm}, \tag{B.2}$$

with the glass thickness $d = 1$ mm. Finally, the lateral separation between the two reflected beams is given by

$$\tilde{d} = w \sin(90\,^\circ - \theta_{air}) = w \cos(\theta_{air}) = 0.76 \text{ mm}. \tag{B.3}$$
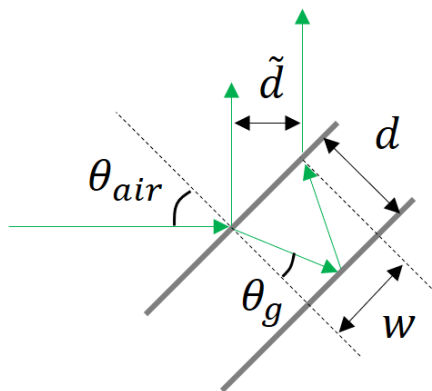
Figure B.1: Schematic used for the calculation of the spacing between two beams reflected on the top / bottom surface of a glass slide of thickness d.

Bibliography

[1]   Giorgio Quaranta et al. "Recent Advances in Resonant Waveguide Gratings". In: *Laser & Photonics Reviews* 12.1800017 (2018). DOI: 10.1002/LPOR.201800017.

[2]   Helen Miller et al. "Single-molecule techniques in biophysics: a review of the progress in methods and applications". In: *Reports on Progress in Physics* 81.024601 (2017). DOI: 10.1088/1361-6633/AA8A02.

[3]   Kirti Prakash et al. "Super-resolution microscopy: a brief history and new avenues". In: *Philosophical Transactions of the Royal Society A* 380.20210110 (2022). DOI: 10.1098/RSTA.2021.0110.

[4]   A. P. Demchenko. "Photobleaching of organic fluorophores: quantitative characterization, mechanisms, protection". In: *Methods Appl. Fluoresc.* 8 (2020). DOI: 10.1088/2050-6120/ab7365.

[5]   Nantao Li et al. "Photonic resonator interferometric scattering microscopy". In: *Nature Communications* 12.1744 (2021). DOI: 10.1038/s41467-021-21999-3.

[6]   Yanyu Xiong et al. "Photonic crystal enhanced fluorescence emission and blinking suppression for single quantum dot digital resolution biosensing". In: *Nature Communications* 13.4647 (2022). DOI: 10.1038/s41467-022-32387-w.

[7]   T. H. Maiman. "Stimulated Optical Radiation in Ruby". In: *Nature* 187 (1960), pp. 493–494. DOI: 10.1038/187493a0.

[8]   Wen Du et al. "Nanolasers Based on 2D Materials". In: *Laser & Photonics Reviews* 14.2000271 (2020). DOI: 10.1002/lpor.202000271.

[9]   E. Hecht. *Optics.* 4th ed. San Francisco: Addison Wesley, 2002.

[10] B. E. A. Saleh and M. C. Teich. *Fundamentals of Photonics.* 3rd ed. New York: Wiley, 2019. DOI: 10.1002/0471213748.

[11]   Giampaolo Pitruzzello and Thomas F. Krauss. "Photonic crystal resonances for sensing and imaging". In: *Journal of Optics* 20.7 (2018). DOI: 10.1088/2040-8986/AAC75B.

[12]   Felix Bloch. "Über die Quantenmechanik der Elektronen in Kristallgittern". In: *Zeitschrift für Physik* 52 (1929), pp. 555–600. DOI: https://doi.org/10.1007/BF01339455.

[13]   Victor Liu and Shanhui Fan. "S^4 : A free electromagnetic solver for layered periodic structures". In: *Computer Physics Communications* 183.10 (2012), pp. 2233–2244. DOI: 10.1016/j.cpc.2012.04.026.

[14]   M. G. Moharam and T. K. Gaylord. "Rigorous coupled-wave analysis of planar-grating diffraction". In: *J. Opt. Soc. Am.* 71.7 (1981), pp. 811–818. DOI: 10.1364/JOSA.71.000811.

[15]   Mikhail N. Polyanskiy. *Refractive index database*. URL: https://refractiveindex.info (visited on 10/08/2022).

[16]   Chia Wei Hsu et al. "Bound states in the continuum". In: *Nature Reviews Materials* 1.16048 (2016). DOI: 10.1038/natrevmats.2016.48.

[17]   Mikhail F. Limonov et al. "Fano resonances in photonics". In: *Nature Photonics* 11.9 (2017), pp. 543–554. DOI: 10.1038/nphoton.2017.142.

[18]   E. I. Green. "The Story of Q". In: *American Scientist* 43 (1955), pp. 584–594.

[19]   J. M. Zhang and Y. Liu. "Fermi's golden rule: its derivation and breakdown by an ideal model". In: *European Journal of Physics* 37 (2016), p. 065406. DOI: 10.1088/0143-0807/37/6/065406.

[20]   E. M. Purcell, H. C. Torrey, and R. V. Pound. "Resonance absorption by nuclear magnetic moments in a solid". In: *Physical Review* 69 (1946), pp. 37–38. DOI: https://doi.org/10.1103/PhysRev.69.37.

[21]   M Ghebrebrhan et al. "Tailoring thermal emission via Q matching of photonic crystal resonances". In: *PHYSICAL REVIEW A* 83.033810 (2011). DOI: 10.1103/PhysRevA.83.033810.

[22]   Donato Conteduca et al. "Beyond Q: The Importance of the Resonance Amplitude for Photonic Sensors". In: *ACS Photonics* 9 (2022), pp. 1757–1763. DOI: https://doi.org/10.1021/acsphotonics.2c00188.

[23] Kevin Luke et al. "Broadband mid-infrared frequency comb generation in a Si_3N_4 microresonator". In: *Optics Letters* 40.21 (2015). DOI: 10.1364/OL.40.004823.

[24] Zoran Krstic and Vladimir D Krstic. "Silicon nitride: the engineering material of the future". In: *Journal of Materials Science* 47 (2012), pp. 535–552. DOI: 10.1007/s10853-011-5942-5.

[25] Graham J. Triggs et al. "Chirped guided-mode resonance biosensor". In: *Optica* 4.2 (2017), pp. 229–234. DOI: 10.1364/OPTICA.4.000229.

[26] K Lindfors et al. "Detection and Spectroscopy of Gold Nanoparticles Using Supercontinuum White Light Confocal Microscopy". In: *Physical Review Letters* 93.3 (2004). DOI: 10.1103/PhysRevLett.93.037401.

[27] Lee Priest, Jack S. Peters, and Philipp Kukura. "Scattering based Light Microscopy: From Metal Nanoparticles to Single Proteins". In: *Chemical Reviews* 121.19 (2021). DOI: 10.1021/acs.chemrev.1c00271.

[28] Richard W Taylor and Vahid Sandoghdar. "Interferometric Scattering Microscopy: Seeing Single Nanoparticles and Molecules via Rayleigh Scattering". In: *Nano Letters* 19 (2019), 4827-4835. DOI: 10.1021/acs.nanolett.9b01822.

[29] Jaime Ortega Arroyo, Daniel Cole, and Philipp Kukura. "Interferometric scattering microscopy and its combination with single-molecule fluorescence imaging". In: *Nature Protocols* 11.4 (2016), pp. 617–633. DOI: 10.1038/nprot.2016.022.

[30] Reza Gholami Mahmoodabadi et al. "Point spread function in interferometric scattering microscopy (iSCAT). Part I: aberrations in defocusing and axial localization". In: *Optics Express* 28.18 (2020), pp. 25969–25988. DOI: 10.1364/OE.401374.

[31] Daniel Cole et al. "Label-Free Single-Molecule Imaging with Numerical-Aperture-Shaped Interferometric Scattering Microscopy". In: *ACS Photonics* 4.2 (2017), pp. 211–216. DOI: 10.1021/acsphotonics.6b00912.

[32] Ying-Hsiu Lin, Wei-Lin Chang, and Chia-Lung Hsieh. "Shot-noise limited localization of single 20 nm gold particles with nanometer spatial precision within microseconds". In: *Optics Express* 22.8 (2014), pp. 9159–9170. DOI: 10.1364/OE.22.009159.

[33] Alan J Walton. "The Abbe theory of imaging: an alternative derivation of the resolution limit". In: *European Journal of Physics* 7.62 (1986).

[34]   H.P. Herzig. *Micro-Optics: Elements, Systems And Applications.* 1st ed. CRC Press, 1997. DOI: https://doi.org/10.1201/9781482272802.

[35]   Matz Liebel, James T Hugall, and Niek F van Hulst. "Ultrasensitive Label-Free Nanosensing and High-Speed Tracking of Single Proteins". In: *Nano Letters* 17 (2017), 1277-1281. DOI: 10.1021/acs.nanolett.6b05040.

[36]   Oguzhan Avci et al. "Pupil function engineering for enhanced nanoparticle visibility in wide-field interferometric microscopy". In: *Optica* 4.2 (2017), pp. 247–254. DOI: 10.1364/OPTICA.4.000247.

[37]   M. Andreas Lieb, James M. Zavislan, and Lukas Novotny. "Single-molecule orientations determined by direct emission pattern imaging". In: *J. Opt. Soc. Am. B* 21.6 (2004), pp. 1210–1215. DOI: 10.1364/JOSAB.21.001210.

[38]   Derin Sevenler et al. "Digital Microarrays: Single-Molecule Readout with Interferometric Detection of Plasmonic Nanorod Labels". In: *ACS Nano* 12 (2018), 5880-5887. DOI: 10.1021/acsnano.8b02036.

[39]   Yuting Yang et al. "Interferometric plasmonic imaging and detection of single exosomes". In: *Proceedings of the National Academy of Sciences of the United States of America* 115.41 (2018), pp. 10275–10280. DOI: https://doi.org/10.1073/pnas.1804548115.

[40]   Pengfei Zhang et al. "Plasmonic scattering imaging of single proteins and binding kinetics". In: *Nature Methods* 17 (2020), pp. 1010–1017. DOI: 10.1038/s41592-020-0947-0.

[41]   Atsushi Miyawaki and Yusuke Niino. "Molecular Spies for Bioimaging-Fluorescent Protein-Based Probes". In: *Molecular Cell* 58 (2015), pp. 632–643. DOI: 10.1016/J.MOLCEL.2015.03.002.

[42]   Jaime Ortega-Arroyo and Philipp Kukura. "Interferometric scattering microscopy (iSCAT): new frontiers in ultrafast and ultrasensitive optical microscopy". In: *Physical Chemistry Chemical Physics* 14.45 (2012), p. 15625. DOI: 10.1039/c2cp41013c.

[43]   Michael J Saxton and Ken Jacobson. "SINGLE-PARTICLE TRACKING: Applications to Membrane Dynamics". In: *Annu. Rev. Biophys. Biomol. Struct* 26 (1997), pp. 373–99. DOI: 10.1146/annurev.biophys.26.1.373.

[44] P. Philippe Laissue et al. "Assessing phototoxicity in live fluorescence imaging". In: *Nature Methods* 14.7 (2017), pp. 657–661. DOI: 10.1038/nmeth.4344.

[45] Alexander Weigel, Aleksandar Sebesta, and Philipp Kukura. "Dark Field Microspectroscopy with Single Molecule Fluorescence Sensitivity". In: *ACS Photonics* 1.9 (2014), pp. 848–856. DOI: https://doi.org/10.1021/ph500138u.

[46] Kristýna Holanová, Milan Vala, and Marek Piliarik. "Optical imaging and localization of prospective scattering labels smaller than a single protein". In: *Optics and Laser Technology* 109 (2019), pp. 323–327. DOI: 10.1016/J.OPTLASTEC. 2018.08.014.

[47] J Ortega Arroyo et al. "Label-Free, All-Optical Detection, Imaging, and Tracking of a Single Protein". In: *Nano Lett* 14 (2014), 2065-2070. DOI: 10.1021/nl500234t.

[48] Richard W Taylor et al. "Interferometric scattering microscopy reveals microsecond nanoscopic protein motion on a live cell membrane". In: *Nature Photonics* 13 (2019), pp. 480–487. DOI: 10.1038/s41566-019-0414-6.

[49] Mahyar Dahmardeh et al. "Self-supervised machine learning pushes the sensitivity limit in label-free detection of single proteins below 10 kDa". In: *Nature Methods* 20.3 (2023), pp. 442–447. DOI: 10.1038/s41592-023-01778-2.

[50] Gavin Young et al. "Quantitative mass imaging of single biological macromolecules". In: *Science* 360 (2018), pp. 423–427. DOI: DOI:10.1126/science. aar5839.

[51] Matthias Mann, Ronald C Hendrickson, and Akhilesh Pandey. "ANALYSIS OF PROTEINS AND PROTEOMES BY MASS SPECTROMETRY". In: *Annu. Rev. Biochem.* 70 (2001), pp. 437–473. DOI: https://doi.org/10.1146/annurev. biochem.70.1.437.

[52] Anna Olerinyova et al. "Mass Photometry of Membrane Proteins". In: *Chem* 7 (2021), pp. 224–236. DOI: 10.1016/j.chempr.2020.11.011.

[53] Katharina Häußermann et al. "Dissecting FOXP2 Oligomerization and DNA Binding". In: *Angew.Chem.Int. Ed.* 58 (2019), pp. 7662–7667. DOI: 10.1002/ange. 201901734.

[54] Di Wu and Grzegorz Piszczek. "Measuring the affinity of protein-protein interactions on a single-molecule level by mass photometry". In: *Analytical Biochemistry* 592.113575 (2020). DOI: 10.1016/j.ab.2020.113575.

[55]   Ali D. Malay et al. "An ultra-stable gold-coordinated protein cage displaying reversible assembly". In: *Nature* 569 (2019), pp. 438–442. DOI: 10.1038/s41586-019-1185-4.

[56]   Alex Naftaly et al. "Revealing Advanced Glycation End Products Associated Structural Changes in Serum Albumin". In: *ACS Biomater. Sci. Eng* 7 (2021), pp. 3179–3189. DOI: 10.1021/acsbiomaterials.1c00387.

[57]   Thiago V. Seraphim et al. "Assembly principles of the human R2TP chaperone complex reveal the presence of R2T and R2P complexes". In: *Structure* 30 (2022), pp. 156–171. DOI: 10.1016/J.STR.2021.08.002.

[58]   C. Shannon. "Communication in the Presence of Noise". In: *Proceedings of the IRE* 37.1 (1949). DOI: 10.1109/JRPROC.1949.232969.

[59]   Peter D Welch. "The Use of Fast Fourier Transform for the Estimation of Power Spectra: A Method Based on Time Averaging Over Short, Modified Periodograms". In: *IEEE Transactions on Audio and Electroacoustics* 15.2 (1967). DOI: 10.1109/TAU.1967.1161901.

[60]   Pauli Virtanen et al. "SciPy 1.0: fundamental algorithms for scientific computing in Python". In: *Nature Methods* 17 (2020), pp. 261–272. DOI: 10.1038/s41592-019-0686-2.

[61]   André Gemeinhardt et al. "Label-Free Imaging of Single Proteins Secreted from Living Cells via iSCAT Microscopy". In: *JoVE (Journal of Visualized Experiments)* 141.e58486 (2018). DOI: 10.3791/58486.

[62]   S. H. Behrens and D. G. Grier. "The charge of glass and silica surfaces". In: *Journal of Chemical Physics* 115.14 (2001), pp. 6716–6721. DOI: 10.1063/1.1404988.

[63]   William Sutherland. "LXXV. A dynamical theory of diffusion for non-electrolytes and the molecular mass of albumin". In: *The London, Edinburgh, and Dublin Philosophical Magazine and Journal of Science* 9.54 (1905), pp. 781–785. DOI: 10.1080/14786440509463331.

[64]   Houman Mirzaalian Dastjerdi et al. "Optimized analysis for sensitive detection and analysis of single proteins via interferometric scattering microscopy". In: *Journal of Physics D: Applied Physics* 55.054002 (2022). DOI: 10.1088/1361-6463/ac2f68.

[65] Johannes Schindelin et al. "Fiji: An open-source platform for biological-image analysis". In: *Nature Methods* 9.7 (2012), pp. 676–682. DOI: 10.1038/NMETH. 2019.

[66] Andreas E. Vasdekis and Gregoire P.J. Laporte. "Enhancing Single Molecule Imaging in Optofluidics and Microfluidics". In: *International Journal of Molecular Sciences* 12.8 (2011), pp. 5135–5156. DOI: 10.3390/IJMS12085135.

[67] Yanyu Xiong et al. "Photonic Crystal Enhanced Fluorescence: A Review on Design Strategies and Applications". In: *Micromachines* 14.3 (2023), p. 668. DOI: 10.3390/MI14030668.

[68] Taishi Zhang et al. "Single-Particle Spectroscopic Study on Fluorescence Enhancement by Plasmon Coupled Gold Nanorod Dimers Assembled on DNA Origami". In: *J. Phys. Chem. Lett* 6 (2015). DOI: 10.1021/acs.jpclett.5b00747.

[69] Gleb M. Akselrod et al. "Probing the mechanisms of large Purcell enhancement in plasmonic nanoantennas". In: *Nature Photonics* 8 (2014), pp. 835–840. DOI: 10.1038/nphoton.2014.228.

[70] Pavel Kolchin et al. "High Purcell Factor Due To Coupling of a Single Emitter to a Dielectric Slot Waveguide". In: *Nano Lett* 15 (2015), 464-468. DOI: 10.1021/nl5037808.

[71] Nikhil Ganesh et al. "Leaky-mode assisted fluorescence extraction: application to fluorescence enhancement biosensors". In: *Optics Express* 16.26 (2008), pp. 21626–21640. DOI: 10.1364/OE.16.021626.

[72] Jean-Yves Tinevez et al. "TrackMate: An open and extensible platform for single-particle tracking". In: *Methods* 115 (2017). Image Processing for Biologists, pp. 80–90. DOI: https://doi.org/10.1016/j.ymeth.2016.09.016.

[73] M F Paige, E J Bjerneld, and W E Moerner. "A Comparison of Through-the-Objective Total Internal Reflection Microscopy and Epi-fluorescence Microscopy for Single-Molecule Fluorescence Imaging". In: *Single Molecules* 2 (2001), pp. 191–201. DOI: 10.1002/1438-5171(200110)2:3<191::AID-SIMO191>3.0.CO;2-K.

[74] Thomas Mueller and Ermin Malic. "Exciton physics and device application of two-dimensional transition metal dichalcogenide semiconductors". In: *npj 2D Materials and Applications* 2.29 (2018), pp. 1–12. DOI: 10.1038/s41699-018-0074-2.

[75]   Dinh Van Tuan, Min Yang, and Hanan Dery. "Coulomb interaction in monolayer transition-metal dichalcogenides". In: *Physical Review B* 98.125308 (2018). DOI: 10.1103/PhysRevB.98.125308.

[76]   M J L S Haines et al. "Exciton-binding-energy maximum in $Ga_{1-x}In_xAs/GaAs$ quantum wells". In: *Phys. Rev. B* 43.14 (1991), pp. 11944–11949. DOI: 10.1103/PhysRevB.43.11944.

[77]   D Orani et al. "Binding Energy and Lifetime of Excitons in $In_xGa_{1-x}As/GaAs$ Quantum Wells". In: *physica status solidi (a)* 164 (1997), pp. 107–110. DOI: https://doi.org/10.1002/1521-396X(199711)164:1<107::AID-PSSA107>3.0.CO;2-8.

[78]   Qing Hua Wang et al. "Electronics and optoelectronics of two-dimensional transition metal dichalcogenides". In: *Nature Nanotechnology* 7 (2012), pp. 699–712. DOI: 10.1038/NNANO.2012.193.

[79]   Maurizia Palummo, Marco Bernardi, and Jeffrey C. Grossman. "Exciton radiative lifetimes in two-dimensional transition metal dichalcogenides". In: *Nano Letters* 15 (2015), pp. 2794–2800. DOI: https://doi.org/10.1021/nl503799t.

[80]   F. Lohof et al. "Prospects and Limitations of Transition Metal Dichalcogenide Laser Gain Materials". In: *Nano Letters* 19 (2019), 210-217. DOI: 10.1021/ACS.NANOLETT.8B03729.

[81]   Yu Ye et al. "Monolayer excitonic laser". In: *Nature Photonics* 9 (2015). DOI: 10.1038/NPHOTON.2015.197.

[82]   Omid Salehzadeh et al. "Optically Pumped Two-Dimensional MoS_2 Lasers Operating at Room-Temperature". In: *Nano Letters* 15 (2015), 5302-5306. DOI: 10.1021/acs.nanolett.5b01665.

[83]   Sanfeng Wu et al. "Monolayer semiconductor nanocavity lasers with ultralow thresholds". In: *Nature* 520.71 (2015). DOI: 10.1038/nature14290.

[84]   Jingzhi Shang et al. "Room-temperature 2D semiconductor activated vertical-cavity surface-emitting lasers". In: *Nature Communications* 8.543 (2017). DOI: 10.1038/s41467-017-00743-w.

[85]   Wuzhou Song et al. "Low-order distributed feedback optofluidic dye laser with reduced threshold". In: *Applied Physics Letters* 94.5 (2009), p. 051117. DOI: 10.1063/1.3079799.

[86] Ashok Kodigala et al. "Lasing action from photonic bound states in continuum". In: *Nature* 541 (2017). DOI: 10.1038/nature20799.

[87] Min Soo Hwang et al. "Ultralow-threshold laser using super-bound states in the continuum". In: *Nature Communications* 12.4135 (2021). DOI: 10.1038/s41467-021-24502-0.

[88] Shaimaa I. Azzam and Alexander V. Kildishev. "Photonic Bound States in the Continuum: From Basics to Applications". In: *Advanced Optical Materials* 9.2001469 (2021). DOI: 10.1002/ADOM.202001469.

[89] Xiaochen Ge et al. "Laterally confined photonic crystal surface emitting laser incorporating monolayer tungsten disulfide". In: *npj 2D Materials and Applications* 3.16 (2019). DOI: 10.1038/s41699-019-0099-1.

[90] Dominik Andrzejewski et al. "Scalable Large-Area p-i-n Light-Emitting Diodes Based on WS_2 Monolayers Grown via MOCVD". In: *ACS Photonics* 6 (2019), 1832-1839. DOI: 10.1021/acsphotonics.9b00311.

[91] F. Raineri et al. "Doubly resonant photonic crystal for efficient laser operation: Pumping and lasing at low group velocity photonic modes". In: *Applied Physics Letters* 86.011116 (2005). DOI: 10.1063/1.1846148.

[92] Chun Ge et al. "Enhancement of pump efficiency of a visible wavelength organic distributed feedback laser by resonant optical pumping". In: *Optics Express* 19.6 (2011), pp. 5086–5092. DOI: 10.1364/OE.19.005086.

[93] Lewis Reeves, Yue Wang, and Thomas F. Krauss. "2D Material Microcavity Light Emitters: To Lase or Not to Lase?" In: *Advanced Optical Materials* 6.1800272 (2018). DOI: 10.1002/ADOM.201800272.

[94] Gunnar Björk, Anders Karlsson, and Yoshihisa Yamamoto. "Definition of a laser threshold". In: *PHYSICAL REVIEW A* 50.2 (1994). DOI: https://doi.org/10.1103/PhysRevA.50.1675.

[95] Anthony E Siegman. *Lasers*. University science books, 1986.

[96] *Refractive index of SCHOTT - BOROFLOAT® 33*. https://refractiveindex.info/?shelf=glass&book=SCHOTT-multipurpose&page=BOROFLOAT33. Accessed: 2023-01-27.

141

[97]   N. Sultanova, S. Kasarova, and I. Nikolov. "Dispersion Properties of Optical Polymers". In: *Acta Physica Polonica A* 116.4 (Oct. 2009), p. 585. DOI: 10.12693/APhysPolA.116.585.

[98]   Gangyi Xu et al. "Efficient power extraction in surface-emitting semiconductor lasers using graded photonic heterostructures". In: *Nature Communications* 3.952 (2012). DOI: 10.1038/ncomms1958.

[99]   George Heliotis et al. "Emission characteristics and performance comparison of polyfluorene lasers with one- and two-dimensional distributed feedback". In: *Advanced Functional Materials* 14.1 (2004), pp. 91–97. DOI: 10.1002/ADFM.200305504.

[100]   Eiji Miyai et al. "Lasers producing tailored beams". In: *Nature* 441 (2006), p. 946. DOI: 10.1038/441946a.

[101]   Yongzhuo Li et al. "Room-temperature continuous-wave lasing from monolayer molybdenum ditelluride integrated with a silicon nanobeam cavity". In: *Nature Nanotechnology* 12 (2017), pp. 987–992. DOI: 10.1038/nnano.2017.128.

[102]   R. Hanbury Brown and R.Q. Twiss. "LXXIV. A new type of interferometer for use in radio astronomy". In: *The London, Edinburgh, and Dublin Philosophical Magazine and Journal of Science* 45.366 (1954), pp. 663–682. DOI: 10.1080/14786440708520475.

[103]   Kazuyoshi Hirose et al. "Watt-class high-power, high-beam-quality photonic-crystal lasers". In: *Nature Photonics* 8.5 (2014), pp. 406–411. DOI: 10.1038/NPHOTON.2014.75.

[104]   Yong Liang et al. "Three-dimensional coupled-wave model for square-lattice photonic crystal lasers with transverse electric polarization: A general approach". In: *PHYSICAL REVIEW B* 84.195119 (2011). DOI: 10.1103/PhysRevB.84.195119.

[105]   Tzeng Tsong Wu, Chih Cheng Chen, and Tien Chang Lu. "Effects of Lattice Types on GaN-Based Photonic Crystal Surface-Emitting Lasers". In: *IEEE Journal of Selected Topics in Quantum Electronics* 21.1 (2015). DOI: 10.1109/JSTQE.2014.2358086.

List of Figures

List of Tables